TOWARD THE VIRGO CLUSTER: ON THE STUDY OF NEUTRAL HYDROGEN IN THE LOCAL UNIVERSE

A Dissertation

Presented to the Faculty of the Graduate School

of Cornell University

in Partial Fulfillment of the Requirements for the Degree of

Doctor of Philosophy

by

Brian Robert Kent

August 2008

TOWARD THE VIRGO CLUSTER:

ON THE STUDY OF NEUTRAL HYDROGEN IN THE LOCAL UNIVERSE

Brian Robert Kent, Ph.D.

Cornell University 2008

A catalog of neutral hydrogen detections toward the Virgo cluster has been assembled. The data set uses observations from the Arecibo Legacy Fast ALFA (ALFALFA) survey, a large extragalactic survey project using the new multi-beam receiver at the Arecibo Observatory. The survey is an ongoing effort and will eventually cover 7000 square degrees of high galactic latitude sky. The technical background, observing mode, and data reduction procedures will be described. The catalog of HI detections and their associated distributions and statistics will be discussed. A number of unique HI detections from the catalog appear to have interesting properties. Some appear associated with, but offset from, low surface brightness optical counterparts; others, at larger spatial offsets, may be tidally related to optical counterparts. Yet another class includes detections which are not identifiable with any optical emission available in online imaging databases. The preliminary ALFALFA results on these objects in the Virgo region, as well as followup aperture synthesis observations obtained with the Very Large Array, will be described. These gas-rich, optically dim objects are not detected in large numbers and are likely not primordial in nature. We explore scenarios pertaining to their origin from ram pressure stripping of large disk galaxies in a cluster environment. We also briefly discuss an HI mass function for the Virgo HI detections, as well as preliminary simulations of a disk galaxy moving at high speed through a cluster environment. The summary of results will include future endeavors with high-velocity clouds and mapping of galactic neutral hydrogen.

BIOGRAPHICAL SKETCH

Brian Robert Kent was born on October 6, 1980, in Morgantown, West Virginia. He attended Morgan Heights School, North Elementary, and Suncrest Junior High School. His childhood interests included outer space and computers, as well as playing the piano and trombone. He graduated from Morgantown High School in 1999, and attended West Virginia University with a Foundation Scholarship. As a physics major, he was awarded the Eberly College of Arts and Science Scholarship, as well as a Barry Goldwater Scholarship. He was a summer student with the Southeastern Association for Research in Astronomy at Florida International University in 2001, and a summer student at the National Radio Astronomy Observatory at Green Bank in 2002. He graduated with a Bachelor of Science degree in Physics, summa cum laude and Phi Beta Kappa in 2003. He was accepted to Cornell University, and undertook research in extragalactic astrophysics and radio astronomy, earning a Master of Science degree in 2006. He has used the Arecibo Radio Telescope, Green Bank Telescope, Very Large Array, and Hale 5-meter Telescope at the Palomar Observatory for his astronomy research. Brian earned his Doctor of Philosophy degree from Cornell University in 2008. His interests include Star Wars, science-fiction, photography, cooking, and astronomy.

He will continue his research in radio astronomy and astrophysics as a Jansky Fellow at the National Radio Astronomy Observatory in Charlottesville, Virginia.

This dissertation is dedicated to my Mom, Linda.

For most of human history we have searched for our place in the cosmos. Who are we? What are we? We find that we inhabit an insignificant planet of a hum-drum star lost in a galaxy tucked away in some forgotten corner of a universe in which there are far more galaxies than people. This perspective is a courageous continuation of our penchant for constructing and testing mental models of the skies; the Sun as a red-hot stone, the stars as a celestial flame, the Galaxy as the backbone of night.

- Dr. Carl Sagan in *Cosmos*

ACKNOWLEDGEMENTS

This work has been supported by NSF grants AST–0307661, AST–0435697, AST–0347929, AST–0407011, AST–0302049 awarded to Professors Riccardo Giovanelli and Martha P. Haynes. The National Astronomy and Ionosphere Center is operated by Cornell University under a cooperative agreement with the National Science Foundation. Support for observing and and participation in summer schools has been provided by NAIC and Professor Robert Brown. The mentioned individuals as well as Professors Richard Lovelace and Eanna Flanagan have served on the committee for this dissertation. The National Radio Astronomy Observatory is a facility of the National Science Foundation operated under cooperative agreement by Associated Universities, Inc. This research has made use of data obtained from or software provided by the US National Virtual Observatory(NVO), which is sponsored by the National Science Foundation. Support has been provided by the NVO through Drs. Robert Hanisch, Tom McGlynn, Alex Szalay, and Roy Williams. Financial support for conference travel has been provided on numerous occasions by the Cornell University Graduate School. Dr. German Cortes and Mr. Phil Perillat have provided theoretical and observational data used to create the beam maps for this dissertation. Several plots in this work make use of color tables from the work of Dr. Aaron Baarth. Mr. Tom Shannon has provided invaluable computer and operating system support. Dr. Adam Brazier has provided important discussions and software support for the survey databases. Professor David Kornreich has provided information and discussions concerning N-body and SPH simulations. The creators and curators of the SAO/NASA Astrophysics Data System (ADS) have made referencing much more efficient in an age of countless articles in the scientific literature. Drs. Christopher Springob and Karen Masters dissertation work is utilized for distance and HI mass function determinations. Dr. Kristine Spekkens provided VLA measurements for HI cloud detections. This research has made use of the NASA/IPAC Extra-

galactic Database (NED) which is operated by the Jet Propulsion Laboratory, California Institute of Technology, under contract with the National Aeronautics and Space Administration. *Skyview* was developed and maintained under NASA ADP Grant NAS5-32068 under the auspices of the High Energy Astrophysics Science Archive Research Center at the Goddard Space Flight Center Laboratory of NASA. This research made use of Montage, funded by the National Aeronautics and Space Administration's Earth Science Technology Office, Computation Technologies Project, under Cooperative Agreement Number NCC5-626 between NASA and the California Institute of Technology. Montage is maintained by the NASA/IPAC Infrared Science Archive.

The financial, technical, and operational support afforded by these individuals and organizations has allowed participation in many meetings, schools, conferences, and activities to the benefit of my education.

A number of individuals and family members have supported me before and during graduate school. Dr. Jim Webb provided my first astronomical research experience at Florida International University studying quasar variability. Dr. Jim Braatz afforded me the opportunity to work with him at NRAO Green Bank. Dr. Jack Littleton supported me in both the classroom and in my research initiatives while an undergraduate physics major. My dad, Bob, has given me his support during my years in school, for which I am very appreciative. Dr. Jorge Cham's *Ph.D. Comics* have provided an extremely helpful dose of humor during graduate school.

I would like to thank "the three Uncles" for their encouragement and support. They are great and extremely intelligent guys who are wonderful friends and share many of my interests. My uncle Tom Conforti is the best and most patient teacher in the world. I wouldn't have made it through the beginnings of my math training without his help. My uncle Dan Conforti has always supported my endeavors with great interest, and I continue to enjoy discussing a wide range of scientific and economic topics with him. I

admire my uncle Richard Conforti as he is one of the most easy going, friendly, and kind people I know. It is so great discussing everything with him, from *Cosmos* to telescopes, and computers to our favorite books. I look forward to many conversations in the future.

I would like to thank my sister, Marcie, an enormously talented and great person. I am privileged to be her brother.

I can never even begin to thank my mom Linda enough for all she does for me. She is the nicest, most intelligent, and most genuine person in the world. Her never ending encouragement and pride for what I do has helped me through all the ups and downs of both life and graduate school. She is a wonderful person, friend, and mom, and I am very proud to be her son. We would *both* like to thank David Letterman for giving us the snow globe on July 25, 2007.

TABLE OF CONTENTS

Biographical Sketch . . . iii
Dedication . . . iv
Acknowledgements . . . v
Table of Contents . . . viii
List of Tables . . . x
List of Figures . . . xi

1 Introduction 1
1.1 Surveying Galaxies in the Universe . . . 1
1.2 Neutral Hydrogen . . . 5
1.3 Early Virgo Cluster Observations and Optical Surveys . . . 6
1.4 Neutral Hydrogen, Virgo, and Surveys . . . 9
1.5 Overview of the Dissertation . . . 14

2 The Arecibo Legacy Fast ALFA Survey 16
2.1 The Arecibo *L*-band Feed Array . . . 16
2.2 Survey Sensitivity and Detection Thresholds . . . 19
2.3 Observations . . . 24
2.4 Data Reduction . . . 26
2.4.1 Level I Data and Drift Scans . . . 26
2.4.2 Level II Data and Data Cubes . . . 31
2.4.3 Spectra and Cataloging . . . 34

3 Catalog and Statistics 36
3.1 Data Access . . . 36
3.2 The Catalog . . . 37
3.3 Statistics of the Catalog . . . 43
3.4 Positional Accuracy of Cataloged Sources . . . 46
3.4.1 Positional Differences between HI and Optical Sources . . . 50
3.4.2 Positional Errors as Derived from Radio Continuum Sources . . . 51

4 Unique Detections Toward the Virgo Cluster 58
4.1 Introduction . . . 58
4.2 Observations and Source Parameters . . . 59
4.3 Discussion . . . 70
4.3.1 Future Work: VLA Observations of Cloud 2 . . . 74

5 A HI Cloud Complex in Virgo 76
5.1 Virgo Cloud Complex . . . 82
5.1.1 Cloud Morphologies and Kinematics from ALFALFA data . . . 83
5.2 The Environment of the Cloud Complex . . . 89
5.3 Discussion . . . 95
5.3.1 A Gravitationally Stable Cloud? . . . 95

5.3.2 Interactions with the Cluster Environment 96
5.3.3 Tidal Effects and Timing Computations 98

6 The Virgo Environment 105
6.1 Introduction 105
6.2 The HI Mass Function 108
6.2.1 Computing the HI Mass Function 109
6.3 Simulating a Galaxy in a Cluster Environment 111
6.3.1 Initial Conditions and Methods of Simulation 112
6.3.2 Preliminary Results 116

7 Summary and Future Work 117
7.1 Overview 117
7.2 HI Clouds 118
7.3 Future Work 120
7.3.1 Galactic Neutral Hydrogen 120
7.3.2 High-Velocity Clouds 121
7.4 Future Endeavors 123

A Virtual Observatory 127
A.1 Introduction to the Data Access Layer: Cone Search Protocol 127
A.1.1 Service Query Requirements 127
A.2 Using Cone Search Client Applications 129
A.2.1 The Cone Search Specification 130
A.2.2 Examples of Using a Cone Search 130
A.3 3. Building a Simple Cone Service 136
A.3.1 Overview and Requirements 137
A.3.2 Testing and Returning the XML VOTable 144
A.4 4. Building a Simple SIAP Service 145
A.4.1 The Simple Image Access Protocol 145
A.4.2 Basic Input Parameters and Output 146
A.4.3 Other Service Input Parameters 147
A.4.4 VOTable Output 148
A.4.5 Setting up the SIAP Service 149
A.4.6 The Imaging Data Set 150
A.4.7 Setting up the Database 150
A.4.8 Testing and Returning the XML VOTable 155
A.5 Combining VO Services in a Data Reduction and Visualization Environment 157
A.5.1 Implementing the VO into a Large Scale Survey 157
A.5.2 Example GUI for SIAP 158
A.5.3 Usage in the ALFALFA Visualization Environment 161

LIST OF TABLES

1.1 HI Survey Comparison 12

2.1 ALFALFA Parameters 18

3.1 HI Candidate Detections 44

4.1 ALFALFA Optically Unseen Detections 62

5.1 Single-Dish Cloud Properties from the ALFALFA Survey 82
5.2 VLA Properties of C1 and C2 84
5.3 Timescale Relation Parameters 102

A.1 Required field UCDs 128

LIST OF FIGURES

1.1 PCCz Density and Scalar Velocity Renderings 2
1.2 Results of HI Surveys 13

2.1 The Arecibo Observatory 17
2.2 ALFA model response pattern 19
2.3 ALFA observed response pattern 20
2.4 Sample calibration solution 28
2.5 Calibration Diagnostics 29
2.6 Bandpass calibration 30
2.7 RFI Flagging Session 32
2.8 Spring Sky Grid Layout 34

3.1 Example HI Spectra 39
3.2 Virgo South catalog 47
3.3 Detection histograms 48
3.4 Catalog statistics 49
3.5 Catalog positional accuracy 1 52
3.6 Catalog positional accuracy 2 53
3.7 Catalog positional accuracy 3 54
3.8 Continuum pointing correction 1 55
3.9 Continuum pointing correction 2 56

4.1 Sky distribution of optically unseen detections 63
4.2 Optically Unseen HI Spectra 1a 64
4.3 Optically Unseen HI Spectra 1b 65
4.4 NGC 4254 HI Tail 67
4.5 UGC 8037 System 68
4.6 UGC 8037 Channel Maps 69
4.7 UV Plane Coverage 70
4.8 HI1208+1155 VLA Map 71

5.1 Virgo Cloud Complex Channel Maps 85
5.2 Virgo Cloud Complex Moment Maps 86
5.3 Virgo Cloud Complex Spectral Profiles 87
5.4 Virgo Cloud Complex Surface Brightness Limits 90
5.5 Virgo Cloud Complex Environmental Map 92
5.6 Vicinity of the HI cloud Complex 93
5.7 HI map of NGC 4424 94
5.8 Virgo Cloud Complex Dynamics Schematic 100

6.1 Virgo region detections for $cz_{\odot} \leq 3000$ km s^{-1} 106
6.2 Virgo region detections 107
6.3 Virgo position-velocity 108

6.4 Virgo HI mass function 110
6.5 Disk galaxy simulation 0° 113
6.6 Disk galaxy simulation 90° 114
6.7 Simulation disk gas loss 115

7.1 Galactic HI Map 122
7.2 High-Velocity Cloud Moment Maps 124
7.3 High-Velocity Cloud First Moment Map 125

A.1 Cone Search Results 136
A.2 Example GUI Application 162
A.3 GRIDView Application 163

CHAPTER 1

INTRODUCTION

1.1 Surveying Galaxies in the Universe

The study of the formation and evolution of galaxies is one of the most important endeavors in modern astrophysics. From studying the dynamics of individual galaxies, to statistical studies of millions of galaxies spanning large filaments and voids, we strive to understand everything about these large collections of stars, gas, and dust embedded in ubiquitous halos of dark matter. Observations of the nearby universe offer insight into the inner workings of galaxies, groups, and clusters, providing answers to crucial questions about evolution and environments. What dynamical interactions can be observed in nearby clusters? Do starless gas–rich, dark matter halos exist in high density, intermediate density, and void environments? Does a population of missing satellites exist in our own Local Group? The importance of a complete census of the various components of galaxies in the local universe at $z \sim 0$ is underscored by the need to understand galaxy evolution across a variety of environments throughout cosmic time.

Figure 1.1 shows a view of the local universe by rendering the galaxy density and velocity fields for a 120 Mpc box in supergalactic coordinates centered on the Milky Way. The renderings were derived from the Point Source Catalog Redshift survey (PSC*z*; Saunders et al. 1995; Schmoldt et al. 1999; Branchini et al. 1999), and are presented here to show the view of the universe afforded by redshift surveys. In addition, the PSC*z* view shows the large influence peculiar velocities can have on distance determinations, especially in nearby regions of large galaxian density.

In a cosmological context, observational studies of galaxies play an important role

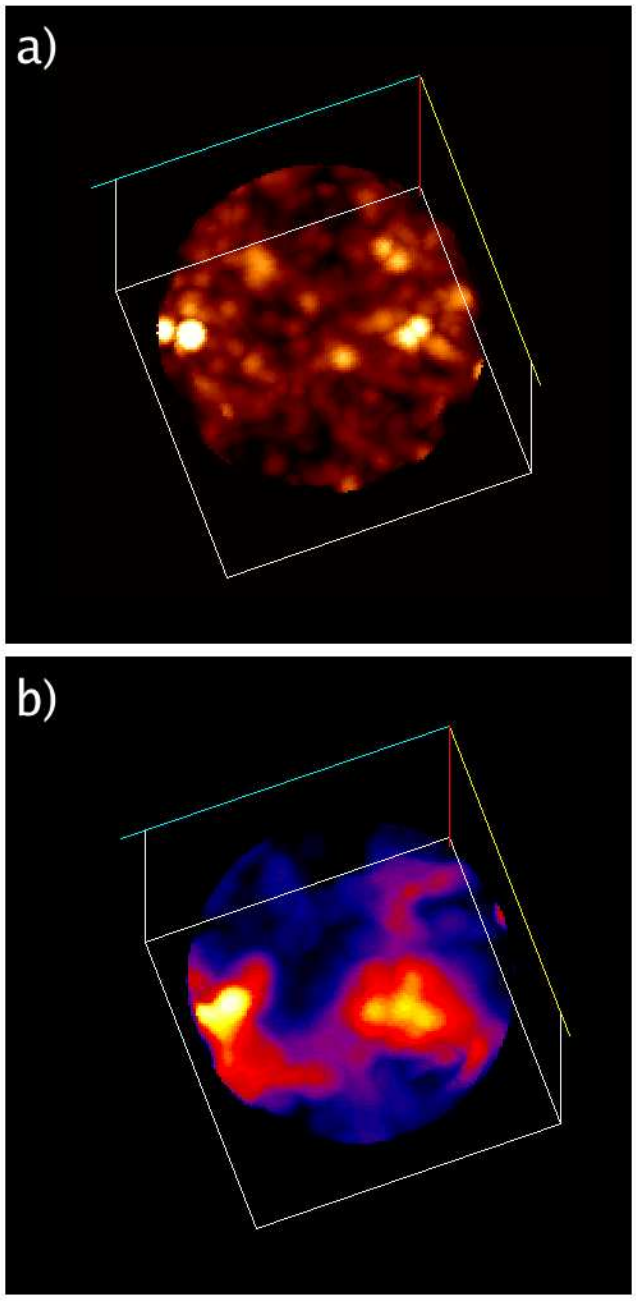

Figure 1.1: Three-dimensional renderings of the a) density and b) scalar velocity fields of the local universe. The images are derived by the author from the published catalogs of the Point Source Redshift Survey catalog (PSC*z*; Saunders et al. 1995; Schmoldt et al. 1999; Branchini et al. 1999). Each box is 120 Mpc on a side with the supergalactic X,Y, and Z axes indicated in yellow, aqua, and red respectively.

in understanding the continuous link between the earliest observable, the Cosmic Microwave Background (CMB), and the numerous galaxies around us at low redshift. Observations of the baryon acoustic oscillations following the Big Bang show the decoupling of the photon-baryon oscillation's imprint seen from the surface of last scattering. This was the initial seed of what was to become the large systems observed as galaxies (White et al. 1993). To date, the concordance model of Big Bang cosmology, known as Lambda-Cold Dark Matter (Λ-CDM; Blumenthal et al. 1984, 1985; Frenk et al. 1985), has been able to correctly predict not only the evolution of these primordial fluctuations, but also the large-scale distribution of matter in the universe (Spergel et al. 2007). As computing power and numerical algorithms have increased in tandem with the amount of data provided by large redshift surveys, the Λ-CDM formalism has been incorporated into into large-scale, high resolution N-body simulations. Results from these theoretical experiments predict more small satellite objects than are seen with current observational studies, especially in the vicinity of large galaxies in groups and clusters (Moore et al. 1999; Klypin et al. 1999). Hence, while the structure of the universe on large scales is well predicted in these scenarios, the details of the substructure in extragalactic populations remain unsolved.

Individual observations of galaxies across the electromagnetic spectrum have revealed a wealth of information about their morphology, kinematics, star formation rate, potential, and history. Large-scale extragalactic surveys, however, have become an increasingly important observational tool, not only for determining important cosmological parameters, but also for tracing the evolution of galaxies throughout cosmic time in environments of varying galaxian density. Numerous surveys with various scientific goals and observing techniques have been successfully completed at various wavelengths (see Huchra 1988; Giovanelli & Haynes 1991, for comprehensive reviews). The data provided by surveys continues to increase in both sheer cataloged numbers

of galaxies and in the individual attributed measurements. The Sloan Digital Sky Survey (SDSS[1]; York et al. 2000) and the Two-Micron All-Sky Survey (2MASS[2]; Skrutskie et al. 2006) in particular have revolutionized the amount of high quality multi-band imaging data available to astronomers. These surveys provide important information for luminosity functions, dust content, and redshifts from spectroscopic follow-up on high surface brightness targets. Redshift surveys utilizing both spectral line and photometric techniques give a three-dimensional view of the universe by providing preliminary Hubble flow distances. Twenty-one centimeter spectral line surveys for neutral hydrogen have the advantage of not only providing redshift information, but also kinematics and dynamics of galaxies. Extragalactic HI observations sample the cool gas content – an important tracer of interactions and the fuel for star formation. Blind HI surveys are sensitive to gas-rich, lower surface brightness objects; this population is not fully sampled by optical observations. These reasons clearly show how extragalactic HI surveys complement the stellar counterpart observations provided by optical and near-infrared surveys. There are many scientific benefits to studying the $z \sim 0$ universe, including that of probing both the low mass dwarf and high mass, low surface brightness regimes. A true, full sampling of the stellar, dust, and gaseous components at $z \sim 0$ and how they evolve with time is critical for understanding galaxy evolution.

[1]Funding for the Sloan Digital Sky Survey (SDSS) has been provided by the Alfred P. Sloan Foundation, the Participating Institutions, the National Aeronautics and Space Administration, the National Science Foundation, the U.S. Department of Energy, the Japanese Monbukagakusho, and the Max Planck Society. The SDSS Web site is http://www.sdss.org/. The SDSS is managed by the Astrophysical Research Consortium (ARC) for the Participating Institutions. The Participating Institutions are The University of Chicago, Fermilab, the Institute for Advanced Study, the Japan Participation Group, The Johns Hopkins University, Los Alamos National Laboratory, the Max-Planck-Institute for Astronomy (MPIA), the Max-Planck-Institute for Astrophysics (MPA), New Mexico State University, University of Pittsburgh, Princeton University, the United States Naval Observatory, and the University of Washington.

[2]This publication makes use of data products from the Two Micron All Sky Survey, which is a joint project of the University of Massachusetts and the Infrared Processing and Analysis Center/California Institute of Technology, funded by the National Aeronautics and Space Administration and the National Science Foundation.

1.2 Neutral Hydrogen

Following Karl Jansky's and Grote Reber's pioneering detections and preliminary mapping of cosmic radio waves, Jan Oort at Leiden Observatory interpreted the detected signals as continuum radiation (Jansky 1933; Reber 1944; Kraus 1966). It was Hendrick van de Hulst, at the suggestion of Oort, who first determined that neutral hydrogen (HI) in interstellar space was a likely source of radiation in the radio spectrum (van de Hulst 1945). Independent attempts by different teams confirmed his prediction with the first detection of neutral hydrogen in interstellar space (Ewen & Purcell 1951; Muller & Oort 1951). These events marked the beginning of observational HI astrophysics.

Photons emitted from neutral hydrogen result from a transition in the ground state energy level of the magnetic dipole orientation. The resulting photon has a frequency determined by

$$\nu_{10} = \frac{8}{3} g \left(\frac{m_e}{m_p}\right) (Rc)\, \alpha^2 \tag{1.1}$$

where the gyromagnetic ratio g =5.58569, m_e and m_p are the electron and proton masses respectively, the Rydberg constant R =1.097 $\times 10^6$ m^{-1}, c is the speed of light, $\alpha \equiv e/(\hbar c)$ is the fine-structure constant, and $\hbar \equiv h/2\pi$, where h is Planck's constant. The HI line has a rest frequency of ν = 1420.405751...MHz ($c/\nu = \lambda$ = 21.1 cm). This *hyperfine* transition occurs between triplet and singlet states when the magnetic dipole moment μ_{10} of the negative electron spin J_e changes from parallel to anti-parallel relative to the positive nuclear spin J_p. The emission probability is extremely low for neutral hydrogen. The Einstein A coefficient determines the rate of spontaneous transition to the lower energy state and is given by

$$A_{10} \approx \frac{64\pi^4}{3hc^3} \nu_{10}^3 |\mu_{10}|^2 \tag{1.2}$$

The value for the mean magnetic dipole moment for HI in the ground state is $\mu_{10} = e\hbar/2m_e c \approx 9.274 \times 10^{-24}$ Joules Tesla^{-1}. For hydrogen, $A_{10} = 2.876 \times 10^{-15}$ sec^{-1}.

Thus the radiative half-life timescale for spontaneous emission is $\tau_{1/2}$ ~11×10^6 years. However, the mean time between collisions in the interstellar medium (ISM) is much shorter than this half-life ($\langle\tau\rangle \sim 10^5$ years $<< \tau_{1/2}$). As a result, collisional excitation can maintain local thermodynamic equilibrium.

Neutral hydrogen is the most abundant element of the ISM, and is detectable along every line-of-sight in our Milky Way galaxy. The strength of this line is directly proportional to the number of hydrogen atoms for cases where the line is optically thin ($\tau << 1$), giving us an effective tool to measure the mass of atomic gas in astrophysical environments. It has proven to be a pivotal observational tool for understanding dynamic processes in galaxies, determining distance estimates, and measuring the full extent of galactic disks and other astrophysical phenomena.

1.3 Early Virgo Cluster Observations and Optical Surveys

The study of the Virgo Cluster arguably began with the listing of its principal large galaxies M49, M58, M59, M60, M61, M84, M85, M86, M87, M88, M89, M90, M91, M98, M99, and M100 in Charles Messier's famous catalog of nebulous objects in the year 1781. While much time would pass before a thorough census of the galaxies in Virgo was complete, Messier noted that many of the nebulae were near the constellation Virgo and Coma Berenices, as was pointed out in correspondence from Pierre Méchain (Messier 1781), the editor of the journal *Connaissance des Temps* at the time. Tammann (1985) outlined a comprehensive history of the astronomical studies of Virgo, and noted that German naturalist Friedrich Alexander von Humboldt wrote of a similar over density of cataloged nebulous objects in that region of sky in one of his volumes of *Kosmos* (Knobloch 2007).

The 20th century brought with it renewed interest in the study of the "island nebulae", as several hundred objects in the Virgo, Leo, and Coma Berenices regions of sky were cataloged, yielding accurate positions, sizes, and magnitudes obtained by various investigators (Schwassmann 1902; Hinks 1911, 1914; Shapley & Ames 1926, 1929, 1930a,b, 1932). These studies also began the preliminary separation of what is now known as the Virgo cluster from the Coma cluster and other background groups.

The diverse, morphological zoo of galaxy types in Virgo was first discussed by Hubble & Humason (1931) and also included the first redshift measurements for galaxies now known to be in the Virgo population. These morphology distribution studies were expanded by de Vaucouleurs (1961), extending further into the cluster's halo and outlying periphery. Smith (1936) examined radial velocity measurements for thirty-two Virgo Cluster "nebulae" and arrived at a virial mass for the cluster of 10^{14} $M_{\odot}$ for a distance of 2 Mpc (or $8.35{\times}10^{14}$ $M_{\odot}$ for a currently accepted distance of 16.7 Mpc). Interestingly enough, in determining a mass estimate Smith was the first to note the velocities of Virgo galaxies with respect to the cluster, stating, "*it is also reasonable to assume that the outermost particles move in circular orbits with a speed of 1500 km/sec.*" Shapley & Ames (1932) also noted the overdensity of bright galaxies around the core cluster centered around M87. The large velocity dispersion of the Virgo population is an important feature that continues to provide challenges in determining distances to galaxies in the cluster. With more radial velocity measurements obtained from optical spectroscopy during the mid 20th century, the structure and dynamics of Virgo and its various populations were characterized for the first time and compared to other, more distant clusters (Reaves 1956; van den Bergh 1960a,b; Markarian 1961; de Vaucouleurs 1961; Holmberg 1961).

Comprehensive reviews highlighting the challenges associated with classifying

Virgo galaxies and disentangling the fainter population from the background can be found in the literature (Zwicky 1959, 1957; de Vaucouleurs 1961, 1975; Abell 1975).

Much attention was given to Virgo due to the large galaxy at its core, as a polarized jet was discovered emanating from E0 galaxy M87 (Baade 1956; Baldwin & Smith 1956; Burbidge 1956; Hiltner 1959; Wade 1961; de Vaucouleurs et al. 1968). The jet emission and polarization was attributed to synchrotron radiation and was also detected in the radio continuum, cataloged with a flux density of 970 Janskys at a frequency of 178 MHz in the Third Cambridge Catalog (Bennett 1962). Further interest in Virgo was fueled by the X-ray detection and spectroscopy of M87 and the hot, intracluster gas throughout the cluster (Friedman & Byram 1967; Bradt et al. 1967; McClintock et al. 1969; Kellogg et al. 1971).

The first deep optical survey dedicated to Virgo was completed with the du Pont 2.5-m reflector at Las Campanas (Sandage & Binggeli 1984; Sandage et al. 1985b; Binggeli et al. 1985; Sandage et al. 1985a; Binggeli et al. 1987, 1993). This Virgo Cluster Catalog (VCC) covered the range $12^h < R.A. < 13^h$ and $0^\circ < Decl. < 20^\circ$ and has a limiting magnitude of $B \backsimeq 23.2$. The VCC has been used for luminosity function studies of the cluster, as well as membership determinations through kinematical analysis. The dwarf galaxy population was extensively cataloged with data from the VCC, building upon previous extensive studies by Reaves (1983).

The most recent optical study of the Virgo cluster has utilized the Advanced Camera for Surveys on the Hubble Space Telescope (Côté et al. 2004). The project has served as a focal point for multi-wavelength studies of various phenomena in and around the core E0 galaxy M87 (Jordán et al. 2004; Peng et al. 2006b,a). The surface brightness fluctuations technique (SBF) has also been used with the survey images for distance estimates and determination of the three-dimensional structure ($D_{M87} = 16.7 \pm 0.2$ Mpc

Mei et al. 2005, 2007).

1.4 Neutral Hydrogen, Virgo, and Surveys

Prior to HI studies of the Virgo cluster, neutral hydrogen had been detected in or limits placed on nearby galaxies in the local group and beyond (Heeschen 1957; Oort 1958; Dieter 1958; Field 1959a,b; Westerhout 1962; Dieter 1962c,a,b; Roberts 1962a; Davies et al. 1963). The first report of neutral hydrogen in Virgo was a purported Parkes telescope detection of HI absorption toward M87 (Robinson et al. 1963; Koehler & Robinson 1966). This claim was later refuted with observations from Nançay (Allen 1968). Fixed horn antenna observations with a 10° beam were used to derive an upper limit to the antenna temperature relative to regions outside the cluster (Goldstein 1966b,a). The first small HI survey examined 18 Virgo cluster galaxies and claimed detections for eight (Robinson 1965). Further studies by Davies & Lewis (1973) and Bottinelli & Gouguenheim (1974) examined HI detections and asserted the idea that Virgo cluster galaxies were deficient in HI when compared to field galaxies (Davies 1968), though interpretations as to the cause differed at that point. Attention was given to both field galaxies and those in clusters, as well as the first HI studies based on morphological selection characteristics. Global HI profiles obtained with the Parkes 210 ft., Effelsburg 100-m, Nançay, Green Bank 300 ft., and Green Bank 140 ft. focused on both the early and late type galaxy populations (Osterbrock 1960; Roberts 1962b, 1972; Lewis & Davies 1973; Bottinelli et al. 1973; Krumm & Salpeter 1976), while the landmark paper by Gunn & Gott (1972) examined physical effects (e.g., ram pressure stripping) on galaxies in a cluster environment.

The 1970's upgrade to the Arecibo radio telescope gave the primary reflector a sur-

face accuracy suitable for high frequency observations ($\nu > 1$ GHz), including those for 21-cm spectral line work (Drake 1971; Lalonde 1974). Arecibo is well suited for targeted HI studies of galaxies. An optically selected sample of 84 E, S0, and Sa galaxies yielded 18 detections in HI and, with the superior resolution of Arecibo, provided estimates of the spatial distributions of extended disks for five Virgo cluster objects (Krumm & Salpeter 1976, 1979). Arecibo's high sensitivity allowed not only the detection of the cool, neutral gas content of galaxies in Virgo, but also yielded redshifts as well. As a sensitive "redshift machine", Arecibo excelled at mapping Virgo, determining galaxy memberships, and understanding the velocity distribution of the different morphological types within the cluster (Helou et al. 1979; Hoffman et al. 1980; Cornett & Smith 1981; Helou et al. 1981; Cornett & Smith 1981; Kraan-Korteweg 1982; Warmels & van Woerden 1983). In particular, the late-type spiral population of Virgo was shown to be deficient in HI and revealed important evidence on the effects of galaxy interactions with the hot, intracluster medium (ICM; Chamaraux et al. 1980; Giovanardi et al. 1983; Giovanelli & Haynes 1983; van Gorkom et al. 1984a; Balkowski et al. 1985; Haynes 1985; Giovanelli 1985). Evidence for these galaxy-ICM interactions was shown through "*a strong correlation between HI deficiency and cluster X-ray luminosity, rather than local galaxy density*" through the studies by Haynes & Giovanelli (1986), which examined the pattern of HI deficiency within 5° of the Virgo core with a sample of 160 galaxies.

The Very Large Array (VLA) complemented single-dish observations, providing resolved maps and HI surface density measurements for small samples of previously HI detected point sources. These studies showed the physical asymmetries in the HI disks due to ram pressure stripping of Virgo Cluster galaxies (van Gorkom et al. 1984a,b). VLA atlases of a Virgo sample observed truncated HI disks relative to their optical counterparts for bright spiral galaxies within 3° of M87 (Cayatte et al. 1990), a feature previously discovered with Arecibo (Giovanelli & Haynes 1983). The fact that different

galaxies are affected differently by the cluster, combined with the HI deficiency pattern studies revealed a wealth of new information about galaxy evolution in a cluster environment (Guhathakurta et al. 1988; Cayatte et al. 1994).

In addition to studying the larger bright galaxies in the context of the global cluster environment, observations of the population of physically smaller dwarfs provided information on star formation rates (Hoffman et al. 1989a). Dwarf galaxies make up the largest population in Virgo with over 850 cataloged members (Binggeli et al. 1987). Of particular interest in the history of Virgo HI observations and relevance to this dissertation is the study of the low surface brightness (LSB) dwarf population and other optically faint (or optically invisible) gas-rich detections (Hoffman et al. 1992). The serendipitous discovery of HI1225+01 in the Virgo southern extension (and optical counterpart for the northeast component) revealed a HI bridge between an LSB dwarf and a starless, gas-rich cloud (Giovanelli & Haynes 1989; Impey et al. 1990; Giovanelli et al. 1991; Salzer et al. 1991; Chengalur et al. 1995).

Work completed by Fukugita et al. (1993) and Solanes et al. (2001, 2002) has examined Virgo's three-dimensional structure by studying the HI deficient spiral population via the Tully-Fisher relation (Tully & Fisher 1977). Complementary studies to the late-type spirals have examined the HI content of early-type galaxies (ETGs; di Serego Alighieri et al. 2007), the origin of the larger population of dwarf ellipticals (Boselli et al. 2008), and comparisons of the HI content to optical imaging (Gavazzi et al. 2008). Reviews of developments in extragalactic neutral hydrogen studies (not limited to the Virgo cluster) can be found in Roberts (1975), Haynes et al. (1984) and Giovanelli & Haynes (1988).

The efforts of large-scale wide-field HI surveys is aimed, in part, at finding detections of similar nature to HI1225+01. While survey goals vary depending on the project

Table 1.1: HI Survey Comparison

Survey	Coverage deg^2	Beam arcmin	*cz* range km s^{-1}	V_{res} km s^{-1}	t_s sec	RMS mJy	N_{det} -	min($M_{HI}/M_\odot$) W_{50} = 30 km s^{-1} at 10 Mpc	Reference -
(1)	(2)	(3)	(4)	(5)	(6)	(7)	(8)	(9)	(10)
AHISS	65	3.3	-700 - 7400	16	var	0.7	65	1.9×10^6	Zwaan et al. (1997)
ADBS	430	3.3	-650 - 7980	34	12	3.6	265	9.9×10^6	Rosenberg & Schneider (2002)
WSRT	1800	49.	-1000 - 6500	17	60	18	146	4.9×10^7	Braun et al. (2003)
Nançay CVn	800	4×20	-350 - 2350	10	80	7.5	33	2.0×10^7	Kraan-Korteweg et al. (1999)
HIJASS	1115	12.	-1000 - 10000	18	400	13	222	3.6×10^7	Lang et al. (2003)
HIJASS-VIR	32	12.	500 - 2500	18	3500	4.	31	1.1×10^7	Davies et al. (2004)
HIDEEP	60	15.5	-1280 - 12700	18	9000	3.2	173	8.8×10^6	Minchin et al. (2003)
HIZSS	1840	15.5	-1280 - 12700	27	200	15.	110	4.1×10^7	Henning et al. (2000)
HIPASS	21341	15.5	300 - 12700	18	450	13.	5315	3.6×10^7	Meyer et al. (2004); Zwaan et al. (2004); Wong et al. (2006)
AUDS	0.4	3.5	-960 - 47000	TBD	70×3600	0.02	(40)	0.6×10^6	Freudling et al. (2005)
AGES	TBD	3.5	-960 - 19000	TBD	300	0.5	TBD	1.4×10^6	Auld et al. (2006)
ALFALFA	7000	3.5	-2000 - 18000	11	48	1.6	> 25000	4.4×10^6	Giovanelli et al. (2005b)

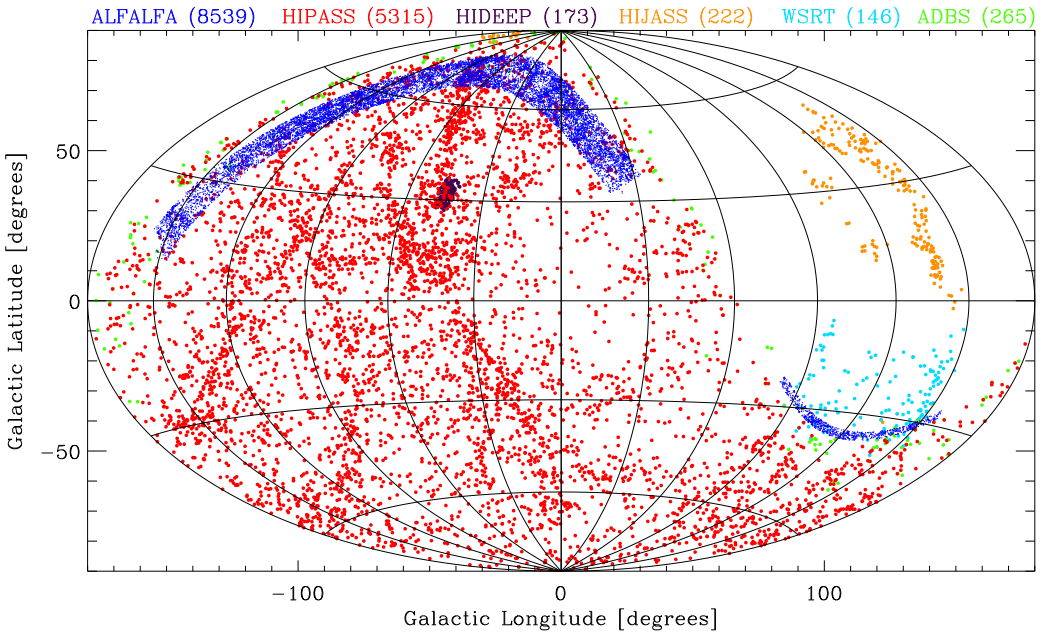

Figure 1.2: Detections from various HI surveys plotted in an equal-area Aitoff projection in galactic coordinates. Catalogs are shown for ALFALFA (blue; Giovanelli et al. 2007; Saintonge et al. 2008; Kent et al. 2008), HIPASS (red; Meyer et al. 2004; Zwaan et al. 2004; Wong et al. 2006), HIDEEP (purple; Minchin et al. 2003), HIJASS (orange; Lang et al. 2003), WSRT (cyan; Braun et al. 2003), and ADBS (green; Rosenberg & Schneider 2002).

strategies and telescope strengths, detecting LSB and optically inert phenomena in environments of different galaxian density remains an exciting prospect. *L*-band multi-beam receivers have revitalized single-dish radio astronomy into a new observation paradigm, generating large data sets for dissemination among large distributed teams (Szalay et al. 2001). The Jodrell Bank, Parkes and, most recently, Arecibo Telescopes have utilized these receiver systems to great efficiency. Table 1.1 describes past, present, and future HI surveys conducted with a variety of telescopes, adopted from the Arecibo Legacy Fast ALFA survey white paper (Giovanelli & Haynes 2003). The column descriptions are as follows:

1. The survey project name.

2. The survey sky coverage in units of square degrees.
3. The survey beam size in arcminutes.
4. The approximate heliocentric redshift range covered by the total survey bandwidth. Radio frequency interference gaps are noted for HIJASS in the range 4500-7500 km s^{-1}. The AUDS and AGES ranges assume the usage of the new extragalactic spectrometer at Arecibo.
5. The velocity resolution at the frequency of the HI line in km s^{-1}, after Hanning smoothing.
6. The effective integration time per beam area in seconds.
7. The root-mean-square(RMS) noise per beam of the survey in millijanskys, for a velocity width of 10 km s^{-1}.
8. The actual or predicted number of detections for the survey.
9. The minimum detectable HI mass at 10 Mpc with a 5σ detection of full-width half-max velocity width of 30 km s^{-1}.
10. The literature reference for the survey parameters.

1.5 Overview of the Dissertation

This Ph.D. dissertation builds on the earlier work describing results from the Arecibo Legacy Fast ALFA (ALFALFA) survey, a large-scale 21-cm line extragalactic radio survey utilizing the Arecibo *L*-band Feed Array seven-element receiver. In particular, this work focuses on the area of sky encompassing the Virgo Cluster of galaxies, the catalogs produced by the survey, and follow-up observations conducted with Arecibo and with the Very Large Array for some of the new and unique detections. The questions addressed by this dissertation are as follows:

- What are the global HI characteristics of the Virgo Cluster?
- How can the detections of low mass, optically dark HI clouds be characterized?
- Is the formation of such clouds the result of a dense cluster environment with intracluster gas, and (obviously) large gravitational potential?
- Do population diagnostics like the HI mass function vary with environment?

Chapter 2 discusses the observational scheme and technical details of the extragalactic survey. Chapter 3 discusses the catalog of the Virgo region and beyond cultivated from the data sets. Chapter 4 discusses Arecibo and VLA detections of extragalactic objects exhibiting no apparent optical counterpart. Chapter 5 discusses one of the more interesting HI cloud complexes in Virgo. Chapter 6 discusses several initiatives aimed at understanding the Virgo environment, including the HI mass function and simple computer simulations of a disk galaxy in a cluster potential. Chapter 7 concludes the dissertation and outlines future work. Appendix A describes programming and tutorial contributions to the Virtual Observatory project.

CHAPTER 2

THE ARECIBO LEGACY FAST ALFA SURVEY

The Arecibo Legacy Fast ALFA (ALFALFA; Giovanelli et al. 2005b) survey is a large extragalactic HI project using the 305-meter radio telescope of the National Astronomy and Ionosphere Center, located on the island of Puerto Rico (Figure 2.1). The survey utilizes the new 7-element Arecibo *L*-band Feed Array (ALFA) to conduct a HI spectral line survey covering 7000 square degrees of sky at high Galactic latitude. ALFA facilitates large-scale surveys such as ALFALFA by enabling users of the Arecibo telescope to conduct observations seven times faster than with a traditional single pixel receiver. The survey will provide a cosmologically fair sampling of the local universe, with the spectral bandpass covering the redshift range $cz_{\odot} \lesssim 18000$ km s^{-1}. ALFALFA surpasses the observational limits of previous first generation HI surveys such as the HI Parkes All Sky Survey (HIPASS; Barnes et al. 2001) and the Arecibo Dual Beam Survey (ADBS; Rosenberg & Schneider 2002). The second generation ALFALFA survey improves upon sensitivity, bandwidth, and both spatial and spectral resolution; it will be the dominant HI data source until the implementation of next generation radio telescopes such as the Square Kilometer Array. This chapter describes the survey science germane to this dissertation, the observing strategy and implementation, and the data reduction process. The resulting catalog of the Virgo cluster and surrounding periphery are described in Chapter 3.

2.1 The Arecibo *L*-band Feed Array

With the upgrade of Arecibo during the 1990's, it became possible for the telescope to accommodate focal plane arrays in contrast to the line feeds that had been used with the telescope throughout its prior history (Kildal et al. 1993). The new Gregorian op-

Figure 2.1: The Arecibo Observatory, home to the world's largest radio telescope. The primary reflector diameter is 305-meters. Photo taken by the author from N8423M piloted by Professor D. Kornreich.

tical system greatly improved the telescope's sensitivity and frequency coverage with a host of new receiver systems. The Arecibo *L*-band Feed Array system (ALFA, built by Parkes/CSIRO under contract from NAIC), is a 7-element feed array with a spectral bandwidth response over the range 1225-1525 MHz. Each element of the receiver is a stepped TE_{11} mode dual linear polarization feed horn that is 25 cm in aperture (Cortés-Medellin 2002). Six feed horns are arranged in a hexagonal pattern with the seventh feed at the center.

Figure 2.2 shows the theoretical ALFA power response pattern projected on the sky. The feed arrangement and Gregorian optics result in the beam pattern projecting a set of seven ellipses (axis ratio $a/b = 1.15$) arranged in a hexagonal pattern. At the half-power response level, the beams are of sizes 3′.8 in the zenith angle direction and 3′.3 in the

azimuth direction. Figure 2.2 also shows the combined sidelobe structure of the response pattern. The high sidelobes must not be neglected in any Arecibo observation near strong and/or extended sources, including continuum sources or high–velocity clouds. Special care is taken in these situations to ensure that spurious detections are not included in catalogs. The central beam's first sidelobe appears at 3% of the peak (-15 dB), and the asymmetric outer beams range from 16-20% of the peak response (-7 to -8 dB). The individual beam structures are shown in Figure 2.3. These images were made with cross scans of the continuum radio source 3C 138 near meridian transit. The feed can be rotated about the central feed, as will be described in the observing scheme in the next section.

Table 2.1: ALFALFA Parameters

Parameter	**Value**
Beams	7
Polarizations	2
Beam size	$3'.8 \times 3'.3$
Gain	11 K/Jy (Beam 0) and 8.5 K/Jy (Beams 1-6)
$T_{\rm sys}$	26-30 Kelvin
Frequency range	1335-1435 MHz
$cz_{\odot}$ range	-2000 to 17912 km s^{-1}
Bandwidth	100 MHz
Correlator Lags	4096
Channel spacing	24.4 kHz (5.1 km s^{-1} at ν = 1420.4058 MHz)
Autocorr sampling	3 level
Channel RMS	2.0 mJy/channel
Map RMS	1.86 mJy/beam
Effective Map t_{int}	48 sec (beam solid angle)$^{-1}$
5σ survey sensitivity	0.72 Jy km s^{-1} for W$_{F50}$=200 km s^{-1} at t_{int}
Drift scan coverage	10 minutes $\times$ 14.5′ (all beams)
Drift scan size on disk	213 MB
Grid sky coverage	2.4×2.4 degrees
Grid $cz_{\odot}$ coverage	a) ~-2000 to 3300 km s^{-1} b) ~ 2500 to 7950 km s^{-1} c) ~ 7200 to 12800 km s^{-1} d) ~12100 to 17900 km s^{-1}
Grid cz overlap	140 channels
Grid size on disk	381 MB

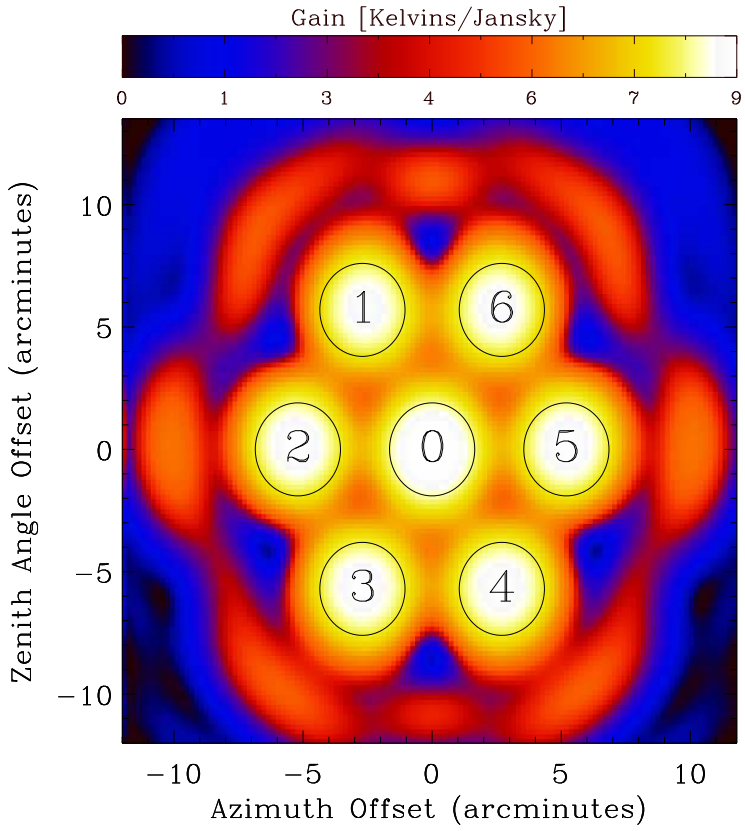

Figure 2.2: ALFA multibeam receiver model response pattern. The peak gain of the central beam zero is ≃11 Kelvins Jansky^{-1}. The peak of the six outer beams is ≃8.5 Kelvins Jansky^{-1}. Note the elliptical shape of the beam due to the illuminated area of of the primary reflector coupled with the Gregorian optics. The black ellipses trace the half-power response of each numbered beam. Data kindly provided by Cortés-Medellin (2002).

2.2 Survey Sensitivity and Detection Thresholds

Care must be taken in a detailed study of the survey parameter space to optimize the design and implementation and, as a consequence, the detection limits. The following analysis details the relations needed to understand the survey limits (Giovanelli et al. 2005b). The ALFALFA survey parameters are listed in Table 2.1. The theoretical root mean square (RMS) noise per channel (or System Equivalent Flux Density; SEFD) is

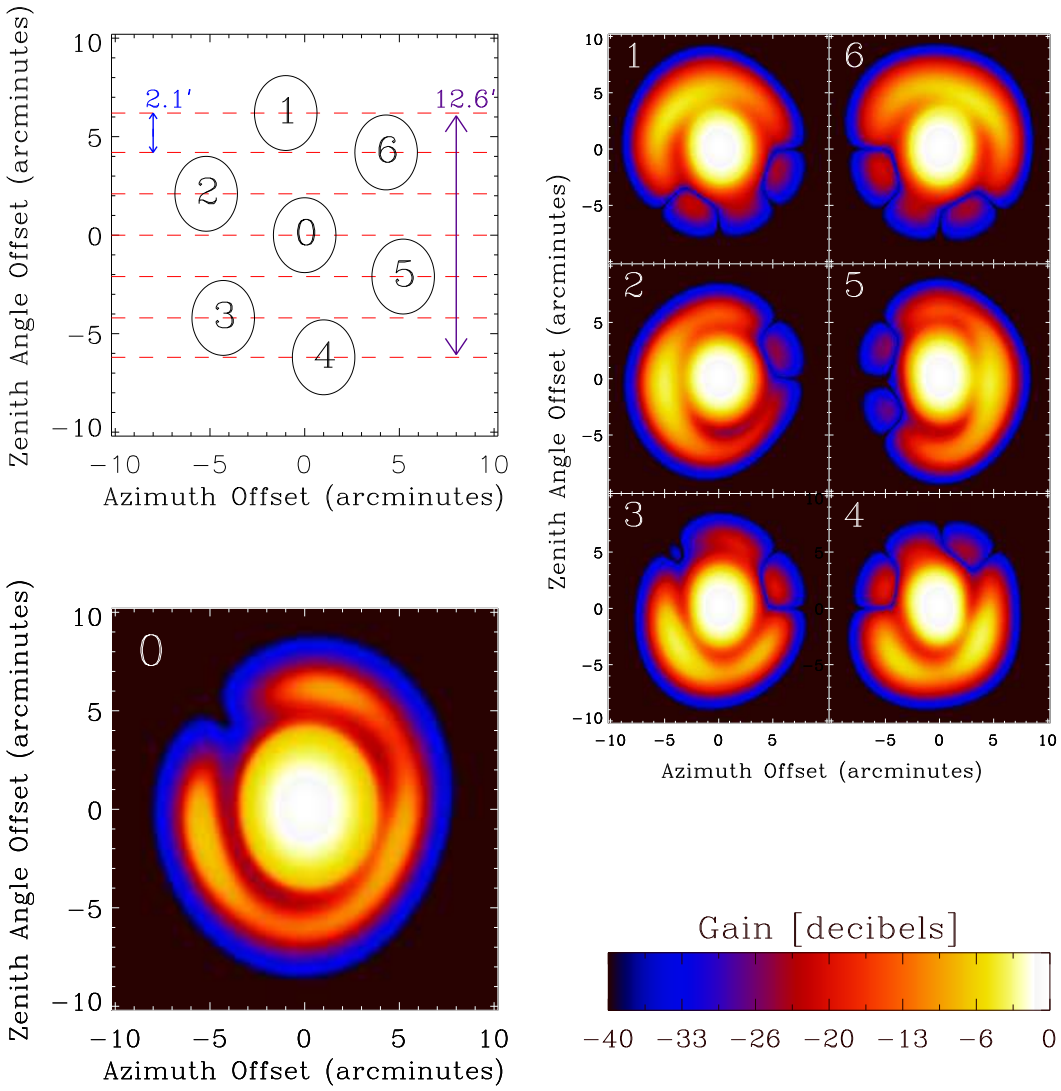

Figure 2.3: ALFA multibeam receiver observed response pattern. The upper left corner shows the 19° rotation of the ALFA beams at the -3 dB level when the azimuth arm is aligned along the local meridian. The remaining plots show a histogram equalization of color intensity images for each beam when observing the continuum radio source 3C 138 near meridian transit. Data kindly provided by Phil Perillat of NAIC.

computed via the radiometer equation

$$\sigma_{rms} = \frac{T_{sys}/G}{\sqrt{2\Delta\nu t_s f}} \tag{2.1}$$

where T_{sys} is the system temperature in units of Kelvins, G is the gain in units of Kelvins Jansky^{-1}, $\Delta\nu$ is the channel bandwidth in units of Hertz, t_s is the integration time in seconds, and f is a factor that takes into account other instrumental and processing effects. T_{sys}/G varies between 2.65 and 3.40 Jy. For this analysis, a value of 3.25 Jy is used. The factor of two in the denominator square root accounts for the addition of both polarizations in the noise computation. The f factor can have multiple components due to 1) spectral smoothing, 2) the switching technique applied for the subtraction of the bandpass and 3) other factors including clipping losses from autocorrelation $f = f_{smo} f_{switch} f_{other}$. The spectral smoothing factor f_{smo} is proportional to the width of the spectral smoothing function W_{smo}, with the remaining factors $f_{switch} f_{other} \backsimeq 0.7$.

Assuming a source is optically thin, the HI mass in solar masses of a source is given by the relation (Roberts 1975):

$$\frac{M_{HI}}{M_\odot} = 2.356 \times 10^5 D_{Mpc}^2 \int S(V)\, dV \tag{2.2}$$

where D_{Mpc} is the distance in megaparsecs, V is the Doppler velocity in km s^{-1}, and $S(V)$ is the flux density as a function of velocity in Janskys. The first order approximation of this relation can be written as

$$\frac{M_{HI}}{M_\odot} = 2.356 \times 10^5 D_{Mpc}^2 S_{peak} W_{kms} \tag{2.3}$$

where S_{peak} is the peak spectral line flux in Janskys, and W_{kms} is the full-width half-maximum velocity width in km s^{-1}.

The signal–to–noise ratio (S/N) must exceed a certain threshold value to be considered a detection in any area of signal processing. The detection limit for the survey is

soft, however, a S/N of $\sim$ 6 is typically used as a threshold value for valid, detected sources in the ALFALFA survey.

For a channel bandwidth $\Delta\nu$ = 24,400 Hertz, the theoretical S/N is given by

$$S/N = \frac{f_\beta S_{peak}}{\sigma_{rms}} \backsimeq 2.44 \times 10^{-4} f_\beta \, (f_{smo} t_s)^{1/2} \, M_{HI} W_{kms}^{-1/2} D_{Mpc}^2 > 6 \tag{2.4}$$

where the parameter definitions are the same as in Equations 2.2 and 2.3. The attenuation of the source flux via beam dilution is also taken into account with the factor $f_\beta \leq 1$. The detection threshold defined in Equation 2.4 works well for signals with narrow velocity widths. For broad spectral lines, however, two important facts must be taken into consideration: 1) S_{peak} is depressed when smoothing signals, as the shape of spectral profiles is not rectangular at the specified spectral resolution and 2) The smoothing of broad signals ($\sim$ several hundred km s^{-1}) does not reduce the noise in proportion to $\sqrt{W_{kms}}$ (Giovanelli et al. 2005b; Rosenberg & Schneider 2002). Smoothing will increase the S/N up to $W_{kms} \backsimeq 400$ km s^{-1}, but will not significantly do so beyond that threshold. The criterion given in equation 2.4 can be written and parameterized to take these facts into account as

$$5.2 f_\beta t_s^{1/2} \left(\frac{M_{HI}}{10^6 M_\odot} \right) D_{Mpc}^{-2} \left(\frac{W_{kms}}{400} \right)^\gamma > 6 \tag{2.5}$$

where the exponent is defined as

$$\gamma = \begin{cases} -1/2 & \text{for } W_{kms} < 400 \text{ km s}^{-1} \\ -1 & \text{for } W_{kms} \geq 400 \text{ km s}^{-1} \end{cases} \tag{2.6}$$

Equation 2.5 can be used to obtain the minimum detectable HI mass:

$$\left(\frac{M_{HI}}{10^6 M_\odot}\right) = 0.49\, f_\beta{}^{-1} D_{Mpc}^2 t_s{}^{-1/2} \left(\frac{W_{kms}}{400\ \mathrm{km\ s^{-1}}}\right)^{-\gamma}, \tag{2.7}$$

and the integration time required to detect a source of HI mass M_{HI} and width W_{kms} at a distance D_{Mpc} with the ALFA receiver,

$$t_s \backsimeq \frac{1}{4} f_\beta{}^{-2} \left(\frac{M_{HI}}{10^6 M_\odot}\right) \left(D_{Mpc}\right)^4 \left(\frac{W_{kms}}{400\ \mathrm{km\ s^{-1}}}\right)^{-2\gamma}. \tag{2.8}$$

The important consequences from these relations described by Giovanelli et al. (2005b) can be summarized as follows:

1. Arecibo is well suited to extragalactic surveys, as the volume sampled scales with the reflector diameter for a fixed integration time.
2. The number of HI clouds detected is linearly proportional to the sampled survey volume. Because the sampled survey volume over a survey solid angle Ω_{survey} is $V_{survey} = \Omega_{survey} D_{max}^3/3$, the number of detections can be increased by increasing the survey volume or the maximum distance.
3. From equation 2.8, it is known that for a given HI mass, the maximum detectable distance is proportional to $t_s^{1/4}$. Since the total number of line of sight beams to cover is simply $\Omega_{survey}/\Omega_{beam}$, then the total survey time is $t_{survey} \propto (\Omega_{survey}/\Omega_{beam}) t_s$.
4. $t_{survey} \propto V_{survey} t_s^{1/4}$. Once an HI mass is detectable at an distance required by the survey goals, it is more advantageous to increase the total survey area Ω_{survey} than it is to increase the integration time per beam solid angle.

2.3 Observations

Arecibo's fixed primary reflector can observe between declination -2°and 38°. The ALFALFA survey uses a meridian transit, fixed azimuth drift scan observation mode. For the catalogs presented in this work, the azimuth arm of the platform is aligned along the local meridian (North or South of zenith depending on the area of sky), and the Gregorian dome is moved along the elevation arm to observe a particular declination track. Data is taken as the sky drifts by. In the near future, a different telescope configuration will be used for high zenith angle positions in the 16° to 20° declination range, as the dome cannot be positioned within |Z.A.| $<$ 1.7°. The optimal rotation angle for maximum declination coverage by ALFA when positioned on the meridian is 19°. The seven drift scan tracks cover a range of 14′.5 and are spaced by 2′.1 in declination. Configurations in this observing mode are shown in the upper left corner of Figure 2.3. During observations, small corrections are applied in zenith angle to keep the telescope pointing along the epoch J2000 declination track as opposed to the current declination. The constant beam orientation also yields a fixed beam pattern when data cubes are generated from the drifts.

The receiver output is transmitted to the digital signal processing (DSP) instruments via the fiber-optic intermediate frequency system (IF). The WAPPs (Wideband Arecibo Pulsar Processor) serve as the digital autocorrelation spectrometer backend, consisting of four processing units that each handle both polarizations of two ALFA beams. Data files are composed of drift scans that cover 10 minutes in right ascension. Data are recorded at a 1 Hz rate, hence each file contains 600 one-second records, and each record consists of fourteen spectra (7 beams x 2 linear polarizations). Data produced by the WAPP are recorded with a 3-level sampling of the autocorrelation function, and the resulting spectra consist of 4096 lags covering a bandwidth of 100 MHz. The extra

"half" WAPP processing unit is used to monitor radio frequency interference. Data are written to disk in the *Flexible Image Transport System* (FITS) format (Hanisch et al. 2001).

Observations use the *Control Interface Module for Arecibo* (CIMA) interface written originally by Jeff Hagen and subsequently maintained and expanded on by Mikael Lerner. Automated Tcl/Tk scripts are used to configure the telescope receiver, rotation angle, and backend. At the end of each 10 minute drift scan, observing is interrupted for approximately 5 seconds, and a solid-state noise diode signal of known intensity is injected into the signal path for 1 second. This signal is later used for calibration during data processing. The 5 second gap between the 600 second drifts amounts to approximately one-third of a beamwidth in right ascension. Observations are monitored in real time via a live time/frequency plot for each beam and polarization.

The project takes a minimalist approach in terms of changing system parameters during the course of observations. Keeping the telescope stationary removes the need to slew the telescope, save for the beginning of the observing run. The drift transit strategy and constant rotation angle of 19° keep the gain from varying. The system temperature also remains relatively constant for a given observing run typically lasting 6 to 10 hours. No Doppler tracking is applied to the LO frequency. The data analysis, including bandpass calibration and generating regularly gridded data cubes, is greatly simplified because of the fewer telescope configuration parameters to disentangle. The observing scheme allows for a 97% "open shutter" time for allocated observing (99% of total observing time), vastly increasing the amount of data applied to astronomical sciences by survey team members.

ALFALFA uses a two-pass strategy by gathering two epochs of data in the same area of sky. Three to nine months after any given drift scan is taken, a second drift

scan is taken for the same area of right ascension, offset by 7′18″ in declination. This minimizes any scalloping due to gain differences between the central and outer beams (T_{sys}/G varies between 2.65 and 3.40 Jy). The combination of the first and second passes yields a spatial sampling of $\sim 1'$ in declination. The two-pass observing strategy offers advantages in contrast to scanning a piece of sky only once. These include:

- *Radio transients*. Identification of radio continuum sources varying across multiple epochs. Comparisons can be made with flux measurements from the NRAO VLA Sky Survey (NVSS) database (Condon et al. 1998).
- *Signal identification*. Spurious signals caused by RFI are unlikely to appear in two separate passes of the same region of sky. Higher spatial sampling from interleaving drifts allows the survey to improve its sensitivity threshold.
- *Hardware failure/maintenance*. Data lost through failure of a whole beam or single polarization can leave gaps in sky coverage; a second pass can partly fill the gaps.

2.4 Data Reduction

2.4.1 Level I Data and Drift Scans

All data reduction is completed in the *Interactive Data Language* (IDL) software published by ITT Visual Information Solutions. IDL is a dynamically typed, single namespace language with advanced graphics capabilities commonly employed in space science research. The procedure library developed by Arecibo staff member Phil Perillat has proved incredibly valuable to the project, and the ALFALFA software reduction

pipeline has been based on his routines for processing data from the WAPP backend.

The initial FITS format files written to disk are first converted to array structures and saved in the native IDL format. Each "drift" or *d* file is a 2 by 600 by 8 element array. In each array element, a large IDL structure is built with the original FITS header information, high-precision position, and time stamp information, as well as a 4096 channel array containing the raw spectrum. The 8th array "beam" element carries redundant data. Each one-second calibration record from the noise diode injection is written to a identical structure type, and saved in its own CALON file. An "off" calibration record is created from the final and first records of two adjacent drift files, and is also saved in its own CALOFF file. The series of 600 second drift and calibration "triplets" file lists are created with scan number prefixes for import into the calibration pipeline. A temperature calibration ratio is computed by taking the cal values at 1400 MHz and dividing by the difference of the average total power for both the CALON and CALOFF files. This is performed for each calibration file, beam, and polarization. A sample calibration ratio for beam 0 and polarization A as well as the system temperature T_{sys} during an observing run is shown in Figure 2.4.

Bandpass subtraction is performed on 2D time/frequency plots, one map at a time on each polarization and beam for a given drift file. The calibration process begins by performing a robust linear fit along the time dimension for each frequency channel. The RMS is also computed for each channel, as is the fraction of time series records less than $2 \times$ RMS. After exclusion of outliers that deviate more than $2 \times$ RMS from the fit, a bandpass value of either (1) the zeroth order coefficient to the linear fit c_0, or (2) the median value of the strip is selected. This option is chosen by the user at the time of reduction. Based on experience, option 1 is usually preferable. The RMS as a function of channel is iteratively fit with a 3rd order polynomial. Channels (including

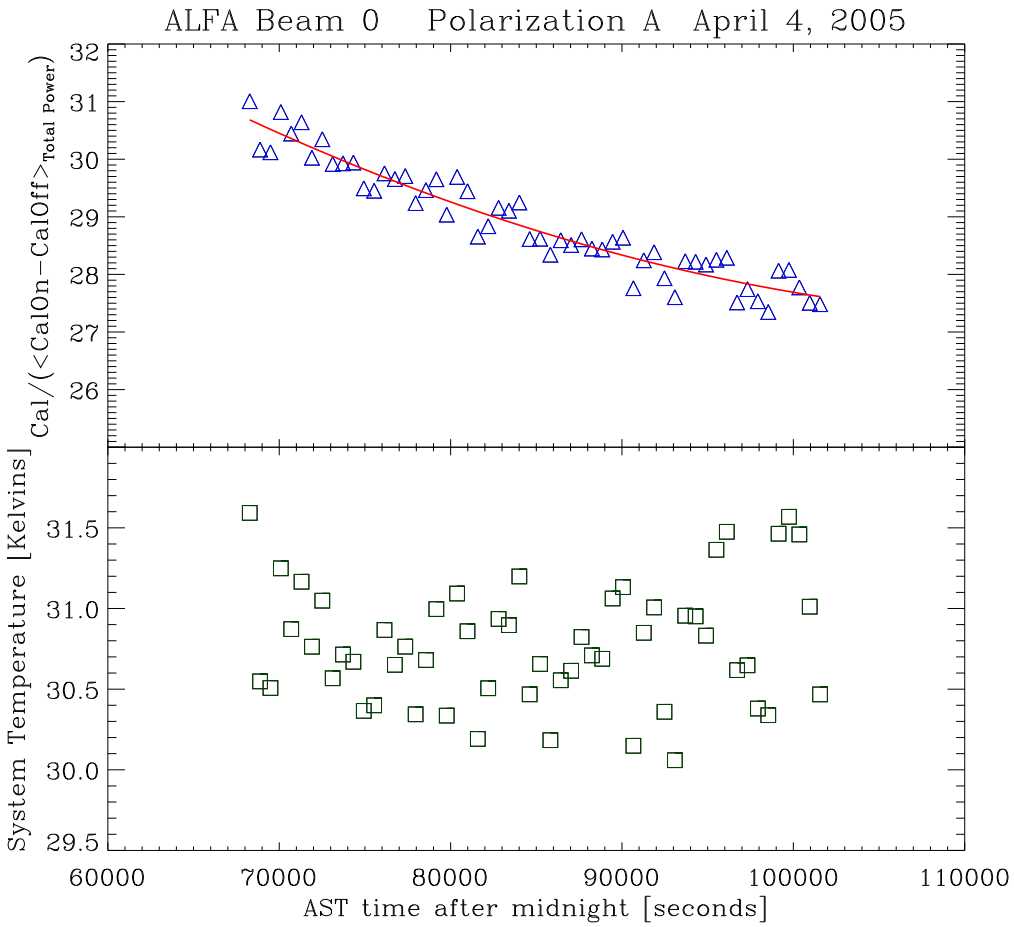

Figure 2.4: Sample calibration solution for the observing session on April 4, 2005. The upper plot shows the calibration ratio Cal/(TP_{calon}-TP_{caloff}) and a third order polynomial fit to the data. The lower plot shows the system temperature during the observing run.

those at the bandpass edges) are flagged that deviate several standard deviations from the fit. In addition, channels are manually flagged, such as those around galactic HI. A cubic spline is used to interpolate the bandpass across the flagged channels . An "off" bandpass is created as the normalized bandpass times the system temperature. A background total power continuum value is also computed for all time series records for all records and channels that have not been flagged, excluding point sources; the continuum contribution from these point sources is also stored away. Figure 2.5 shows the diagnostics of the described calibration process. The final calibrated and corrected

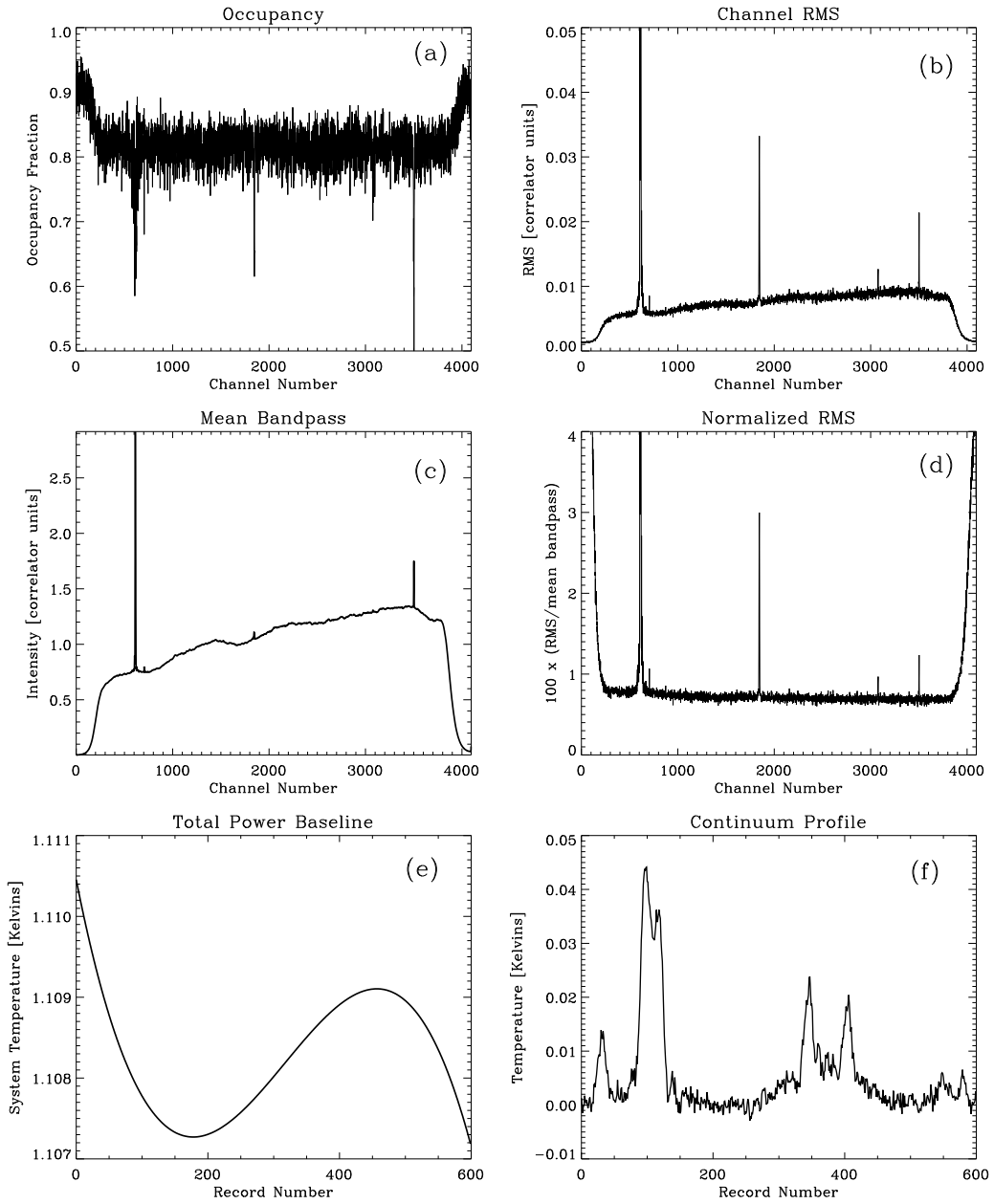

Figure 2.5: Plots showing the products, statistics, and diagnostics of the bandpass calibration for a single drift. (a) shows the occupancy fraction of records that are within $2 \times$ RMS of the time series fit for each channel (b) shows the RMS for each channel (c) the mean bandpass of the strip (d) the RMS divided by the mean bandpass multiplied by a factor of 100 (e) the continuum baseline contribution after removal of point sources and (f) The continuum "strip chart" integrated along *good* channels. All data shown are for beam 4, polarization A.

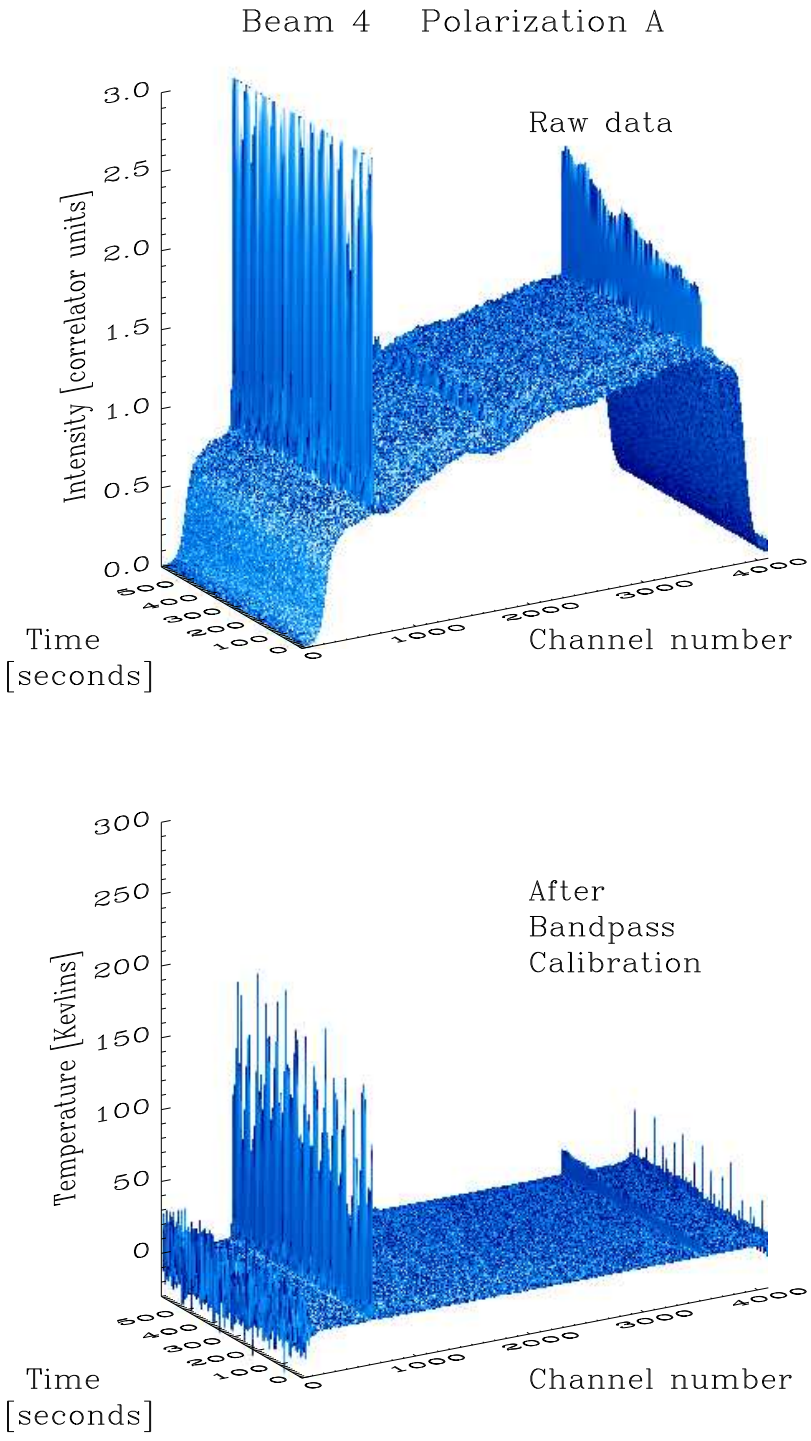

Figure 2.6: 2D surface showing a time/frequency plot of beam 4 polarization A. The upper plot shows the raw ALFALFA data, clipped to an intensity of 3.0 for dynamic range convenience. The bottom plot shows the data, scaled to Kelvins, after the bandpass calibration process. Features in both plots include the FAA radar signature near channel 615 (1350 MHz) and galactic HI near channel 3500 (1420 MHz).

bandpass is computed as

$$BP_{corr} = \frac{BP_{on} - BP_{off}}{BP_{off}} T_{sys} \tag{2.9}$$

All calibrated values are stored in units of Kelvins. Calibrated and reduced drift files are saved to disk for interference flagging. An example of before and after calibrated time/frequency plots is shown in Figure 2.6.

Careful attention is given to flagging radio frequency interference for both improvement of data quality products and to decrease the likelihood of including spurious detections in the automated signal extraction process later on. The RFI flagging stage is where data quality is first assessed. Each bandpass calibrated 2D time/frequency plot is examined closely by eye. Areas of interference due to nearby airport radar and associated harmonics are individually flagged; these records and/or channels are excluded during the signal extraction and data cube gridding process. An example flagging session is shown in Figure 2.7. The data products as this stage in the pipeline are known as Level I data products.

2.4.2 Level II Data and Data Cubes

The ALFALFA primary target areas consist of the "Spring" sky between 7^h30^m < R.A. < 16^h30^m and the "Fall" sky between 22^h < R.A. < 03^h. ALFALFA "grids" are 3D position-position-velocity data cubes from which final source measurements are obtained. The process of creating grids begins by scanning coordinate information saved in small size (~30MB) position files for each observing session. A listing is compiled of any drift files that will contribute to any position within the specified grid boundaries. Each drift file is opened and data contributing to the grid are summed in the appropriate x/y/frequency bins weighted by a Gaussian kernel (typically of size 2′). Grid pixels are

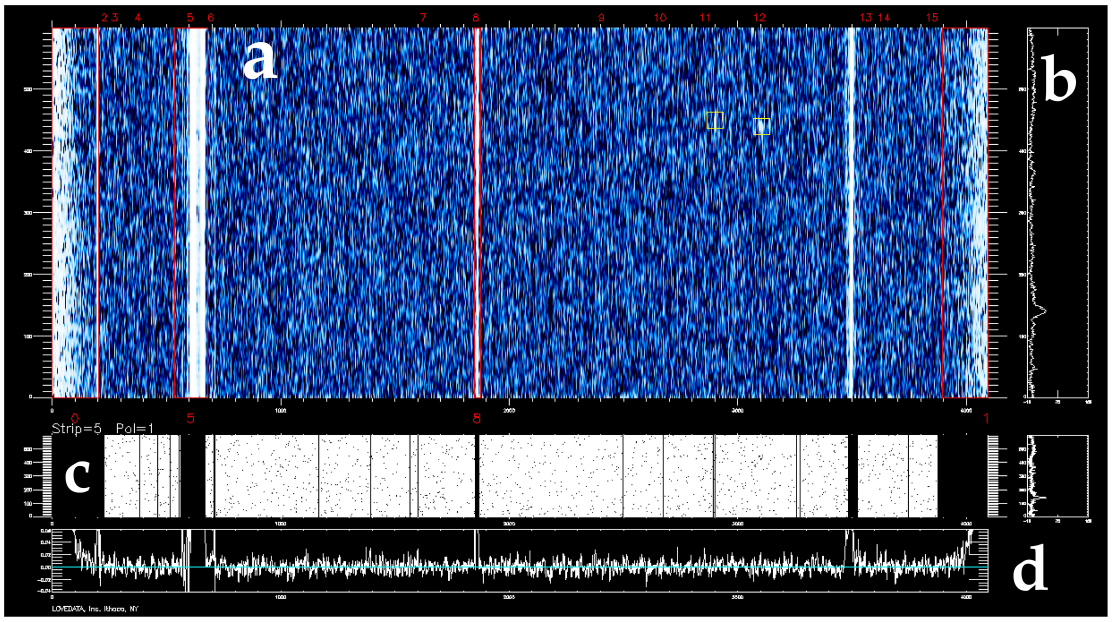

Figure 2.7: Example session of radio-interference flagging from April 4, 2005. The user selects regions of interference via predetermined box numbers or user-defined regions. Cross-referencing with optical and HI databases allows the user to check known information during the data reduction session. The figure sections are as follows: a) the main time vs. frequency plot of the data showing the FAA radar and galactic HI, b) the continuum flux integrated along the strip, c) the map mask showing the pixels (in white) used by the bandpass calibration procedure to produce the continuum flux strip, and d) the average spectrum for all 600 records. Red boxes indicated marked regions of RFI, and yellow boxes indicate previously identified objects in the Arecibo General Catalog.

approximately $1'$ square depending on the declination range. Data are also included or ignored based on RFI flagging from the level I production process. A spectral weight map for each channel is also created based on contributing drifts at each grid point. The entire process is repeated for total power continuum maps and weights. Final grids are scaled to units of Jansky beam^{-1} and divided by the appropriate weights for both spectral and continuum maps. In addition, because the synthesized beam area used to generate the grids is larger than that of the telescope at *L*-band (from $3.5'$ to $4'$), the grids are also multiplied by a gain dilution factor given by

$$G_{dilute} = 1 + \frac{W_{FWHM}^2}{3'.3 \times 3'.8} \tag{2.10}$$

where W_{FWHM} is the Gaussian kernel size of $2'$.

Velocity channels are first shifted to the heliocentric velocity frame such that channel 2047 (counting from zero) of all raw spectra are at a frequency of 1385 MHz and $cz_{\odot}$ = 7663 km s^{-1}. The process creates four data cubes. Each contains a spectral HI cube of size 144 × 144 pixels in R.A. and declination, and 1024 channels in frequency space (∼5100 km s^{-1} in *cz* space). The four data cubes are identified by a letter designation for the $cz_{\odot}$ range that they cover: (a) -2000 to 3300 km s^{-1}, (b) 2500 to 7900 km s^{-1}, (c) 7200 to 12800 km s^{-1}, and (d) 1200 to 17900 km s^{-1}. Each grid overlaps the next by ∼1000 km s^{-1} in *cz* space. Each of the four grids occupies approximately 330 MB of disk space, with ancillary files attached containing a complete history of how the grid was constructed.

Baselining involves processing grid slices - R.A. vs. spectral channel maps are baselined for both polarizations. For most maps, a first order polynomial is fit and subtracted in the spectral direction. Special cases may require excluding galactic HI, high-velocity clouds, and high signal-to-noise extended detections from the fit. In areas where residual stray RFI may be present, baselining is also performed in the R.A. direction. A secondary process involves fitting robust n =1 polynomial fits to R.A./decl. maps for each spectral channel. The subtraction along each R.A. strip effectively “flatfields” the image in channels devoid of any signals. Extended signals are excluded from the fit, especially for channels containing galactic HI or bright galaxy emission. The grids used for the data set from which this dissertation is derived are shown in Figure 2.8. An automated matched filter algorithm is used for signal extraction. Candidate signals are later examined by eye and cross correlated with existing catalogs. The process is fully described by Saintonge (2007a,b). The data products at this stage are referred to as Level II.

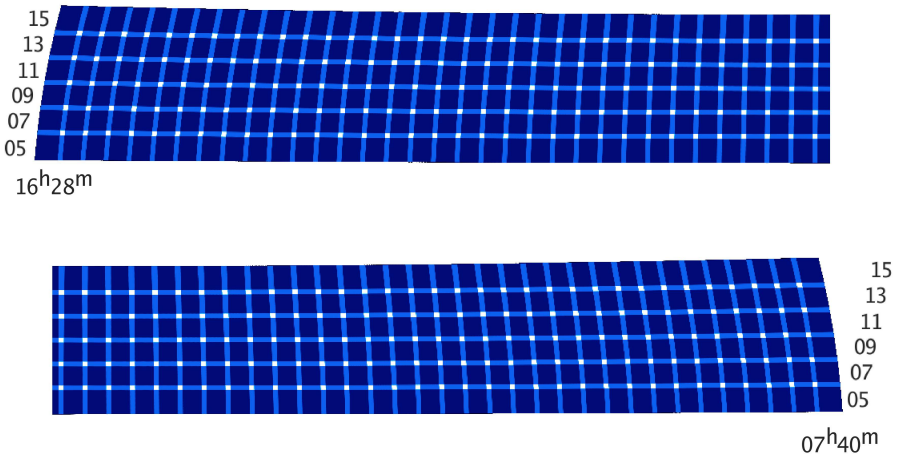

Figure 2.8: Layout of all 402 grids comprising the Spring ALFALFA sky coverage as of June 2008. The overlap and 2.4° × 2.4° sky area of each grid is shown in an Aitoff equal area projection. The numbers at left and right indicate the grid center declination identifications. The right ascension assignments extend from 0740 to 1628. The grids cover 1527 square degrees and represent 21.8% of the ALFALFA survey.

2.4.3 Spectra and Cataloging

Fully processed grids and candidate catalogs are analyzed in a visualization environment called GRID*View*. The program is shown in Appendix A in the context of the Virtual Observatory environment. In the vicinity of candidate detections, both polarizations, existing catalog entries and redshifts, and imaging databases are examined closely to corroborate the signal if possible. A thumbnail data cube is then extracted from a subgrid covering at least $7' \times 7'$ and imported into a measurement environment called GAL*Flux*. The measurement process begins with the selection of channels containing source emission by eye. A zeroth moment map is created by integrating the flux over these channels with pixel values given by

$$M_0 = \int S_\nu dv \ \ [\mathrm{mJy\ beam^{-1}\ km\ s^{-1}}] \tag{2.11}$$

An ellipse is fit at multiple isophotal levels. The isophotal half-peak intensity level for the moment map is used for all cataloged measurements. The source image is spatially integrated over the solid angle covered by the pixels within the fit. This summed flux density s_ν is divided by the sum of the beam values B sampled at the position of the image pixels, given by

$$S_\nu = \frac{\sum_{x_0} \sum_{y_0} s_\nu(\Delta x, \Delta y)}{\sum_{x_0} \sum_{y_0} B(\Delta x, \Delta y)} \text{ [mJy]} \tag{2.12}$$

as described by Shostak & Allen (1980). This flux density measurement technique is optimized for source sizes near the beam area or smaller.

For a given integrated spectral profile, peak flux density levels f_p of each spectral horn are selected. Channels are identified along the profile sides between 15% and 85% of f_p-RMS. Velocities are identified for each side of the profile where a polynomial fit to the identified channels gives a value of 50% of f_p-RMS. The difference in these values is the velocity width W_{F50}, and the average is systemic velocity V_{50}. The measurement is also made at the 20% level for the velocity and associated width. Velocity width measurements also play an important part in determining the signal–to–noise ratio (S/N) of a spectrum, especially for sources with $W_{F50} > 400$ km s^{-1}. This important feature will be discussed in Chapter 3.

Velocities and widths, centroided sky positions from the isophotal ellipse fits, S/N, etc., are all measured and stored in individual source files with the spectral profiles. Optical identification is also made based on previous HI observations (Springob et al. 2005b) and visual inspection of the optical imaging databases from Sloan and the Digital Sky Survey.

CHAPTER 3

CATALOG AND STATISTICS

3.1 Data Access

Because the ALFALFA collaboration includes many worldwide members, rapid dissemination of the data products is of the utmost importance to the survey's success[1]. The catalog results presented here are accessible from the ALFALFA archive (designed by the author) at *http://arecibo.tc.cornell.edu/hiarchive/alfalfa/*. The site provides Web services using protocols from the U.S. National Virtual Observatory[2]. Contributions to the Virtual Observatory are described in Appendix A. The measurements and spectra join the fast-growing archive of HI measurements (Springob et al. 2005b; Giovanelli et al. 2007; Saintonge et al. 2008; Kent et al. 2008). An ongoing development effort focuses on the long-term public delivery of the 3D ALFALFA data set through Web–based access tools. A major challenge is the data volume: after regridding the 3D cubes covering the 32 individual "grids" from the current catalog alone occupy a total disk space of 50 GB (a minor fraction of the total survey data set). Allowing access and manipulation of the gridded data publicly will require the development of Web services and server applications.

In this work, we present a catalog of HI sources extracted from the ALFALFA grids covering a region stretching from from +4° to 16° in declination and from 11^h36^m to 14^h00^m in R.A. For reference to our database, denomination of the grids from which sources in this catalog were extracted are 1140 to 1400 in 8^m steps of R.A.and +05 to

[1]Elements of this chapter appear in Kent et al. (2008). Reproduced by permission of the AAS.

[2]This research has made use of data obtained from or software provided by the US National Virtual Observatory(NVO), which is sponsored by the National Science Foundation.

+15, in steps of 2°. The solid angle of sky can be computed via

$$\text{Area} = \Delta\phi \, \frac{\pi}{180} \left| \cos(90^\circ - \delta_1) - \cos(90^\circ - \delta_2) \right| \text{ [steradians]} \tag{3.1}$$

where $\Delta\phi = (\mathrm{RA}_1^h - \mathrm{RA}_2^h) \times 15$ degrees hour^{-1}. This result can be converted to square degrees by multiplying by the factor $(180/\pi)^2$. The solid angle subtended by this region is ∼425 deg^2, which is ∼ 6% of the sky to be ultimately surveyed by ALFALFA. The coverage of the region is completed by the target goals of ALFALFA, i.e. the region has been sampled by two separate passes with the ALFA array in drift mode.

3.2 The Catalog

Raw data scans are processed to Level I (see Chapter 2 and Giovanelli et al. 2005b, for details) data sets upon completion of the observing sessions. The survey employs a two–pass system to yield a data set that is well sampled spatially. Once the survey has completed two passes of a designated tile it is converted into regularly gridded data cubes. Baselining, signal extraction, and source identification are completed and measurements are taken from integrated spectral profiles. These profiles originate from cutouts of the sub-grids, which are then used to create properly weighted source spectra.

Signal extraction is initiated in the Fourier domain with a automated matched filter algorithm (Saintonge 2007b). Follow-up by eye confirms these sources and matches them with any possible optical counterpart found in the Sloan Digital Sky Survey (SDSS) or blue band imaging provided by the Digital Sky Survey. In addition, measurements and sources can be compared to NED and listings of existing HI observations. This facilitates quick response for follow-up with selected sources. Candidate detections are assigned to the following classes:

1. Signals that are extragalactic HI sources above a soft limit of a signal-to-noise ratio (S/N) $\gtrsim$ 6.5.
2. Signals that are likely galactic or perigalactic in nature– high-velocity clouds.
3. Signals of lower S/N (4.5 $\lesssim$ S/N $\lesssim$ 6.5) but with corroborating evidence based on identification of an optical counterpart with similar redshift measurements at another wavelength.

Other low-S/N candidates are placed in a separate listing for future follow-up. Examples of HI spectra and DSS2 Blue band optical images of the field are shown in Figure 3.1

Table 3.1 presents the results of the 2345 detections from the portion of the survey described in this dissertation. The column descriptions are as follows:

1. The sequential catalog number (1 for Giovanelli et al. (2007) and 3 for Kent et al. (2008) and source number).
2. The Arecibo General Catalog number that corresponds to a private database entry maintained at Cornell University.
3. The Right Ascension and Declination (epoch J2000) of the centroid position. The listed position has been corrected for systemic pointing errors. An analysis of the positional accuracy will be discussed later.
4. The Right Ascension and Declination (epoch J2000) position of the most likely optical counterpart of the HI detection. Each candidate source position in an optical image is examined by eye during the data reduction process described in Chapter 2. SDSS images from the CAS server are the principle inspection tool. In the event that SDSS images do not cover the area in question, images from the blue plates of the Second Digital Sky Survey scanning are used (DSS2B; Lasker

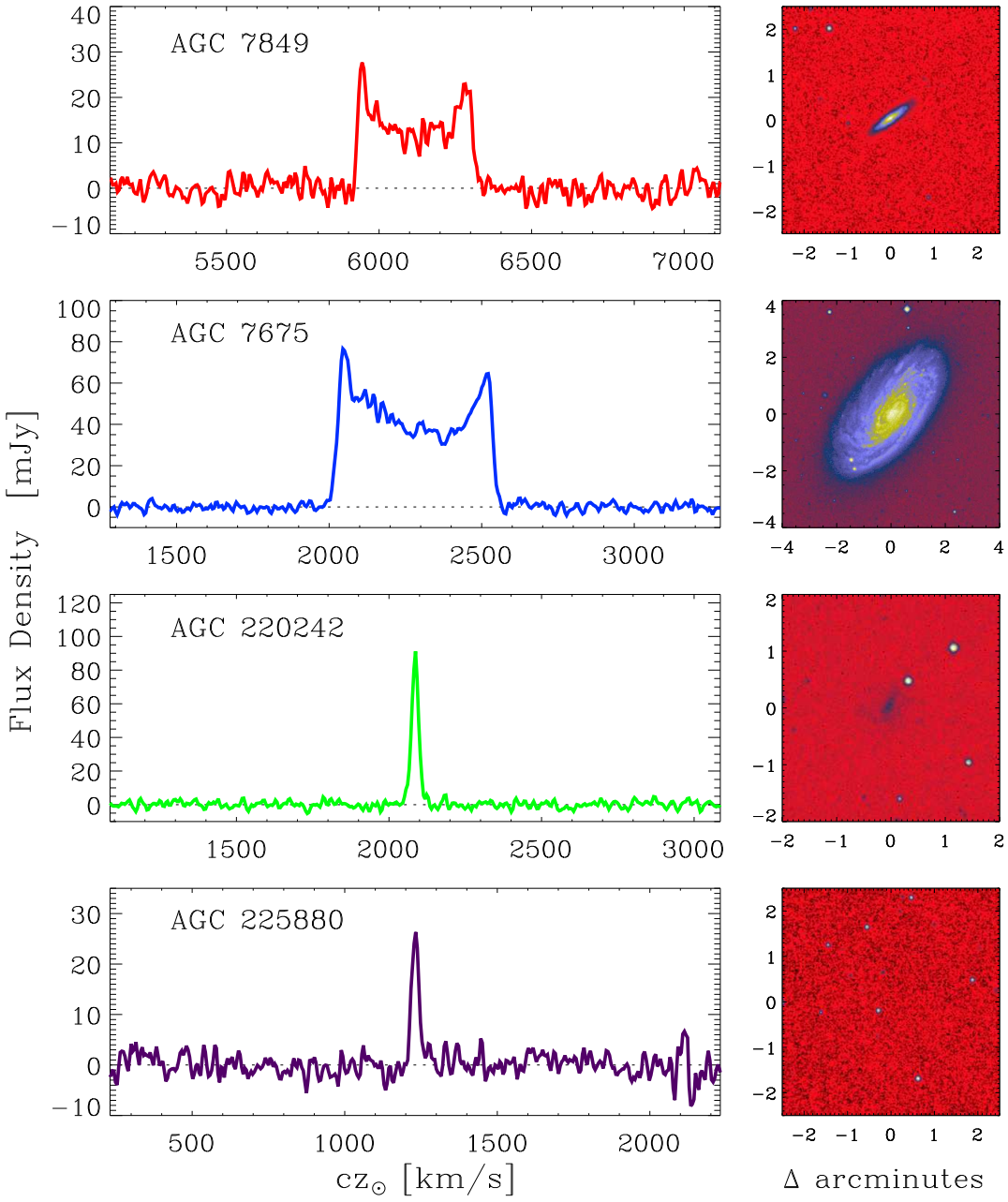

Figure 3.1: Example HI spectra of various sources. Images are obtained from the Digital Sky Survey 2 Blue plates.

et al. 1990). Optical images are examined for counterparts based on spatial proximity, morphology, color, and redshift. The centroid accuracy is $\lesssim 2''$. If no optical counterpart can be clearly identified, no optical position is recorded in the catalog – high-velocity cloud detections are included in this category. Comments are provided in Column 12 if a preferable source is identified and other possible candidates are present in the field.

5. The heliocentric velocity of the HI source in km s^{-1}, $cz_{\odot}$, measured as the midpoint between the channels at which the flux density drops to 50% of each of the two peaks (or of one, if only one is present) at each side of the spectral feature. The measurement process is described in Chapter 2. The error on $cz_{\odot}$ to be adopted is half of the velocity width (Column 6).

6. The velocity width of the source line profile, W_{F50}, measured at the 50% level of each of the two peaks, as described for Column 5. This value is corrected for instrumental broadening. No corrections due to turbulent motions, disk inclination or cosmological effects are applied. Shown in parentheses is the estimated error on the velocity width, ϵ_w, in km s^{-1}. This error is the sum in quadrature of two components: the first is a statistical error, principally dependent on the S/N ratio of the feature measured; the second is a systematic error associated with the subjective guess with which the observer estimates the spectral boundaries of the feature: maximum and minimum guesses of the spectral extent of the feature are flagged and the ratio of those values is used to estimate systematic errors on the width, the velocity and the flux integral. In the majority of cases, the systematic error is significantly smaller than the statistical error; thus the former is ignored.

7. Integrated flux density of the source, F_c, in Jy km s^{-1}. This is measured on the integrated spectrum, obtained by spatially integrating the source image over a solid angle of at least $7' \times 7'$ and dividing by the sum of the survey beam values over

the same set of image pixels (Shostak & Allen 1980). Estimates of integrated fluxes for very extended sources with significant angular asymmetries can be incorrectly estimated by our algorithm, which is optimized for measuring sources comparable to or smaller than the survey beam. A special catalog with parameters of extended sources will be produced after completion of the survey. Shown in parentheses is the estimated uncertainty of the integrated flux density, in Jy km s^{-1}. Uncertainties associated with the quality of the baseline fitting are not included; an analysis of that contribution to the error will be presented elsewhere for the full survey. See the description of Column 6 for the contribution of a possible systematic measurement error.

8. Signal–to–noise ratio (S/N) of the detection, estimated as

$$S/N = \Big(\frac{1000F_c}{W_{F50}}\Big)\frac{w_{smo}^{1/2}}{\sigma_{rms}} \tag{3.2}$$

where F_c is the integrated flux density in Jy km s^{-1}, as listed in Column 7, the ratio $1000F_c/W_{F50}$ is the mean flux across the feature in mJy, w_{smo} is either $W_{F50}/(2 \times 10)$ for $W_{F50} < 400$ km s^{-1}or $400/(2 \times 10) = 20$ for $W_{F50} \geq 400$ km s^{-1}[w_{smo} is a smoothing width expressed as the number of spectral resolution bins of 10 km s^{-1} bridging half of the signal width], and σ_{rms} is the rms noise figure across the spectrum measured in mJy at 10 km s^{-1}resolution, as tabulated in Column 9. In a similar analysis, from Giovanelli et al. (2005a) we adopted a maximum smoothing width $W_{F50}/20 = 10$. See Figure 3.4 and related text below for details. The value of the smoothing width could be interpreted as an indication of the degree to which spectral smoothing aids in the visual detection of broad signals, against broad-band spectral instabilities. The ALFALFA data quality appears to warrant a more optimistic adoption of the smoothing width than previously anticipated.

9. Noise figure of the spatially integrated spectral profile, σ_{rms}, in mJy. The noise

figure as tabulated is the rms as measured over the signal– and radio-frequency interference (RFI)-free portions of the spectrum, after Hanning smoothing to a spectral resolution of 10 km s^{-1}.

10. Adopted distance in Mpc, D_{Mpc}. For objects with $cz_{cmb} > 3000$ km s^{-1}, the distance is simply $cz_{cmb}/H_\circ$; cz_{cmb} is the recessional velocity measured in the Cosmic Microwave Background reference frame and $H_\circ$ is the Hubble constant, for which we use a value of 72 km s^{-1} Mpc^{-1}. For objects of lower cz_{cmb}, we use a peculiar velocity model for the local universe. This model is based on the work of Tonry et al. (2000) and Masters et al. (2004). Objects that are thought to be parts of clusters or groups are assigned the cz_{cmb} of the cluster or group. Cluster and group membership are assigned following the method described in Springob et al. (2007). Note that the Virgo cluster extends over much of the solid angle surveyed. This introduces unavoidable ambiguities in the distance assignment, as the peculiar flow model only corrects for large-scale perturbations in the velocity field and is unable to deal effectively with regions in the immediate vicinity of the cluster and along a section of a cone which contains the cluster, up to $cz_\odot \sim 2500$ km s^{-1}. For objects assigned to the Virgo cluster, a distance $D_{Virgo} = 16.7$ Mpc is used (Mei et al. 2007).

11. Logarithm in base 10 of the HI mass, in solar units. That parameter is obtained by using the expression $M_{HI} = 2.356 \times 10^5 D^2_{Mpc} F_c$.

12. Object code, defined as follows:

    Code 1 refers to sources of S/N and general qualities that make it a reliable detection. By "general qualities" we mean that, in addition to an approximate S/N threshold of 6.5, the signal should exhibit a good match between the two independent polarizations and a spatial extent consistent with expectations given the telescope beam characteristics. Thus, some candidate detections with $S/N > 6.5$

have been excluded on grounds of polarization mismatch, spectral vicinity to RFI features or peculiar spatial properties. Likewise, some features of $S/N < 6.5$ are included as reliable detections, due to optimal overall characteristics of the feature. The S/N threshold for the acceptance of a reliable detection candidate is thus soft. In a preliminary fashion, we estimate that detection candidates with $S/N > 6.5$ in Table 1 are reliable, i.e., they will be confirmed in follow-up observations in better than 95% of cases (Saintonge 2007b).

Code 2 refers to sources of low-S/N (< 6.5), which would ordinarily not be considered reliable detections by the criteria set for code 1. However, those HI candidate sources are matched with optical counterparts with known optical redshifts which match those measured in the HI line. These candidate sources, albeit "detected" by our signal finding algorithm, are accepted as likely counterparts only because of the existence of previously available, corroborating optical spectroscopy. We refer to these sources as "priors". We include them in our catalog because they are very likely to be real.

Code 9 refers to objects assumed to be HVCs; no estimate of their distances is made.

A notes flag is also included. An asterisk at the end of the row indicating a comment is included for this source in the online database or publication.

3.3 Statistics of the Catalog

For this region 2345 detections are presented: 1818 (~77.5%) are code "1" detections that rate fair to excellent in quality; 473 (20.2%) are code "2" detections that have known priors associated with them–optical redshifts corroborate these lower-S/N detections;

Table 3.1: HI Candidate Detections

Cat#-ID	AGC	HI Coords.	Opt. Coords.	$cz_\odot$	$w50$ (ϵ_w)	F_c (ϵ_f)	S/N	RMS	Dist.	$\log_{10} M_{HI}$	Code
-	-	(J2000)	(J2000)	km s^{-1}	km s^{-1}	Jy km s^{-1}	-	mJy	Mpc	$M_\odot$	-
(1)	(2)	(3)	(4)	(5)	(6)	(7)	(8)	(9)	(10)	(11)	(12)
3- 1	210497	113610.7+100304	113609.9+100319	6210	261 (23)	2.58 (0.10)	17.1	2.09	88.2	9.67	1
3- 2	213318	113610.9+114858	113612.2+114857	9518	229 (13)	0.68 (0.06)	6.2	1.61	133.7	9.46	2
3- 3	210517	113653.6+115040	113655.3+115053	10347	297 (5)	1.16 (0.07)	9.3	1.62	145.2	9.76	1
3- 4	213320	113713.2+114840	113714.3+114806	10714	122 (8)	1.30 (0.05)	17.6	1.49	150.3	9.84	1
3- 5	213100	113739.2+085134	113739.2+085151	3815	118 (36)	0.50 (0.06)	5.4	1.91	55.4	8.56	2
3- 6	210540	113805.9+111243	113808.1+111149	10660	316 (15)	1.76 (0.10)	10.5	2.11	149.5	9.96	1
3- 7	6605	113813.3+120646	113813.0+120643	982	89 (6)	3.20 (0.07)	35.7	2.11	11.6	8.00	1
3- 8	215419	113830.7+111357	113832.2+111316	13062	53 (14)	0.63 (0.06)	8.1	2.37	182.8	9.70	1
3- 9	210550	113844.5+105327	113846.1+105258	12788	301 (36)	1.21 (0.12)	5.7	2.73	179.0	9.96	2
3- 10	213025	113905.0+100815	113905.4+100807	12721	118 (5)	1.14 (0.07)	11.0	2.11	178.1	9.93	1
3- 11	213102	113911.8+093815	113911.6+093808	5963	137 (15)	0.93 (0.07)	9.0	1.96	84.8	9.20	1
3- 12	213103	113924.3+084254	113926.3+084222	5460	180 (6)	0.76 (0.07)	6.1	2.10	77.9	9.04	2
3- 13	6626	113952.1+085214	113952.8+085229	1984	156 (10)	4.87 (0.07)	43.1	2.02	29.6	9.00	1
3- 14	210582	114000.7+112745	114001.5+112746	10267	360 (4)	2.86 (0.10)	15.6	2.16	144.1	10.15	1
3- 15	6633	114018.8+090033	114018.5+090035	1810	294 (24)	4.12 (0.10)	23.4	2.29	29.6	8.93	1

the remaining 54 detections (2.3%) are high-velocity clouds.

Of the detections presented in this catalog, 24% have $cz_{\odot} < 3000$ km s^{-1}, a large fraction explained by the fact that this portion of the survey crosses the Virgo region and supergalactic plane where the density of galaxies is higher. The detection rate is 5.5 objects per square degree. Excluding the HVC detections, 52 do not have apparent optical counterparts. A preliminary discussion of these "optically unseen" HI clouds was reported by Kent et al. (2007). Of particular interest is a cloud complex of five detections located halfway between M87 and M49. If not gravitationally bound, the system will disperse in less than a cluster crossing time. The detections and aperture synthesis follow-up are described in Chapters 4 and 5.

The described catalog, when combined with a catalog of strips to the north presented by Giovanelli et al. (2007) presents a wealth of information to complement existing and future Virgo Cluster surveys across the spectrum. ALFALFA improves upon previous HI surveys in numbers and positional accuracy of the first generation HI survey HIPASS. Wong et al. (2006) reported on 131 detections from the HIPASS survey in the same ALFALFA region for this work's catalog. ALFALFA also complements the *GOLDMINE* database (Gavazzi et al. 2003), an optically selected compilation of Virgo galaxies. Long integrations were used on some of the *GOLDMINE* detections; as a result some are fainter than the ALFALFA detection limit.

The region of sky presented with this catalog lies south of M87 and is shown in Figure 3.2. The upper panel displays all detections, while the lower panel shows detections found at $cz_{\odot} < 3000$ km s^{-1}. Various distributions of the catalog parameters are shown in Figure 3.3: (a) shows large-scale structures of Virgo and the A1367-Coma supercluster regime in a velocity distribution, as well as the high cz gap near 15,000 km s^{-1} resulting from RFI; panels (b), (c), and (d) show the distributions for the velocity width W_{50}, the

integrated flux and S/N, respectively. The final panel (e) shows the HI mass distribution, with distances computed from velocity flow models (Tonry et al. 2000; Masters et al. 2004). The uncertainty in the distance of galaxies projected on a narrow cone centered on the Virgo Cluster causes detections to have uncertain calculated HI masses. Other distance indicator techniques will need to be employed in order to properly determine an accurate HI mass function. This topic will be discussed in future work.

The top panel of Figure 3.4 shows the Spänhauer diagram, detailing the HI mass versus distance for the objects in the catalog. The placement of nearby objects at the Virgo distance by the velocity flow model is clearly seen as the vertical gathering of objects at 16.7 Mpc. Regions affected by RFI are also indicated with vertical dashed lines. The middle panel of Figure 3.4 shows the S/N ratio versus measured velocity width of the catalog entries, demonstrating the independence of signal extraction on velocity widths. The bottom panel of Figure 3.4 shows the integrated flux versus the measured velocity width. The dashed line indicates an S/N limit of 6.5, the rough limit of code 1 objects listed in Table 3.1.

3.4 Positional Accuracy of Cataloged Sources

Continuum sources are extracted and their positions are measured in a "telescope" coordinate reference frame. This reference frame is determined at the Observatory separately for each receiver system by optimizing a model fit to a set of pointing calibrators. Repeatable residuals from this model translate into small-scale pointing errors, which typically have amplitudes on order of 15″ for the ALFA array receivers. These errors vary with both azimuth and zenith angles. Because ALFALFA observations are made with ALFALFA at the meridian (constant azimuth), and consist of long runs at a constant

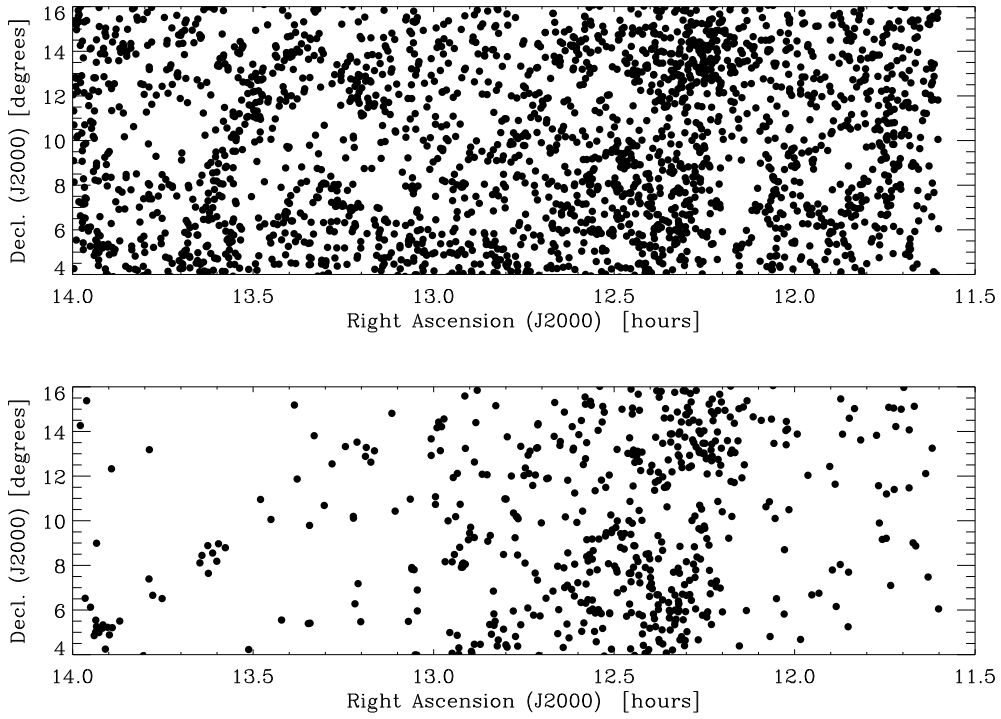

Figure 3.2: Spatial distribution of HI candidate detections listed in Table 3.1, with analysis completed by B. R. Kent, R. Giovanelli, M. P. Haynes, and R. A. Koopmann. The upper panel shows all detections presented in this catalog. The lower panel shows all objects with $cz_{\odot} < 3000$ km s^{-1}.

zenith angle, the ALFALFA sources' positions in the telescope reference frame easily reveal the systematic errors represented by those residuals when they are compared with the positions of a higher resolution – and thus higher accuracy – coordinate reference system. In this section we compare HI source positions obtained in the Arecibo telescope reference system with two more accurate position sets: those of optical galaxies and those of VLA radio continuum sources from the NRAO VLA Sky Survey (NVSS; Condon et al. 1998).

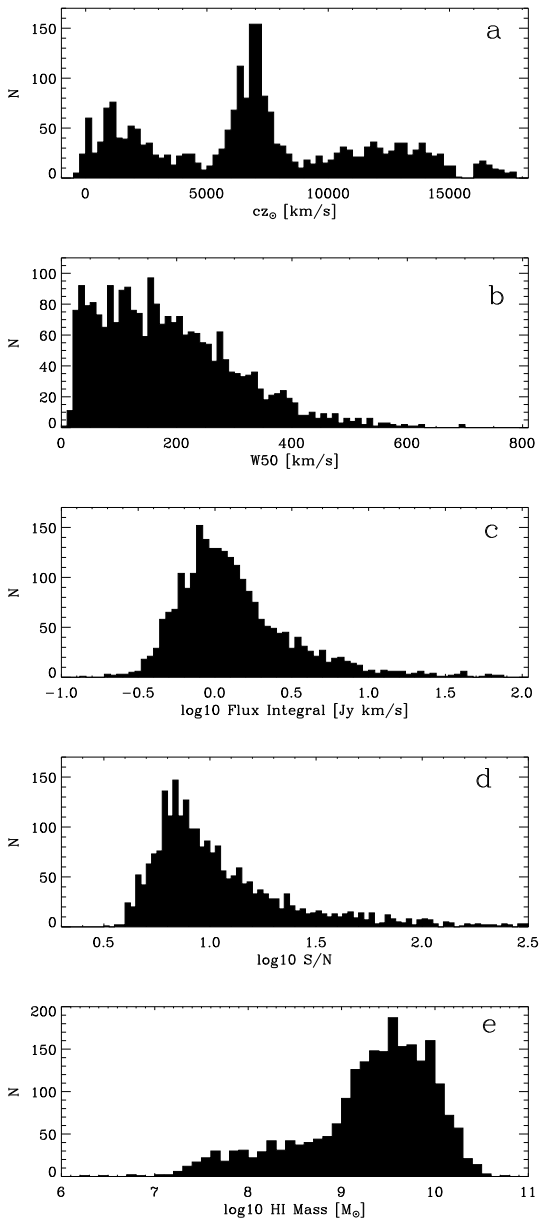

Figure 3.3: Various histograms of the HI detections listed in Table 1. (a) shows the *cz* distribution in km s^{-1}; (b) shows the HI line width W_{50} in km s^{-1}; (c) shows the base 10 logarithm of the integrated flux in Jy km s^{-1}; (d) shows the base 10 logarithm of the peak S/N ratio; (e) shows the derived HI mass, in base 10 logarithmic units of $M_{\odot}$. The HI masses of some detections may be skewed to higher estimates due to distance uncertainties toward the Virgo cluster region.

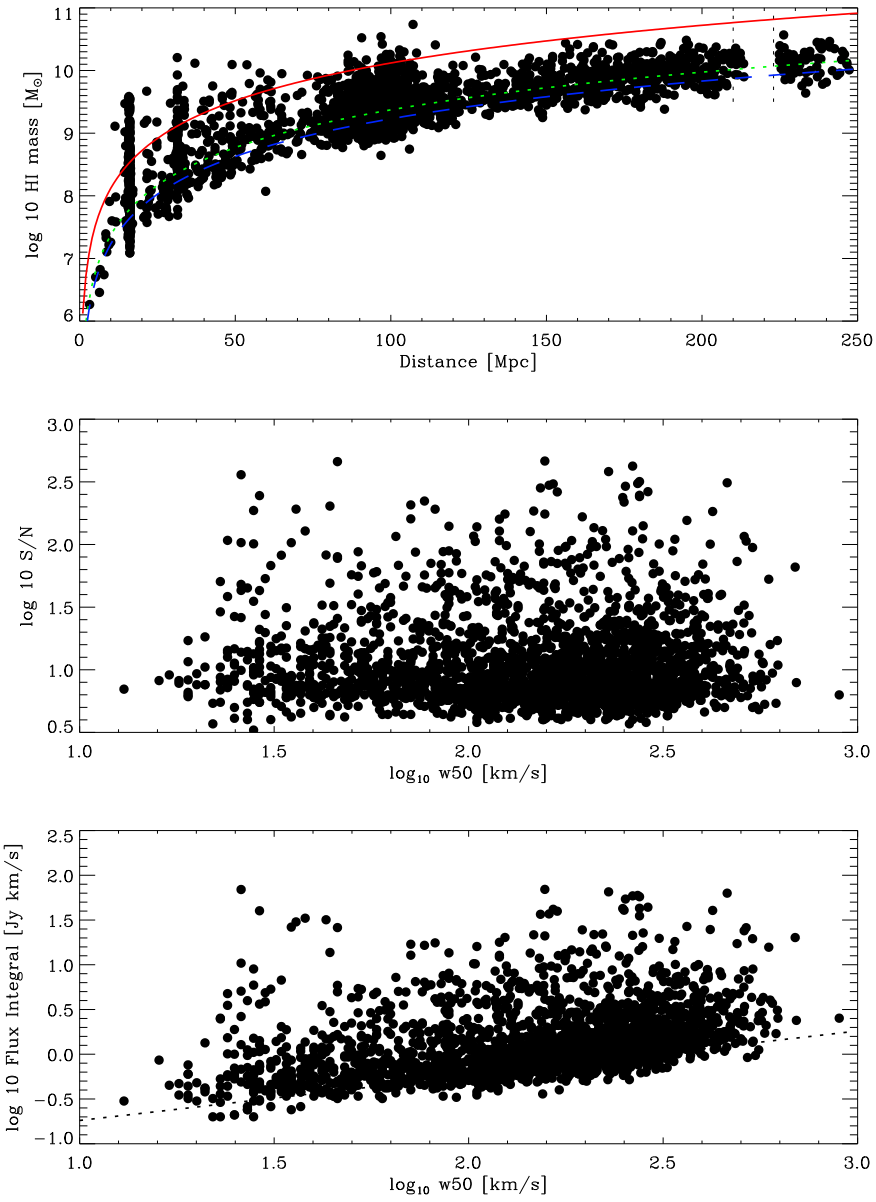

Figure 3.4: Statistical properties of the Virgo south catalog. The top panel shows the HI mass versus distance for all sources of type 1 and 2 presented in Table 3.1. Note that galaxies assigned to the Virgo cluster appear as the vertical feature at 16.7 Mpc, and the gap at 220 Mpc is due to RFI. The solid red line indicates the 5σ detection limit (5.6 Jy km s^{-1}) for the HIPASS survey. The dotted green line indicates a 1.0 Jy km s^{-1} limit. The dashed blue line indicates a 0.72 Jy km s^{-1} limit for the ALFALFA survey. All detection limits are shown assuming a velocity width of 200 km s^{-1}. The middle panel shows the $\log_{10}$ S/N ratio versus velocity width W_{50}. The lower envelope is independent of S/N which indicates that no significant bias is present in the detection of sources of large width. The bottom panel shows the integrated flux versus velocity width W_{50}, with the dashed line indicating a S/N limit of 6.5.

3.4.1 Positional Differences between HI and Optical Sources

The accuracy of positional HI centroids is important in establishing correct optical identifications. The ALFALFA catalogs are presented to the astronomical community with positions as accurate as possible. The impact of the telescope pointing is recovered as we describe below.

The $3'.3 \times 3'.8$ FWHM elliptical beam of the Arecibo telescope affords the ALFALFA survey greater positional accuracy than previous large-scale blind HI surveys. This factor in the survey characteristics becomes important when matching HI detections with their optical counterparts, if they exist. Positional accuracy is limited by the beam size, S/N, and errors in the telescope's pointing. For the region of sky surveyed in this work, the ALFA receiver system is oriented such that the beam's major axis is in the declination direction and the telescope's azimuth arm is aligned in the north–south direction.

Processed ALFALFA drift scans are combined and re-gridded into a data cube that is spatially sampled at $1' \times 1'$ per pixel. Gaussian weighting is also applied and the final resolution is $3'.8 \times 4'.3$. Sources and their associated measured parameters are extracted from these data cubes. Source extraction is carried out via an automated matched filter algorithm with visual follow-up confirmation by a project team member. Once a source is identified, a 2D map is integrated over the spectral extent of the object, with ellipses fit to the quarter- and half-power levels of the measured peak, as well as other preset isophotal levels. Since most sources are unresolved by the ALFA beam, the HI source position is taken to be the center of the half-power ellipse. Extended objects that may exhibit warped or asymmetric disks are treated with extra care because the ellipse may not provide the best estimate of the position center.

The systematic pointing errors of the telescope can be recovered due to the fixed azimuth telescope observing mode employed by the survey. These errors add ∼15″ or more at *L*-band frequencies with the maximum pointing errors occurring when the telescope is at the extremes of its zenith angle range.

Positions of optical counterparts of HI sources are obtained by team members through the Digital Sky Survey, from the SDSS database, or through the local Arecibo General Catalog maintained at Cornell. Figures 3.5 and 3.6 show the positional differences (HI minus optical) for twelve different Declination ranges, each binned by 1°. The points correspond to sources that have optical counterparts – optically inert HI clouds, HVC, and tidal tails are not included. The position differences can be attributed to centroiding statistical errors, optical misidentification, and the previously mentioned telescope pointing offsets. The optical centroid errors are negligible when compared to the other source errors. The systematic error budget, as illustrated by offsets in the data distribution from the center of the plots, is attributed to telescope pointing errors.

Signal–to–noise affects the accuracy of the HI position centroid. Figure 3.7 shows the positional accuracy of the HI positions, after correction for telescope pointing errors, for various S/N regimes. For the higher S/N detections the median centroid error is approximately 15″.

3.4.2 Positional Errors as Derived from Radio Continuum Sources

In addition to spectral data cubes, ALFALFA data are used to generate regularly gridded continuum maps. Continuum sources are extracted and their positions determined. These maps are used to determine pointing corrections for the ALFALFA catalog objects by comparing centroid positions with those published by the NRAO VLA Sky Survey

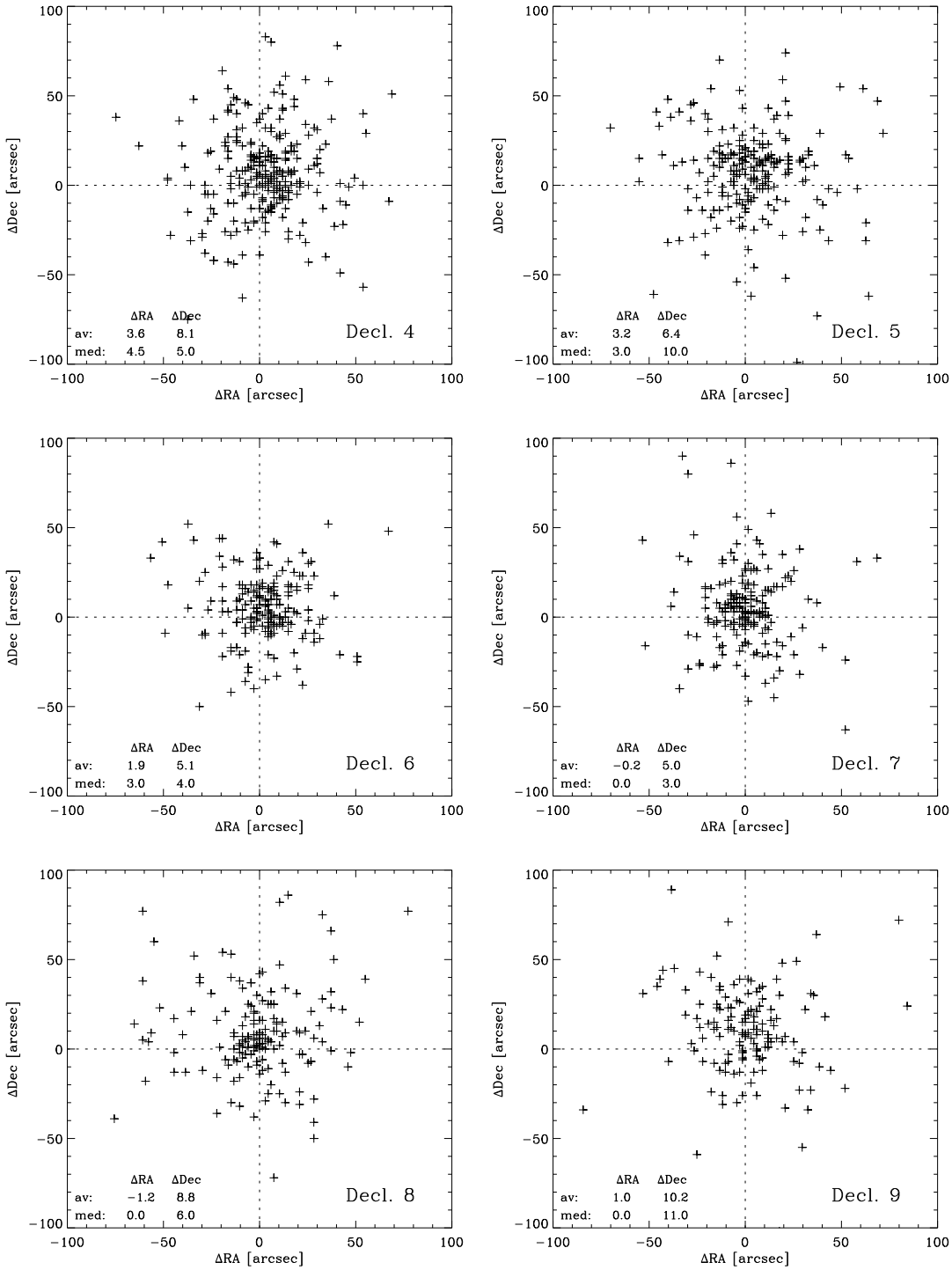

Figure 3.5: Differences between the positions of the HI sources for declination ranges 4, 5, 6, 7, 8 and 9 degrees, as indicated by the values embedded in the source names in Column 1 of Table 3.1, and the optical counterpart positions as listed in Column 4 of Table 3.1. Sources are separated by declination bins of 1°: the label "Decl. 8" identifies sources with declination between +8° and +9°, etc. Average and median offsets, expressed in arcseconds, are inset within each panel.

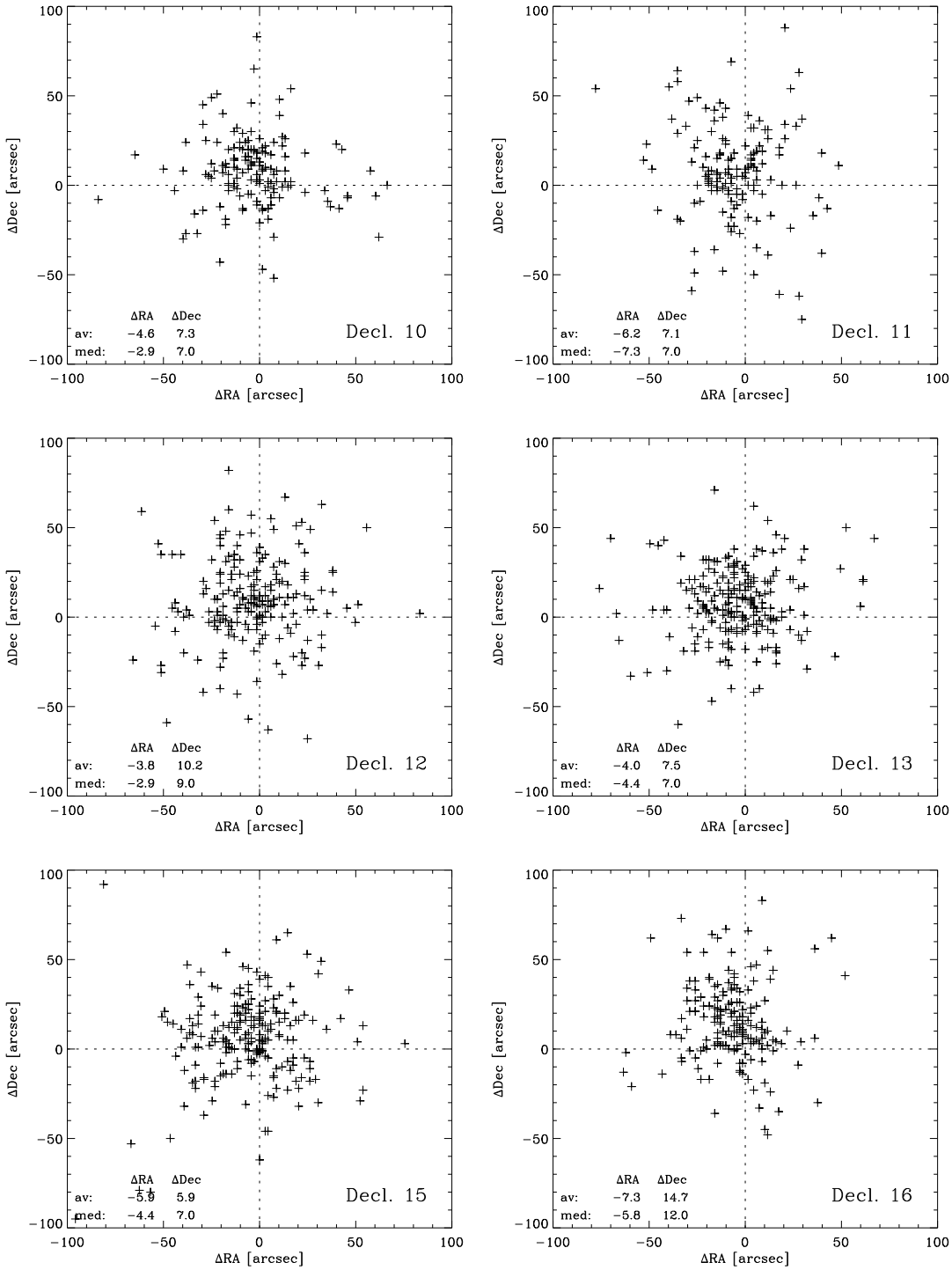

Figure 3.6: Differences between the positions of the HI sources for declination ranges 10, 11, 12, 13, 14, and 15 degrees, as indicated by the values embedded in the HI source names corresponding to the identifiers in Column 1 of Table 3.1, and the optical counterpart positions as listed in Column 4 of Table 3.1. Sources are separated by declination bins of 1°: the label "Decl. 14" identifies sources with declination between +14° and +15°, etc. Average and median offsets, expressed in arcseconds, are inset within each panel.

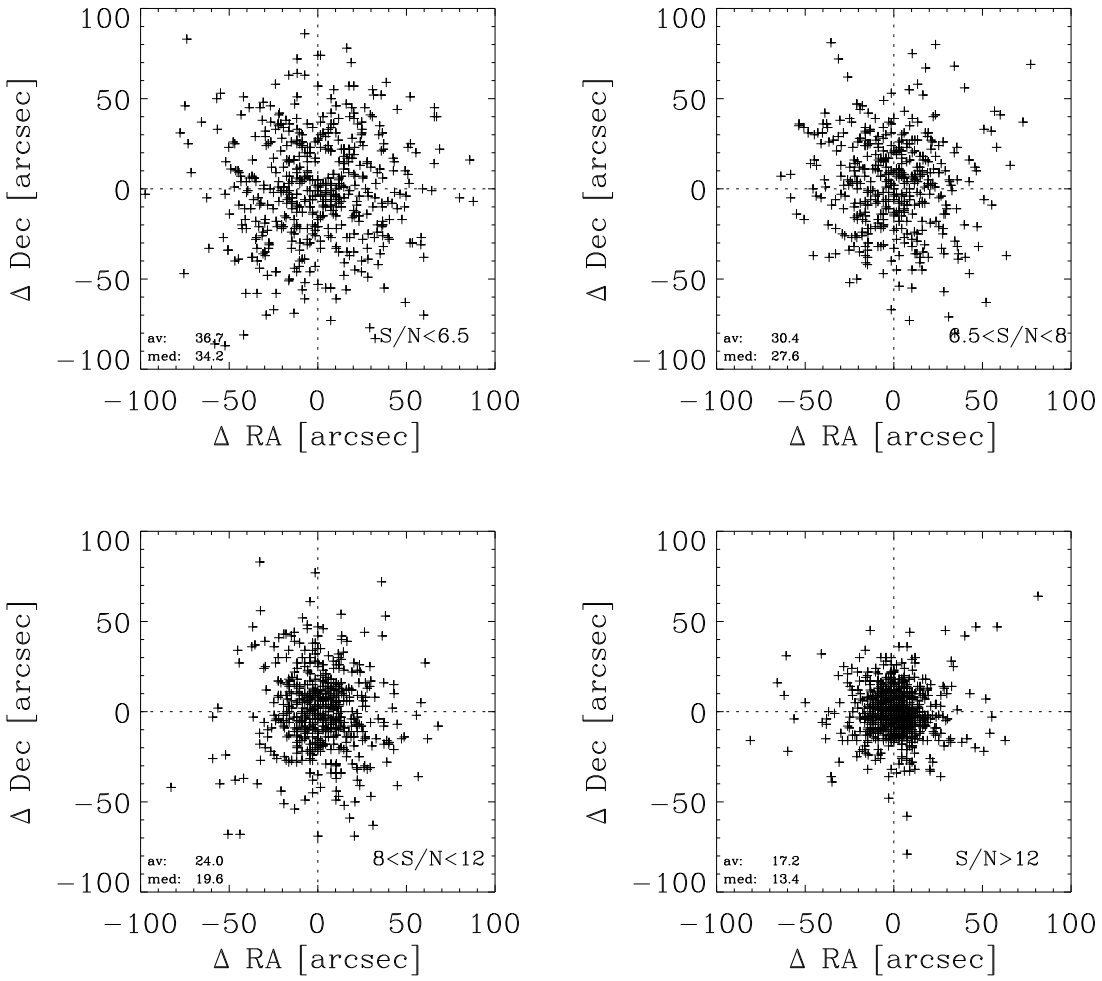

Figure 3.7: Differences between the positions of the HI sources, as indicated by the values in Column 3 of Table 3.1, which are corrected for systematic telescope pointing errors, and the optical counterpart positions as listed in Column 4 of Table 3.1. Sources are separated by S/N as indicated in each panel. Average and median offsets, expressed in arcseconds, are inset within each panel.

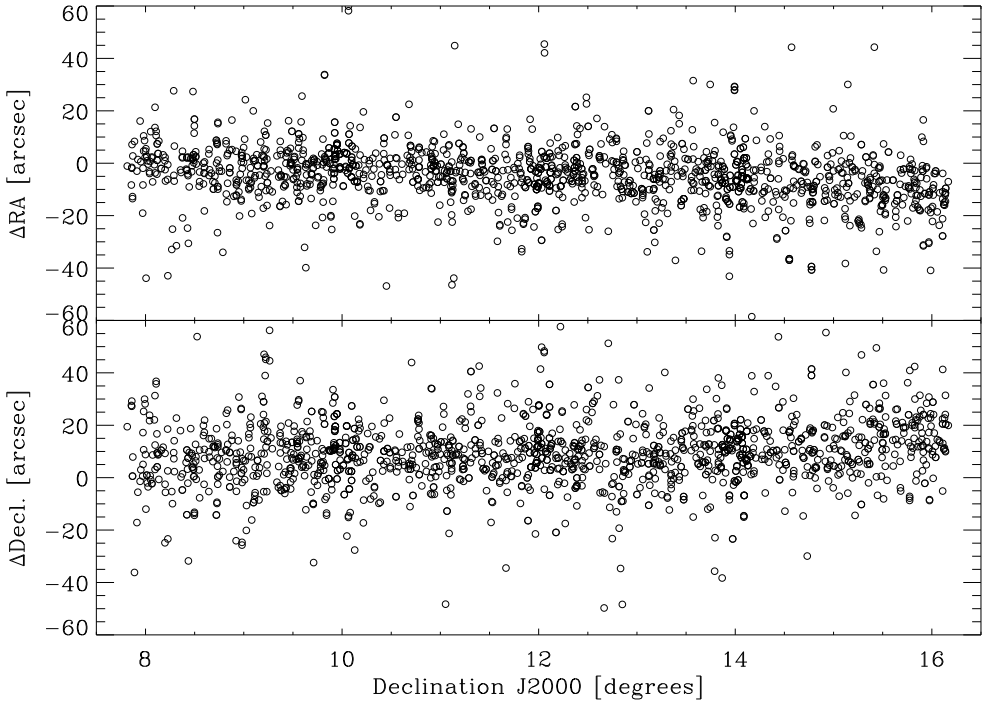

Figure 3.8: Positional differences between 1568 ALFALFA and NVSS continuum sources (Condon et al. 1998). The offsets in the mean values of ΔR.A. and ΔDecl. are due to the Arecibo telescope pointing errors.

(NVSS; Condon et al. 1998). The positions presented in this catalog and in catalogs published on the online ALFALFA data archive are corrected via the method presented here. The pointing corrections utilize data from sixty-four data cubes from the Paper III catalog and the catalog presented in the paper.

Continuum sources for position comparison are selected with a priori information from the NVSS. For identification accuracy, the positions of high signal–to–noise objects are used. Therefore, for each region of sky defined by an ALFALFA data cube, an NVSS source subset is identified with a peak intensity $I_{NVSS} > 20$ mJy beam^{-1}. The average rms of the NVSS source catalog is 0.48 mJy beam^{-1}. For each of the sources in the subset, a 9′ box is cutout for the ALFALFA data centered on the NVSS centroid position. A 2-D Gaussian fit is attempted in this window. If the fit converges, then

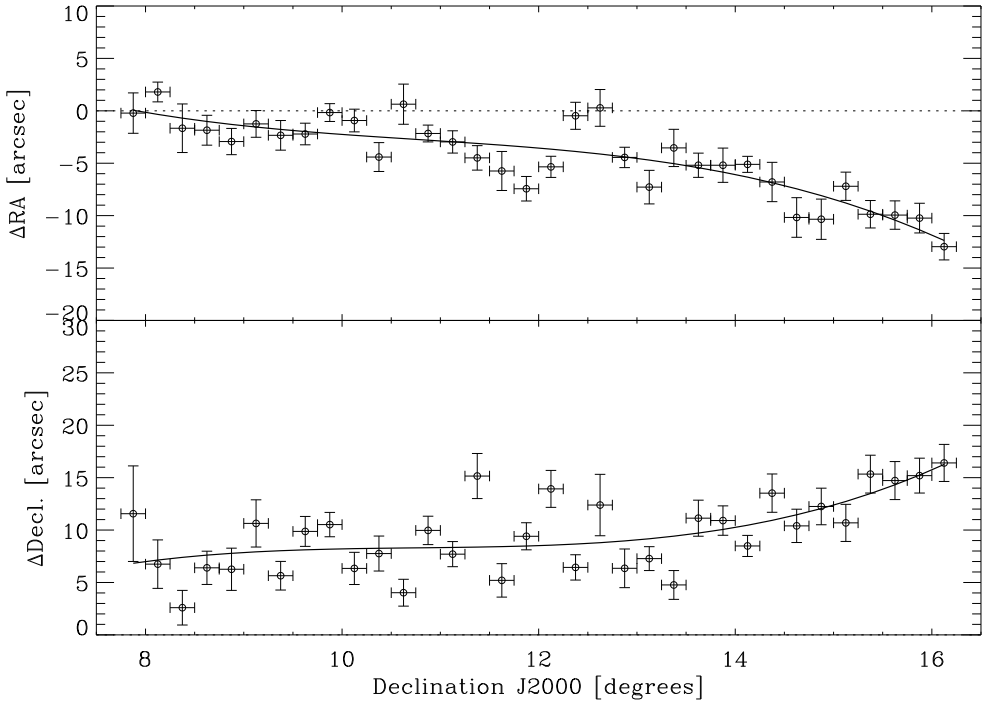

Figure 3.9: Positional difference between ALFALFA and NVSS continuum sources (Condon et al. 1998) averaged over 0.25 degree declination bins. Vertical bars indicate the error on the mean for each bin. Horizontal bars indicate the bin width for a given point.

the position from the peak of the fit is compared with any NVSS sources in the box. This process consists of comparing the ALFALFA continuum centroid with any possible NVSS positions and flux totals in the 9′ box. If the sum of the NVSS fluxes differs from the measured ALFALFA flux by more than 50%, then the source is not used in the pointing correction. Because of the differences in beam sizes, several NVSS sources may be confused and seen as one source in the ALFALFA beam. Therefore, if flux agreement is achieved between the ALFALFA and NVSS entries, acceptable sources are saved and position differences are computed in right ascension and declination.

Using this automated method for cross-identification of NVSS sources yields 1583 objects with centroid positions in the ALFALFA data cubes covering ~300 deg^2 of sky.

The differences between the ALFALFA and NVSS centroids are plotted in Figure 3.8. The robust mean position for each Declination bin is plotted in Figure 3.9, with vertical bars indicating the error on the mean and the horizontal bars indicating the bin width. These position differences are binned in quarter degree Declination increments. A third-order polynomial is fitted through these averaged points, and the resulting coefficients are used to correct the pointing in the catalog. The positions for the HI detections published in this paper reflect these pointing corrections, which remove telescope pointing errors from the HI centroids in the catalogs.

CHAPTER 4

UNIQUE DETECTIONS TOWARD THE VIRGO CLUSTER

4.1 Introduction

The predictions of the hierarchical galaxy formation paradigm requires corroboration by observational data (Cole et al. 2000; Baugh 2006). Optically selected samples of galaxies do not detect low luminosity, and hence presumably low mass objects, in the predicted numbers. This has often been referred to as the "substructure" or "missing satellite" problem (Klypin et al. 1999). The possible existence of a statistically significant population of dark matter dominated, optically faint halos would be of cosmological importance (Hawkins 1997; Somerville 2002). While the statistics of halos that are completely devoid of baryons would be difficult to assess, optically faint but gas-rich systems could be detected via their 21-cm line emission. ALFALFA, the Arecibo Legacy Fast ALFA extragalactic HI survey (Giovanelli et al. 2005b) currently underway, will cover 7000 square degrees of sky at $cz_{\odot} < 18000$ km s^{-1}. At this time more than half of the solid angle encompassing the Virgo Cluster has been fully surveyed. ALFALFA can detect $\sim 2 \times 10^7\ M_{\odot}$ at the cluster distance, which in this paper will be assumed to be 16.7 Mpc. The Virgo Cluster offers a fertile environment for the possible detection of gas-rich, optically faint systems.

A number of extragalactic HI clouds have been reported in the past (e.g., Schindler et al. 1999; Sancisi et al. 1987; Giovanelli & Haynes 1989; Chengalur et al. 1995; Kilborn et al. 2000; Ryder et al. 2001; Minchin et al. 2005; Oosterloo & van Gorkom 2005); they are however not necessarily identified with optically dark halos. Some have been shown to be tidal appendages or to be associated with optical counterparts, e.g. the NE component of the HI1225+01 pair of objects (Giovanelli et al. 1991) and the

object known as VIRGOHI21 (Davies et al. 2004; Minchin et al. 2005, 2007; Haynes et al. 2007); others are thought to be the result of ram pressure stripping in the cluster environment, e.g. the HI feature near NGC 4388 (Oosterloo & van Gorkom 2005). The interactions between sub-groups in Virgo play an important role in the cluster's evolution, acting as a preprocessing step of the material as the galaxies fall into the cluster.

Here we present a catalog of eight 21-cm line sources detected by ALFALFA in the central portion of the Virgo Cluster region which have no obvious optical counterparts. Parameters of the detections and descriptions of their environments are given. Three of the sources were previously reported and one hinted at by other studies and "rediscovered" in the data set of the ALFALFA survey[1].

4.2 Observations and Source Parameters

The sources presented in this paper are part of the ALFALFA catalog and refer to the region 12^h < R.A.(J2000) < 13^h and $+8^\circ$ < Dec.(J2000) < $+16^\circ$. Complete source catalogs of this region have been reported by Giovanelli et al. (2007) and Kent et al. (2008); they are accessible at *http://arecibo.tc.cornell.edu/hiarchive/alfalfa/.* Sources are extracted from the ALFALFA data set via an automated algorithm (Saintonge 2007b), successively inspected by eye, measured and classified according to a code which primarily depends on signal-to-noise (S/N). The objects reported in this chapter are all classified as *bona fide* detections (code 1; see Chapter 3), typically of S/N $\gtrsim$ 6.5, where S/N is defined as (reproduced from Chapter 3 for reference)

$$S/N = \left(\frac{1000F_c}{W_{50}}\right)\frac{w_{smo}^{1/2}}{\sigma_{rms}} \tag{4.1}$$

[1]Elements of this chapter appear in Kent et al. (2007). Reproduced by permission of the AAS.

where F_c is the integrated flux density in Jy km s^{-1}, w_{smo} is either $W_{50}/(2 \times 10)$ for $W_{50} < 400$ km s^{-1} or $400/(2 \times 10) = 20$ for $W_{50} \geq 400$ km s^{-1} [w_{smo} is a smoothing width expressed as the number of spectral resolution bins of 10 km s^{-1} bridging half of the signal width], and σ_{rms} is the rms noise figure across the spectrum measured in mJy at 10 km s^{-1} resolution. All of them have been confirmed by corroborating observations carried out with the Arecibo telescope or with the Very Large Array (VLA) as discussed below. Details of the ALFALFA observations can be found in Giovanelli et al. (2005b) and Giovanelli et al. (2007).

Table 4.1 contains the observed and derived parameters of the HI clouds. Their velocities indicate that an association with the Virgo cluster is possible for most of them, with the exception of the group associated with NGC 4795/4796. The latter is more likely to be in the background of the Virgo cluster, at a distance of ~40 Mpc which is assumed for the clouds in that group.

The fields of each of the sources in Table 4.1 have been inspected in the Sloan Digital Sky Survey and the DSS2 via *Skyview*[2] (Lasker et al. 1990; McGlynn et al. 1994). The contents of Table 4.1 are as follows:

1. Cloud ID number
2. Right Ascension (J2000) of the HI detection
3. Declination (J2000) of the HI detection. These positions are typically accurate to within 30″or better (see Giovanelli et al. 2007)
4. Heliocentric velocity in km s^{-1}
5. Velocity width measured at half peak power in km s^{-1}.

[2] *Skyview* was developed and maintained under NASA ADP Grant NAS5–32068 under the auspices of the High Energy Astrophysics Science Archive Research Center at the Goddard Space Flight Center Laboratory of NASA.

6. Integrated flux in Jy km s^{-1}
7. Signal-to-noise ratio
8. Base 10 logarithm of the HI mass in solar units, assuming HI is optically thin
9. Angular distance from M87 in degrees

For three of the sources, we separately list the parameters of several clumps, identified with letter qualifiers. Figure 4.1 shows locations of the sources within the Virgo cluster region; the grayscale background image shows hard X-ray counts (0.5-2.0 keV) from the ROSAT data set of Snowden et al. (1995), smoothed with a 5′ kernel. The approximate boundaries of the *M* and *W′* clouds are indicated by dashed circles (Binggeli et al. 1993). We note that the fields of the HI clouds often contain one or several small optical objects; the possibility that one of them may be a small dwarf or low surface brightness galaxy associated with the HI source cannot be excluded at this time. The integrated HI spectral profiles for each source are shown in Figures 4.2 and 4.3, labeled as in Table 4.1. We discuss the characteristics of each HI source below.

Cloud 1.–This object, unresolved by the Arecibo beam of 3′.3 × 3′.8, is near the detection limit of ALFALFA at the Virgo distance; S/N and spectrum used are those of the ALFALFA survey observations. That detection has been confirmed by successive, more sensitive Arecibo observations. This is the object with the lowest HI mass in Table 4.1. We note that the Irr galaxy UGC 7003 lies 30′ NW of the HI source at $cz_{\odot}$ = 1286 km s^{-1}, the NGC 4019 group lies 15′ W at $cz_{\odot}$ = 1524 km s^{-1} and UGC 7038 lies 32′ NW at $cz_{\odot}$ = 889 km s^{-1}.

Cloud 2.–This object, also unresolved by the Arecibo beam, lies 3′.8 away from a small optical galaxy for which no optical redshift is known. The optical galaxy AGC 220171 at 121035.6+114539, an apparently undisturbed object classified as a

Table 4.1: ALFALFA Optically Unseen Detections

Identifier	α	δ	$cz_\odot$	$W50$ (ϵ_w)	$\int S\,dV$ (ϵ_f)	S/N	$\log_{10} M_{HI}$	d_{M87}	Comment
-	J2000	J2000	(km s^{-1})	(km s^{-1})	(Jy km s^{-1})	-	$M_\odot$	deg	-
(1)	(2)	(3)	(4)	(5)	(6)	(7)	(8)	(9)	(10)
1	120244.4	+140456	1121± 1	22± 2	0.30 ± 0.02	5.1	7.29	7.0	AO single pixel confirmation
2	120845.5	+115517	1230± 1	29± 2	0.77 ± 0.04	11.6	7.63	5.4	VLA mapping
3	121341.8	+125351	2235± 2	53± 3	1.21 ± 0.07	9.2	8.54	4.2	VLA mapping
4	122619.4	+125330	2246± 5	135± 11	2.05 ± 0.07	14.4	8.77	1.2	VIRGOHI 4 (Davies et al. 2004) VLA map by oosterloo & van Gorkom (2005)
5	122954.7	+075812	473± 5	30± 10	1.13 ± 0.06	10.9	7.87	4.4	Vicinity of M49/NGC 4472 (Sancisi et al. 1987). Aperture synthesis data by Henning et al. (1993).
-									
6a	121755.5	+144445	1984± 1	128± 2	2.09 ± 0.06	16.2	8.13	3.9	Clumps in VIRGOHI 21,
6b	121749.1	+150452	2200± 6	40± 13	0.52 ± 0.05	5.0	7.53	4.1	WSRT data by Minchin et al. (2005, 2007)
6c	121733.8	+142347	2111± 10	65± 20	0.57 ± 0.04	7.3	8.17	3.8	″
-									
7a	122942.8	+094154	524± 7	116± 15	1.16 ± 0.07	8.6	7.87	2.7	Virgo complex
7b	123019.4	+093518	603± 4	252± 7	2.56 ± 0.09	13.1	8.22	2.8	Virgo complex
7c	123025.8	+092801	488± 5	62± 11	2.48 ± 0.07	21.2	8.21	2.9	Virgo complex
7d	123119.0	+092749	607± 4	56± 7	0.72 ± 0.06	6.5	7.67	2.9	Virgo complex
7e	123126.7	+091852	480± 10	53± 21	0.91 ± 0.06	7.6	7.77	3.1	Virgo complex
-									
8a	125504.3	+080613	2629± 3	71± 7	0.72 ± 0.07	6.4	8.43	7.3	NGC 4795/4796 group
8b	125510.2	+080244	2754± 14	407± 27	2.91 ± 0.12	9.4	9.08	7.4	NGC 4795/4796 group
8c	125513.7	+080251	2771± 4	292± 7	2.52 ± 0.10	10.9	9.02	7.4	NGC 4795/4796 group

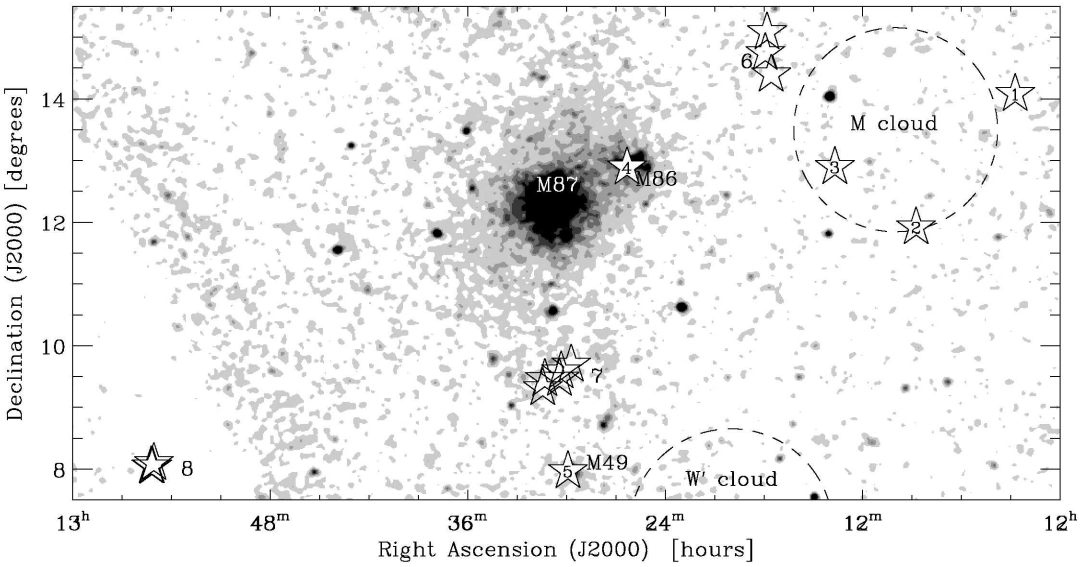

Figure 4.1: Sky distribution of the HI detections listed in Table 4.1. The X-ray peaks of cluster members M87,M86, and M49 are labeled for reference. The gray background is a hard X-ray counts image from ROSAT (Snowden et al. 1995), smoothed with a 5′ Gaussian kernel. The portions of the M and W′ subclouds are indicated by the dashed circles (Binggeli et al. 1993).

BCD, lies 29′ to the SE at a redshift of $cz_{\odot}$ = 1296 km s^{-1}. A VLA map will be discussed in section 4.3.

Cloud 3.–This object, also unresolved by the Arecibo beam, is located in a crowded field - a host of galaxies are in the surrounding periphery at a comparable redshift. The density of galaxies with known optical or HI redshifts in this region is high and 21 are known with 1800 < $cz_{\odot}$ < 2500 km s^{-1} within one degree of the HI source. The nearest optical galaxy with similar velocity is AGC 221651 at 121336.4+130201, 8′ N of the HI feature at $cz_{\odot}$ = 1932 km s^{-1}. A VLA map of the source has been obtained and the results will be discussed in a forthcoming study.

Cloud 4.–The HI source is located 3.6′ SE of M86 (NGC 4406; $cz_{\odot}$ = −244 km s^{-1}), the large Virgo S0 galaxy. It was previously reported by Davies et al. (2004) as VIRGOHI4. They also suggested that the source could lie behind M86. HI synthesis imag-

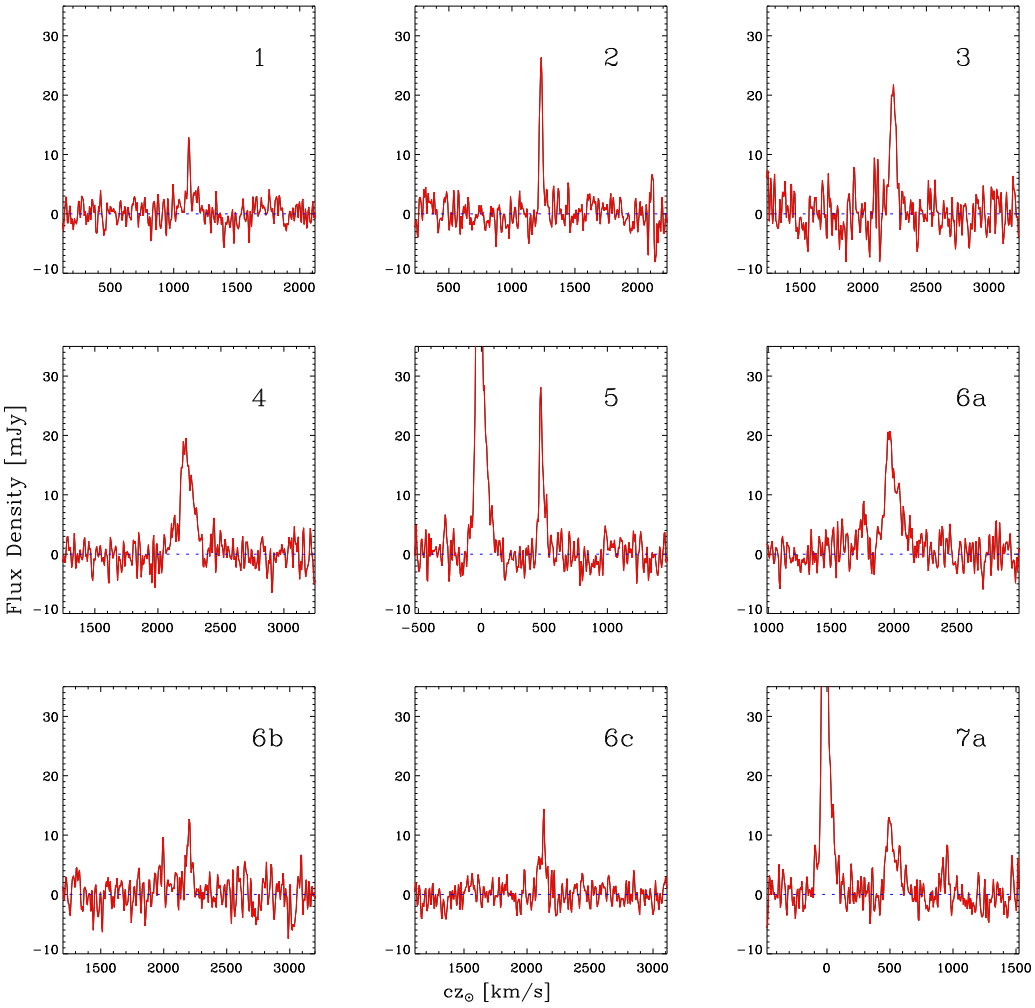

Figure 4.2: Integrated spectral profiles extracted from ALFALFA data cubes for the HI detections listed in Table 4.1.

ing by Oosterloo & van Gorkom (2005) showed the HI source to be a plume extending from NGC 4388($cz_\odot$ = 2524 km s^{-1}) and possibly resulting from interaction between that galaxy and the intracluster gas. Jacoby et al. (2005) indicated that Hα filaments detected could be associated with this plume. In the same vicinity ALFALFA makes a separate detection of M86 (Giovanelli et al. 2007) at negative velocities with the HI centroid located 18″ to the south. The features reported by Bregman & Roberts (1990) are associated with the ALFALFA HI detection of M86.

Cloud 5.–This object was first reported by Sancisi et al. (1987). Later, aperture syn-

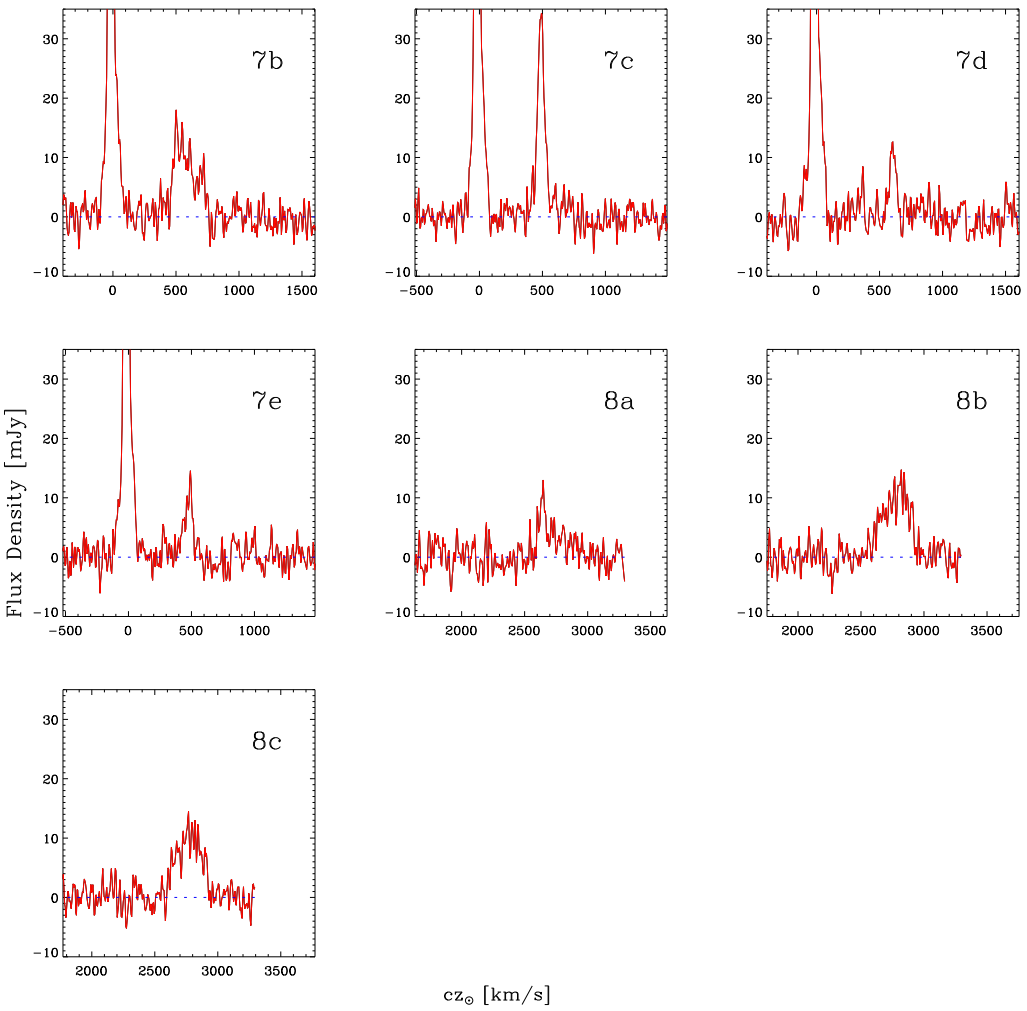

Figure 4.3: Integrated spectral profiles extracted from ALFALFA data cubes for the HI detections listed in Table 4.1.

thesis observations were presented by Henning et al. (1993) and McNamara et al. (1994). The HI source is located 2′.6 southeast of M49($cz_{\odot}$ = 997 km s^{-1}) and it is proposed to be related to the interaction between M49 and the dwarf irregular UGC 7636($cz_{\odot}$ = 276 km s^{-1}).

Cloud 6: NGC 4254 tail.–Two sources(6*a*&*b*) are the brightest clumps in a stream found in the vicinity of NGC 4254 (M99; $cz_{\odot}$ = 2407 km s^{-1}) an Sc galaxy at a projected distance 3.7° northwest of M87. The brightest of the two is an object first detected at Jodrell Bank (Davies et al. 2004; Minchin et al. 2005) and more recently mapped at

Westerbork by the same team (Minchin et al. 2007). Dubbed "VIRGOHI21", it was proposed by that group that the source is a giant "dark galaxy." The ALFALFA observations clearly show the feature to be part of a stream connected to NGC 4254, continuously extending some 250 kpc to the North of that galaxy. The feature appears to be of tidal origin. A third ALFALFA detection (6*c*) lies 18′ W of NGC 4254. A more detailed analysis of the ALFALFA evidence on this object is given in Haynes et al. (2007). A zeroth moment map of both the tail component and NGC 4253 extracted from the ALFALFA data cubes is shown in Figure 4.4. Also presented is a rotation curve along the tail obtained with *L*-band wide single pixel observations. Not only does the tail clearly connect to NGC 4254 in velocity space, but it also exhibits a gradient similar to a circular velocity curve.

Cloud 7.–A complex of five HI clouds, it projects between M87 and M49, roughly 3° south of the former. The five clouds, spread in velocity between 480 and 607 km s^{-1}, extend over approximately 35′ in the plane of the sky, or 200 kpc at the Virgo cluster distance. In HI mass, the clouds range between 0.5×10^8 and 2.0×10^8 $M_\odot$. VLA observations have been obtained and clouds 7c and 7d have been clearly detected. Detailed observations and interpretations of these objects are discussed in Chapter 5.

Cloud 8.–Three clouds comprise an HI complex that surrounds the SB0/a galaxy NGC 4795($cz_\odot$ = 2781 km s^{-1}) and its dwarf companion NGC 4796($cz_\odot$ = 2406 km s^{-1}). It was previously noted that a large flux measurement discrepancy between Arecibo and Effelsberg measurements was likely due to an offset of the HI from the center of the NGC 4795/4796 pair (Hoffman et al. 1989b). Later observations at Arecibo by Duprie & Schneider (1996) are suggestive of an extension of the HI emission from NGC 4796 towards its irregular companions UGC 8042/5, perhaps arising from a tidal interaction. ALFALFA maps show that HI emission surrounds the NGC 4795/6 pair,

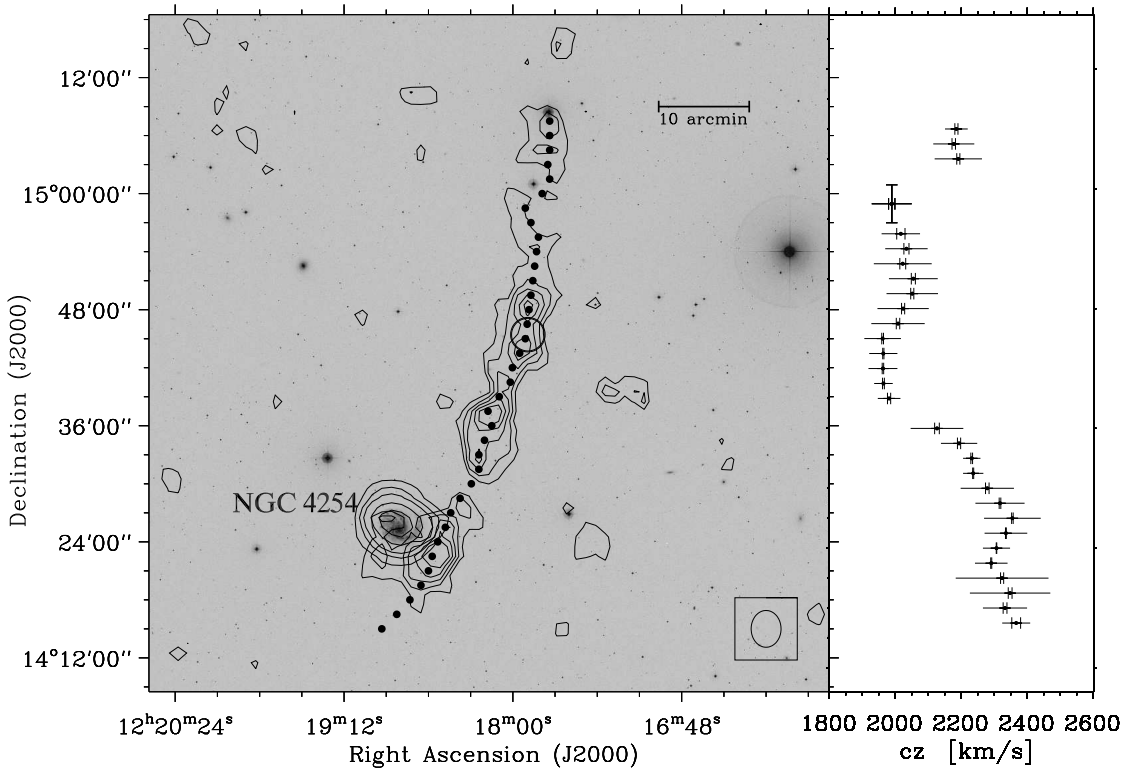

Figure 4.4: NGC 4254 vicinity and HI data. NGC 4254 is a $m = 1$ Sc spiral galaxy located at a projected distance 3.7° northwest of M87. The galaxy's heliocentric redshift is $cz_{\odot} = 2404$ km s^{-1}. Left: HI flux contours extracted from the ALFALFA survey data set, which mapped the full field represented in the image, superposed on a 2nd generation Digital Sky Survey Blue image (Lasker et al. 1990). The 36 filled dots indicate the locations of beam centers for the successive *L*-band wide observations. The contours centered on NGC 4254 are at 10, 15, 20, 30, and 40 Jy beam^{-1} km s^{-1}, integrated from 2259 to 2621 km s^{-1}. The contours for the HI stream are at 0.35, 0.52, 0.70, 0.87, and 1.0 Jy beam^{-1} km s^{-1}, integrated from 1946 to 2259 km s^{-1}. Note the difference in dynamic range of contours for the galaxy and the stream, selected for viewing ease. The 3′ circle in mid stream indicates the position of VIRGOHI21 reported by Minchin et al. (2005). The ellipse on the bottom right indicates the size of the Arecibo beam. Right: The velocity of the HI emission peak as seen in *L*-band wide pointings. Some of the *L*-band wide spectra yielded poor baselines or poor peak definition. Figure adopted from Haynes et al. (2007). Reproduced by permission of the AAS.

and that it is indeed connected to the two nearby galaxies, UGC 8045 and UGC 8042, which are respectively at $cz_{\odot}$ = 2801 km s^{-1} and $cz_{\odot}$ = 2856 km s^{-1}. The HI masses computed in Table 4.1 assume a distance of ~40 Mpc. The kinematics of the HI indicate that all the galaxies in this system are at a comparable redshift and are interacting as a group. Figures 4.5 and 4.6 show the optical and HI environments from the DSS 2 Blue plates and ALFALFA data respectively.

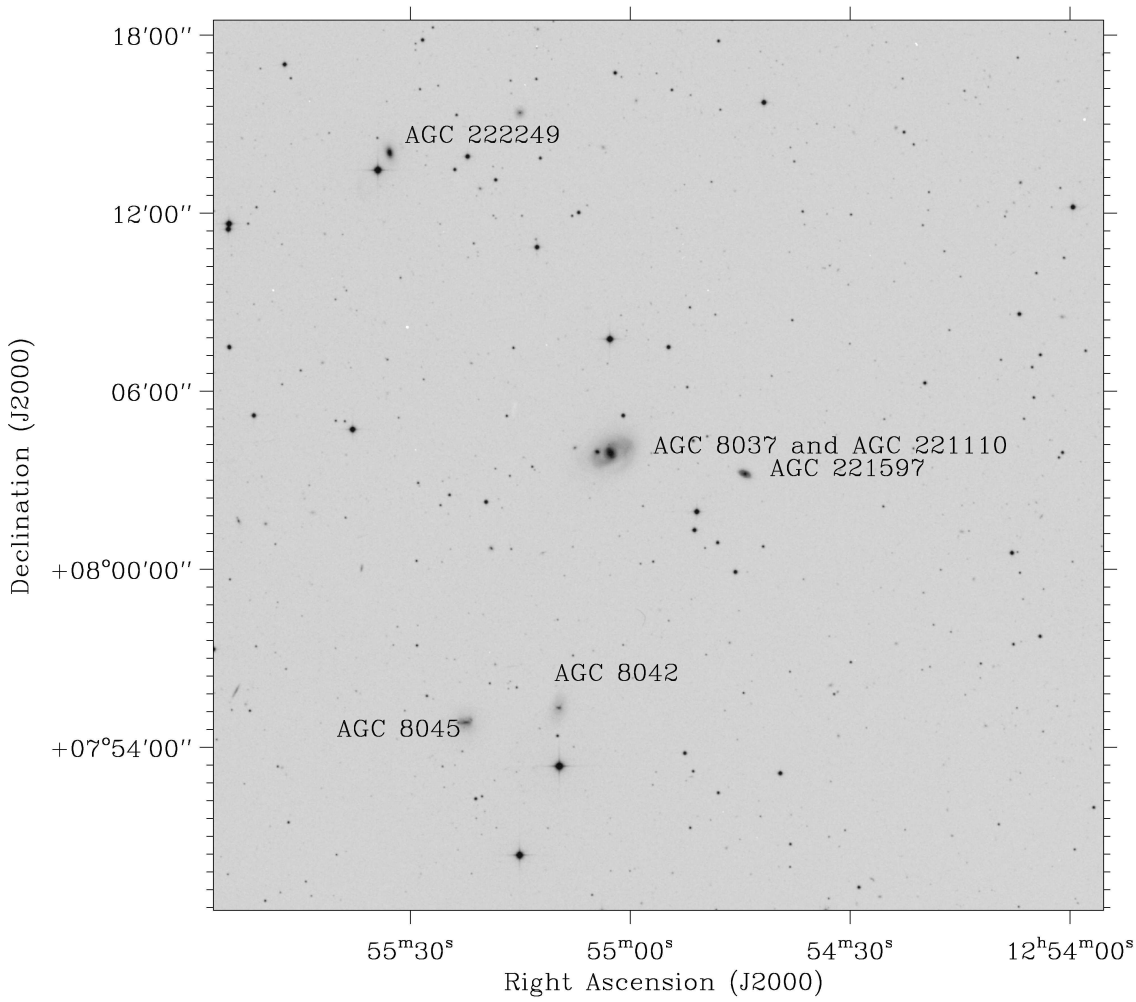

Figure 4.5: Cloud 8 (Table 4.1) environment. DSS 2 Blue optical image showing SB spiral galaxy UGC 8037 (NGC 4795) and nearby galaxies sharing similar redshift measurements.

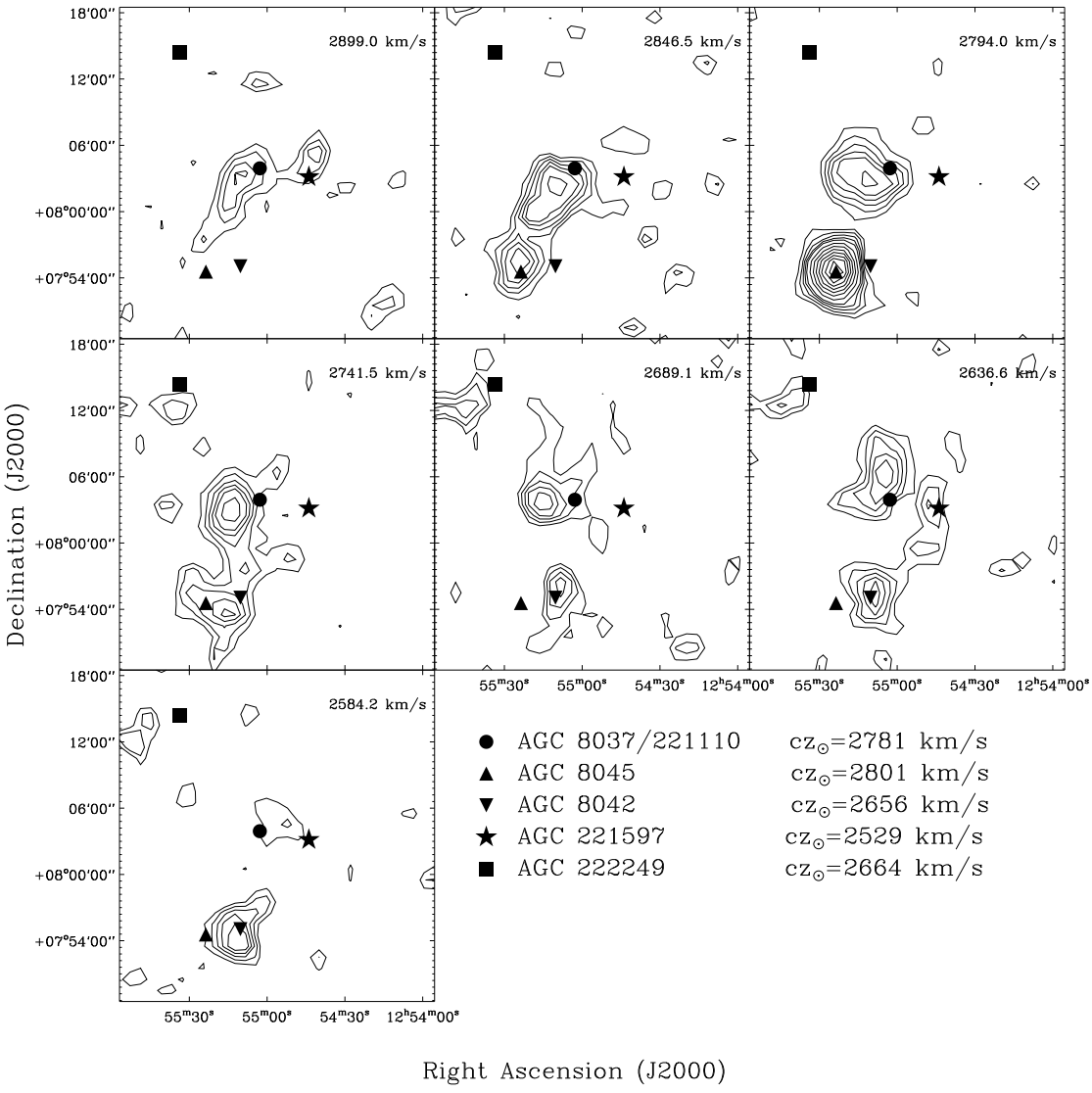

Figure 4.6: Cloud 8 (Table 4.1) environment. Channel maps of HI data extracted from ALFALFA data cubes for the UGC 8037 (NGC 4795) environment. The flux contours are at the levels of 2,3,4,5 and 8-28 mJy beam^{-1} in 2 mJy beam^{-1} intervals.

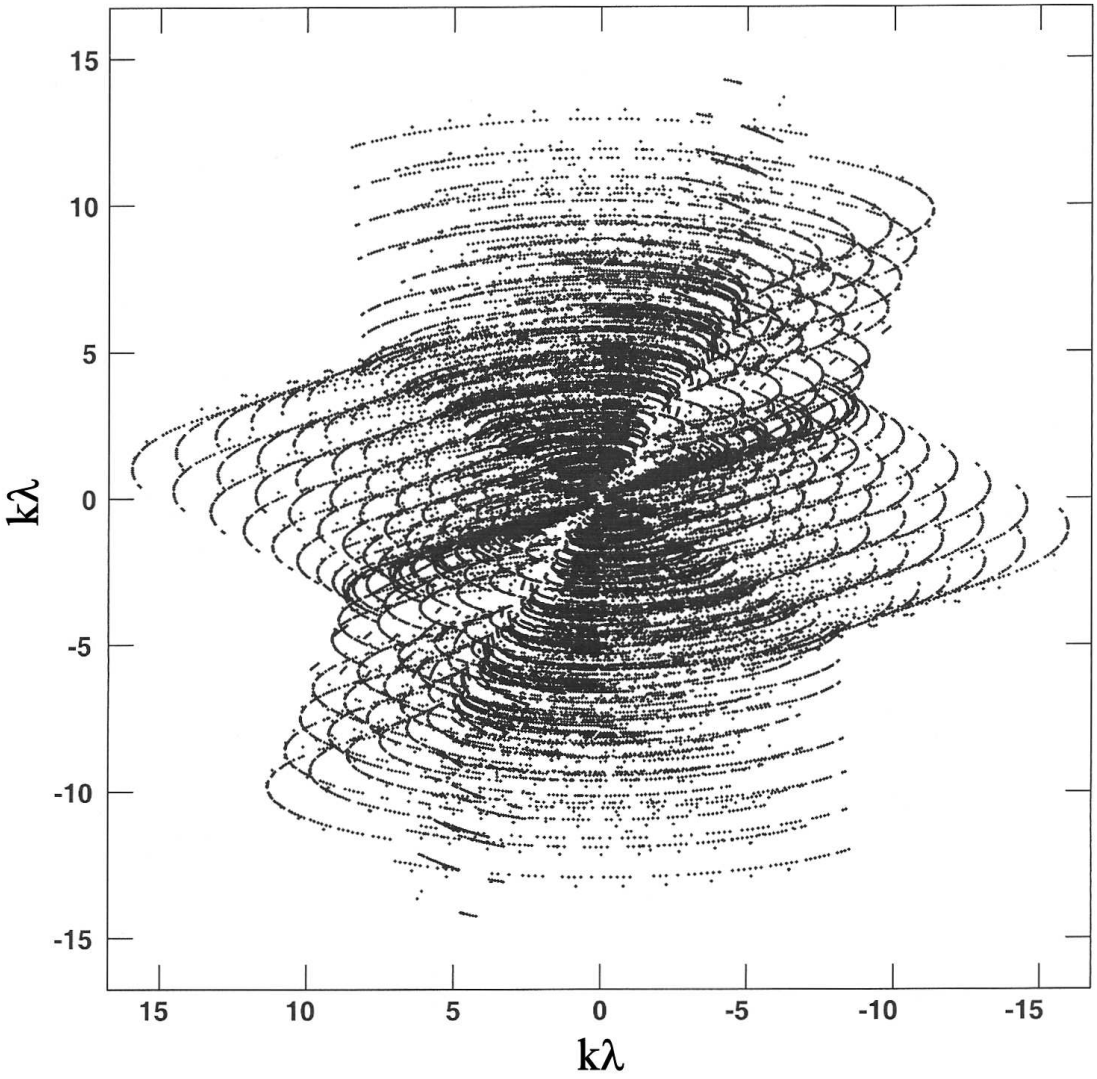

Figure 4.7: VLA U-V plane coverage for a 10 hour observation of Cloud 2 from Table 4.1.

4.3 Discussion

The characteristics of the eight sources reported here are quite diverse. They can be grouped into three categories: isolated objects, objects in the vicinity of large galaxies, and disturbed objects that could be remnants of an encounter with a larger system, such as the collective cluster potential. Except for cloud 8, the projected distances to M87

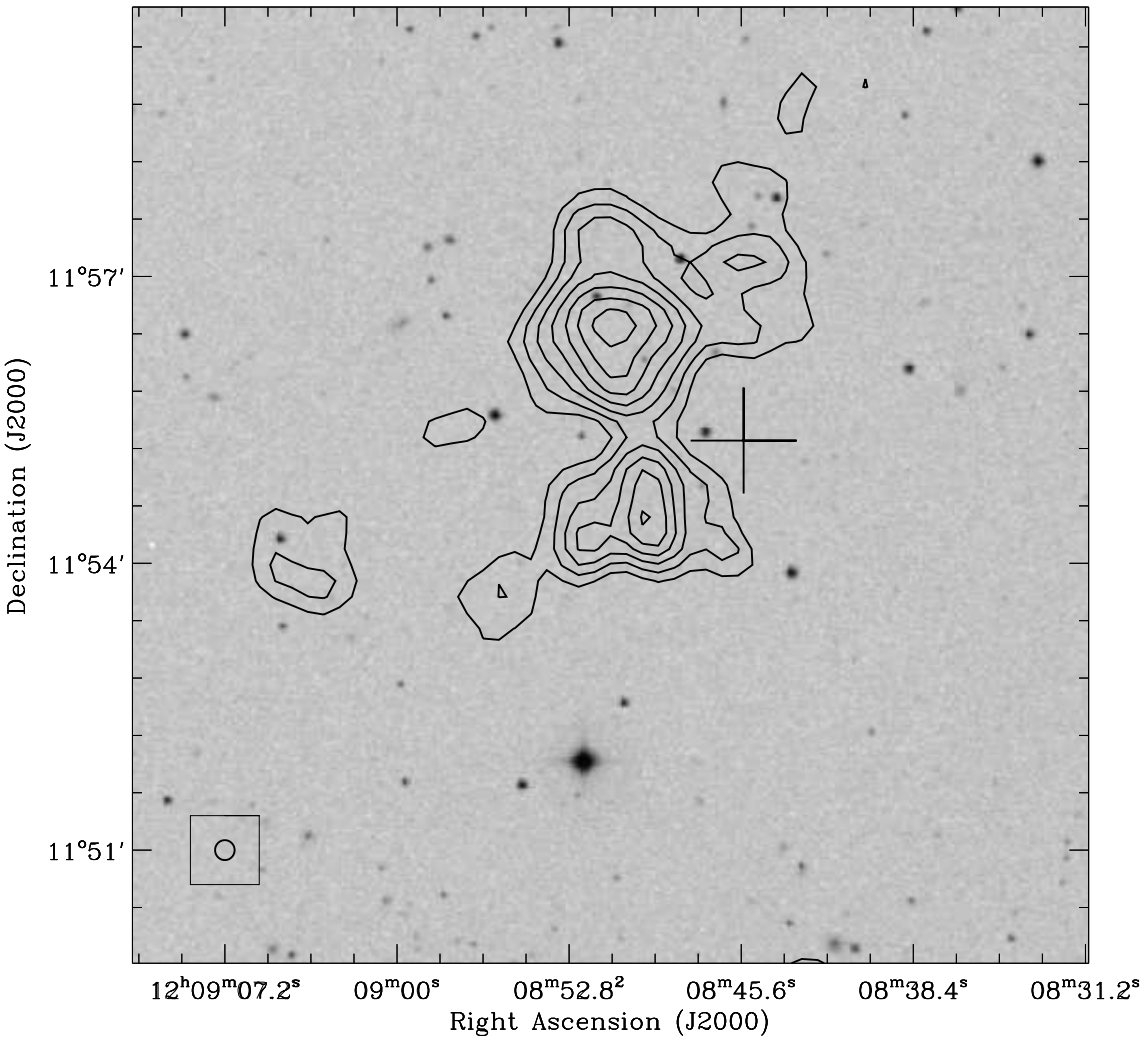

Figure 4.8: VLA C-array moment zero HI map of Cloud 2 from Table 4.1. The map was created using uniform weighting. The map rms is σ = 3.8 mJy beam^{-1} km s^{-1}, with contours indicating 3, 4, 5, 6, 7, 8 and 9σ. The large cross indicates the centroid of the Arecibo detection (3′.8 × 3′.3 beam). The synthesized beam size is indicated in the lower left corner.

and heliocentric velocities place the HI sources within the canonical boundaries of the Virgo Cluster, as defined by Binggeli et al. (1985).

Clouds 4 and 5 have been extensively studied in the past, using higher resolution aperture synthesis data which indicate a clear association with Virgo cluster galaxies M49 and NGC 4388. The proximity to these galaxies and the cluster environment are important in determining their properties. The clouds in the vicinity of NGC 4795 (cloud 8) are most likely the result of tidal stripping in interacting members of a close group, not an uncommon occurrence.

Cloud 6 has raised significant attention, as it was proposed to be a rare representative of a category of massive, yet starless galaxies. The ALFALFA observations clearly show that rather than being an isolated "dark galaxy," this object is an extended stream connected to NGC 4254. The velocity field obtained with *L*-wide observations can be used as a timing tool as a result of the coupling of the tail to a rotating disk and the gravitational potential well of the cluster (Haynes et al. 2007).

ALFALFA observations of clouds 1, 2 and 3 offer no clear hints as to their origin. They are all unresolved by the Arecibo beam, hence their HI is contained within a region $\sim$ 10 kpc diameter or less. The HI masses of the clouds are relatively low, especially for clouds 1 and 2, and the lack of a size determination impedes an estimate of their dynamical masses; upper limits for the latter on order of 1–6$\times 10^8$ $M_\odot$ can be obtained if one assumes turbulent or rotational motion amplitudes as indicated by the velocity widths. These objects are projected near or within the boundaries of the M cloud, a loose subclump thought to be behind and falling into the main cluster around M87, although little coherence in the velocities of the trio exists to firmly substantiate such association. At any rate, they appear to be relatively isolated and far removed from the central parts of the cluster so that gravitational, rather than hydrodynamical processes

involving the intracluster gas, are more likely to be invoked in explaining their nature. While the mean number density of VCC galaxies in the M cloud region is less than 1.5 $\times 10^{-3}$ (arcmin)$^{-2}$ (Binggeli et al. 1985; Schindler et al. 1999), cloud 3 lies in a locally overdense region, where galaxy-galaxy interactions may be more frequent. It cannot be excluded however that these clouds may be primordial, low mass halos, perhaps associated with small dwarf or low surface brightness optical counterparts. Analysis of recently obtained VLA data and planned follow-up optical studies will help elucidate this issue.

Cloud 7 is resolved by ALFALFA data into several separate clouds, spread over more than 200 kpc (if located at the cluster distance) and 250 km s^{-1} in extent. With a mean velocity near 540 km s^{-1}, the complex could well be located in the foreground of the cluster, although cluster galaxies of similar redshift are found in the vicinity. Most notably, NGC 4424, an SBa at $cz_{\odot}$ = 476 km s^{-1} is located approximately 40′ to the west of the complex. ALFALFA and VLA HI maps of that object (Chung et al. 2007), as well as CO maps (Cortés et al. 2006) indicate that its structure is disturbed, showing an appendage extending to the south of the galaxy, pointing opposite the direction of the cloud complex. Assuming the whole of the complex is not a gravitationally bound unit, the velocity differences between the individual clouds will separate them at the approximate rate of $\sim$ 150 kpc Gyr^{-1}. Differential motions of this amplitude are consistent with tidal forces within the cluster potential and suggest the complex may disperse within a cluster crossing time. A more detailed analysis based on ALFALFA data is discussed in Chapter 5.

While a detailed statistical study of the ALFALFA catalogs in the Virgo regions awaits completion of the survey effort therein, it is interesting to note that ALFALFA does not detect very large numbers of low HI mass sources in the cluster. This is an in-

dication that, at least in the cluster region, the HI mass function faint end slope does not rise sufficiently to contribute appreciably to solving the "substructure" problem mentioned in the chapter introduction.

4.3.1 Future Work: VLA Observations of Cloud 2

Cloud 2 was observed with the Very Large Array in C configuration on November 26, 2006. The Cloud 2 detection was observed in 30 minute intervals for 12 hours with observations of 3C147 as a flux calibrator at the beginning and VLA catalog source 1120+143 as a phase calibrator for 4 minutes between each pointing. The system configuration used a 1.56 MHz bandwidth with 128 channels centered at 1.4147 MHz. The resulting velocity resolution at the band center was 2.5 km s^{-1} before Hanning smoothing. Doppler tracking was employed during the observations.

Standard calibration and reduction was followed using the Astronomical Image Processing System (AIPS; Napier et al. 1993). The map is free of any strong continuum sources, allowing for subtraction of continuum emission via linear fits. The U-V plane coverage for the observation is shown in Figure 4.7. A uniform weighting was applied to the cube, as was a CLEANing algorithm for reduction of sidelobe contamination (Schwarz 1978). A data cube using uniform weighting was created, with pixel elements smoothed to 10″. The resulting preliminary total intensity map is shown in Figure 4.8.

The map RMS is σ =3.8 mJy $beam^{-1}$ km s^{-1}, with contours indicating 3, 4, 5, 6, 7, 8 and 9σ. The large cross indicates the centroid of the Arecibo detection (3′.8 × 3′.3 beam). The source is resolved into three extended clumps. The two main clumps are of high S/N, located near the pointing center and appear to be connected by a bridge. The peaks are separated by ∼2′ in space (∼9 kpc at the Virgo distance). A third

detection lies ∼3′ southeast of the northern most clump. The small, compact group of HI detections composing Cloud 2 are spread over no more than 15′ to 20′ in extent, with a velocity spread of ∼20 km s^{-1}. The aperture synthesis data reveals that Cloud 2 is similar to the Cloud 7 complex, albeit on different size scales. Aperture synthesis observations have also been obtained for other cloud complexes in Table 4.1 and will be presented in a later publication (Kent et al. 2008).

CHAPTER 5

A HI CLOUD COMPLEX IN VIRGO

The study of the cold gas content in extragalactic systems plays an important role in understanding their formation and evolution. Not only does the gas content reveal information on the star formation potential of a galaxy, it also traces the dynamic history and response to the surrounding environment whether the galaxy inhabits a dense cluster or unpopulated field. The fingerprint of galactic collisions and ram pressure stripping effects can also been seen with the detection of gaseous fragments and clumps in the vicinity of groups. Combined with data from other wavelengths, the gas content of galaxies place a crucial astrophysical component with the stellar and dust components of other studies.

The 21cm spectral line of neutral hydrogen serves as an important tool for measuring the cool, neutral gas component of galaxies, as well as a redshift indicator and kinematical probe. The HI line also has the distinction of being able to detect gas rich systems with little or no stellar emission, giving blind HI surveys the sensitivity advantage of detecting a population not seen by optical surveys. Studies with these optical surveys do not yield the numbers of low mass objects predicted by the hierarchical galaxy formation scenario (Moore et al. 1998; Somerville 2002). HI surveys might be able to, in part, shed light on this "missing satellite problem". Arguments have also been made that dark galaxies could significantly outnumber normal galaxies at high redshift (Hawkins 1997). As such, the extragalactic population could be very undersampled; the existence of these primordial dark matter halos would have important cosmological implications. Detecting baryon deficient halos that are dominated by dark matter is a difficult task, but the detection of optically-faint, gas-rich systems could yield, in part, some of the missing mass put forth by this substructure problem. If the dark galaxies contain baryons

in the form of cool gas with no stars, they would be detectable in HI (Giovanelli et al. 2005b; Davies et al. 2006). However, it is a challenge to distinguish primordial dark matter halos from gaseous tidal debris, especially in higher density environments where interactions are more prevalent.

HI clouds reported in the literature have typically been associated with optical counterparts, nearby groups, or large disk galaxies (Schneider et al. 1983; Sancisi et al. 1987; Giovanelli & Haynes 1989; Chengalur et al. 1995; Kilborn et al. 2000; Ryder et al. 2001). Others are the result of tidal or harassment-type disturbances from interactions with a cluster (Minchin et al. 2005, 2007; Oosterloo & van Gorkom 2005; Haynes et al. 2007). Previous serendipitous detections of HI clouds near the Virgo cluster have revealed stellar counterparts upon optical follow-up. A small dwarf galaxy was detected around the well–known HI1225+01 (Giovanelli & Haynes 1989), coinciding with the northeast HI clump. The southwest clump of HI1225+01 has failed to yield any optical light down to a surface magnitude limit of 27 mag arcsec^{-2} (Djorgovski 1990; Impey et al. 1990; Salzer et al. 1991). Another reported HI feature, VIRGOHI21, was detected north of spiral galaxy NGC 4254 (Minchin et al. 2005), as well as in the data set of the Arecibo Legacy Fast ALFA Survey, which provides full coverage of the region. These observations show that VIRGOHI21 is not isolated, but exhibits a clear HI tail leading to NGC 4254. Higher sensitivity follow-up observations with Arecibo's single pixel *L*-band receiver have confirmed this connection (Haynes et al. 2007). A large spiral galaxy's interaction with a cluster can occur via a variety of mechanisms, the most common being ram pressure stripping (Davies & Lewis 1973; Chamaraux et al. 1980). The effects of ram pressure stripping can be seen through the HI deficiency noted in Virgo cluster galaxies (Haynes & Giovanelli 1986). Oosterloo & van Gorkhom (Oosterloo & van Gorkom 2005) reported the discovery of a HI cloud in the vicinity of Virgo spiral NGC 4388 with a HI mass of 3.4×10^8 $M_\odot$, separated into distinct clumps. Oosterloo &

van Gorkom (2005) show a clear connection to NGC 4388, and measure column densities above 10^{20} cm^{-2}. Further evidence of cluster induced effects can be seen with spiral galaxies exhibiting asymmetries in their HI disks (Haynes & Giovanelli 1984; Cayatte et al. 1990; Chung et al. 2007). Intergalactic features detected in HI in the vicinity of nearby galaxies are typically disk material, appearing as separate entities after being subjected to tidal forces of neighboring galaxies (Haynes et al. 1984). It has also been shown that galaxies moving on high speed trajectories can be "harassed" by other galaxies and the large gravitational potential of the cluster. Evidence for these episodes of galaxy harassment is seen via large tidal streams (~200 kpc in size) and remnant clumps of gas in the cluster near large spirals. As the outer parts of Virgo have not reached virial equilibrium, the peripheral environment consists of a population of large galaxies moving at high orbital speed during the process of infall (Moore et al. 1996). While the fingerprint of galactic collisions via tidal remnants are observed in a variety of groups and close encounters between large disk galaxies (Toomre & Toomre 1972; Hibbard et al. 2001), Virgo affords the opportunity to study nearby examples of galaxies under the influence of a cluster environment. HI clouds in a cluster environment can be categorized as a transient phenomenon, offering an explanation as to why they are not seen in large numbers.

Virgo, the nearest rich cluster of galaxies, provides a nearby environment for which to partake in the study of galaxy formation, evolution, and interaction. Much effort has been placed in studying the Virgo population across the entire electromagnetic spectrum, as different wavelengths are sensitive to different populations of galaxies and their surrounding intracluster environment. With over 1300 cataloged detections (Binggeli et al. 1985), the Virgo cluster's over–density of galaxies extends over 300 square degrees in the sky, gathered into several subclumps. These clumps are centered around large elliptical galaxies, including M87 for the main clump, and M49 for the south-

ern subclump. Morphology–density relations (Dressler 1980) imply that the density of early-type galaxies decreases while that of late-types increases with increasing distance from these clump centers. Thus the vulnerable gas disks of late-type galaxies can be disturbed, often dramatically, by the cluster potential, neighboring galaxies and the intracluster medium (ICM). Whether or not such "HI clouds" can be formed primordially as a result of gravitational collapse onto dark matter halos is an important topic in galaxy formation (Taylor & Webster 2005; Davies et al. 2006). Due to the high density of galaxies in the vicinity, it is a challenge to determine whether such HI cloud detections in a cluster environment are primordial in nature. An open mind should be kept on the possibility that such HI clouds may constitute a small fraction of the missing satellites required by the results of N-body simulations.

Optical sky surveys of Virgo reveal the morphological nature of the cluster members. The Digital Sky Survey (Lasker et al. 1990) offers deep optical imaging, as does the Sloan Digital Sky Survey (York et al. 2000). The SDSS also offers photometry and targeted spectroscopy of millions of bright galaxies, providing information on chemical abundances and redshift information. A catalog of Virgo galaxies with HI and photometric data have been compiled on the GOLDMINE website (http://goldmine.mib.infn.it/ ; Gavazzi et al. 2003). Further distance information has been provided by the Advanced Camera for Surveys Virgo Cluster survey (ACS), focusing on early-type galaxies and their environments (Peng et al. 2006b). HST observations from this project allow for the surface-brightness fluctuation method to be used as a distance indicator (Mei et al. 2007). HI surveys also have a crucial role to play in understanding the Virgo cluster. The HI Parkes All-Sky Survey (HIPASS; Barnes et al. 2001) has surveyed 30000 deg^2 in a blind extragalactic HI survey, part of which covers Virgo in the declination region $+2^\circ <$ Decl. $< +20^\circ$. For the area of sky defined in Chapter 3, HIPASS detects 131 sources, in contrast to the 2345 sources detected by the ALFALFA survey. Understand-

ing the cold gas characteristics of the Virgo cluster is of the utmost importance, as HI can more effectively reveal the effects of the cluster environment on galaxies (Davies & Lewis 1973). The HI content of galaxies can be greatly affected by a number of mechanisms. Ram pressure stripping, gas evaporation and galaxy collisions can alter the gas content and structure in galaxies. However, in a cluster environment, disk galaxies moving at high speed, ram-pressure stripping, and the large gravitational potential of Virgo all contribute to the possibility of fragmentation or dissipation of HI gas in this environment. This is clearly seen in disks that have shrunk and correlates with the amount of HI deficiency (Haynes & Giovanelli 1986; Cayatte et al. 1990). Ram pressure stripping is very efficient in the core as opposed to the outlying periphery, where the density of the hot X–ray gas is lower.

The Arecibo Legacy Fast ALFA survey is providing insight into the HI environment of Virgo and many other high priority targets (Giovanelli et al. 2005b). The probability of detecting such objects can be increased in a blind HI survey covering a wide area of sky - a strategy employed by ALFALFA. While the HI content of many individual spiral galaxies has been mapped in detail with interferometry (Cayatte et al. 1990, 1994; Chung et al. 2007), none have completely covered the Virgo core region as ALFALFA has accomplished so far. Understanding the global cluster environment in HI as well as the characteristics and dynamics of HI clouds (primordial or recycled gas), is a major goal of the ALFALFA survey. The survey aims to study and characterize the HI environment local universe, including that of the Virgo cluster. ALFALFA will provide a fair, well-sampled, and homogeneous spectral data set, covering 7000 deg^2 of the high galactic latitude sky out to a redshift of $cz_\odot \sim 18000$ km s^{-1}. Over 425 deg^2 of the Virgo cluster in the range $11^h36^m <$ R.A.(J2000) $< 14^h00^m$ and $+4^\circ <$ Decl.(J2000) $< +16^\circ$ have been completely surveyed. Catalogs and extracted parameters for this data set are currently being compiled for publication (Giovanelli et al. 2007; Kent et al. 2008). A

key feature of the survey is its sensitivity to low HI mass objects – ALFALFA will provide a complete HI census down to $2 \times 10^7 M_\odot$ at the Virgo distance. Sampling the low-mass population will be key in determining the HI mass function in the cluster environment, as well as in the field. ALFALFA will provide a cosmologically fair sample of the local universe, enabling a determination of the faint end slope of the HI mass function. However, distance uncertainties toward Virgo will make HI mass determinations challenging, and will require follow-up observations in other spectral regimes to obtain primary distance indicators.

The ALFALFA data set to date has yielded many interesting detections, including new high-velocity clouds, tidal streams in the vicinity of large spiral galaxies, and small clouds with no apparent optical counterparts. The detected HI clouds add to the evidence of tidal and hydrodynamic interactions in Virgo, some of them similar to those revealed by the diffuse intracluster light (Mihos et al. 2005). Other streams and tidal debris similar in nature have also been detected in the ALFALFA survey, and will be discussed in later work.

In this chapter we give a detailed description of a multi-component HI cloud complex in the Virgo cluster region initially reported by Kent et al. (2007). In section 5.1 we describe the observations and data reduction method within the context of the ALFALFA extragalactic HI survey and cloud detections made with that data set. In section 5.2 we discuss the environment of the cloud complex. In section 5.3 we discuss possibilities and scenarios for the existence of such an object in the greater Virgo Cluster environment. Throughout the paper we assume a distance to the Virgo Cluster of $D_V = 16.7$ Mpc, and adopt the heliocentric optical definition for all velocities.

5.1 Virgo Cloud Complex

The cloud complex was discovered in the ALFALFA data obtained in the Spring 2005 campaign, which sampled the Virgo core region ($12^{\rm h} < \alpha < 13^{\rm h}, 8^\circ < \delta < 16^\circ$). The data presented here are taken from the processed grid centered at $\alpha = 12^{\rm h}20^{\rm m}, \delta = 9^\circ 00'$ (J2000). The characteristics of the ALFALFA grids from which the data are taken are summarized in Table 2.1.

Table 5.1: Single-Dish Cloud Properties from the ALFALFA Survey

Cloud	α, δ (J2000)	$cz_\odot$ (km s^{-1})	$W50$ (km s^{-1})	F_c (Jy km s^{-1})	S/N	$\log_{10}(M_{HI}/M_\odot)$
(1)	(2)	(3)	(4)	(5)	(6)	(7)
C1	12 30 25.8, +09 28 01	488 ± 5	62 ± 11	2.48 ± 0.07	21.2	8.21 ± 0.01
C2	12 31 19.0, +09 27 49	607 ± 4	56 ± 7	0.72 ± 0.06	6.5	7.67 ± 0.04
C3	12 29 42.8, +09 41 54	524 ± 7	116 ± 15	1.16 ± 0.07	8.6	7.87 ± 0.03
C4	12 30 19.4, +09 35 18	603 ± 4	252 ± 7	2.56 ± 0.09	13.1	8.22 ± 0.02
C5	12 31 26.7, +09 18 52	480 ± 10	53 ± 21	0.91 ± 0.06	7.6	7.77 ± 0.03

The cloud complex is located at $\alpha \sim 12^{\rm h}30^{\rm m}, \delta \sim 9^\circ 30'$ – this places it 2.9° (845 kpc in projection) South of M87 and 1.5° (432 kpc in projection) north of M49. The Virgo galaxy density in this region is $\sim 6 \times 10^{-3}$ galaxies arcmin^{-2} (Schindler et al. 1999). The nearest galaxies to the complex are NGC 4424 and NGC 4445 at similar recessional velocities. We discuss the environment of the complex further in section 5.2.

The complex consists of five distinct emission features or "clouds", which we denote C1–C5. In Chapter 4, this complex is listed as Cloud 7. The clouds in the complex are listed in Table 5.1 in increasing distance from the central and largest cloud. Together, they span nearly 35′ (170 kpc in projection) on the sky and 130 km s^{-1} in velocity. Channel maps of the ALFALFA data set in the vicinity of these detections are shown in Figure 5.1, and total intensity (zeroth moment) and intensity-weighted velocity maps of

the region is in Figure 5.2. An integrated spectral profile for each cloud is presented in Figure 5.3.

The individual properties of the clouds in Table 5.1 are computed in the manner described in Chapter 3. The spatial centroid of each cloud is in Column (2). Its accuracy depends on the source strength, and varies from an average of $\sim 15''$ for the brightest features to $\sim 30''$ for the faintest ones. The heliocentric velocity $cz_{\odot}$, width at 50% of the peak $W50$ and total flux F_c of the integrated spectral profiles in Figure 5.3 are in Columns (3)–(5). The signal-to-noise ratio S/N of the detections is in Column (6), as computed by Equation 3.2. The HI mass M_{HI} for each cloud is in Column (7), and is computed assuming that the clouds are optically thin and at the Virgo distance D_V= 16.7 Mpc:

$$\frac{M_{HI}}{M_{\odot}} = 2.356 \times 10^5 \, D_V^2 \, F_c \tag{5.1}$$

where D_V is in Mpc and F_c is in Jy km s^{-1}. The uncertainties on M_{HI} in Table 5.1 and elsewhere do not include that in the distance adopted, which is poorly constrained due to the large peculiar velocities of objects near Virgo (Binggeli et al. 1987; Tonry et al. 2000; Vollmer & Huchtmeier 2003).

VLA measurements for C1 and C2 have also been obtained and are shown in Table 5.2 (Spekkens 2008).

5.1.1 Cloud Morphologies and Kinematics from ALFALFA data

Cloud C1: C1 is the main cloud in the complex and the highest S/N detection in this region. It is marginally resolved by the ALFA beams (Figure 5.2). Its integrated profile is symmetric and narrow with a peak flux density of 38 mJy (Figure 5.3). A new detection by ALFALFA, C1 has one of the largest HI masses in the complex at

Table 5.2: VLA Properties of C1 and C2

Cloud	$(\alpha, \delta)'$	$cz'_{\odot}$	$W50'$	F'_c	a'_{HI}	$\log_{10}(M'_{HI})$	$\log_{10}(M'_{dyn})$
	(J2000)	(km s^{-1})	(km s^{-1})	(Jy km s^{-1})	$'$	$M_{\odot}$	$M_{\odot}$
(1)	(2)	(3)	(4)	(5)	(6)	(7)	(8)
C1	12 30 24,+09 28 20	488 ± 6	78 ± 11	2.14 ± 0.07	2.7 ± 0.3	8.15 ± 0.02	9.36 ± 0.1
C2	12 31 18,+09 29 25	597 ± 3	38 ± 5	0.57 ± 0.06	1.5 ± 0.3	7.57 ± 0.05	8.48 ± 0.1

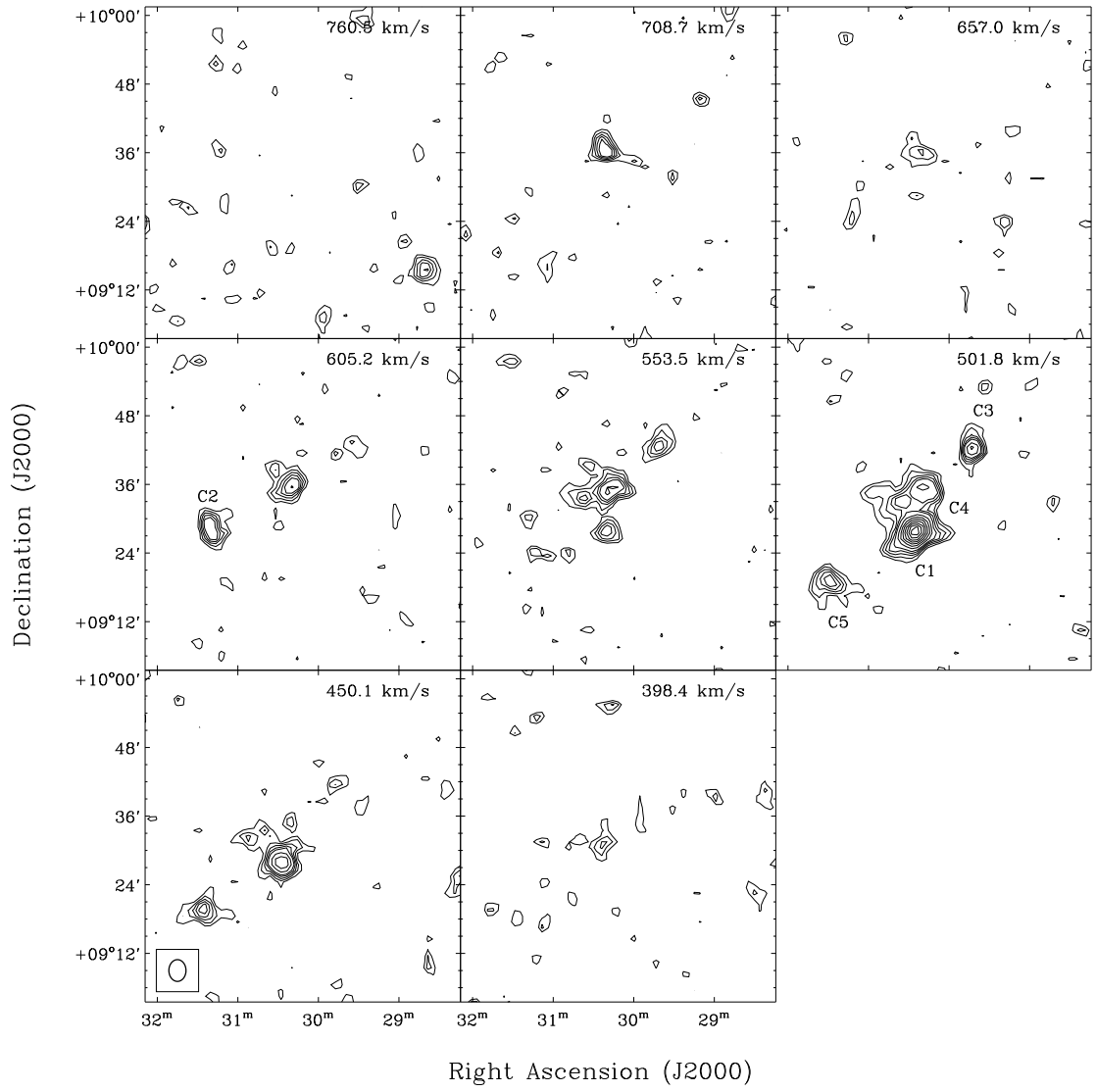

Figure 5.1: Channel maps of the cloud complex from 760 km s^{-1} to 400 km s^{-1} in the ALFALFA survey data. Contours are at (2, 3, 4, 5) and 6–26 mJy $beam^{-1}$ in 2 mJy $beam^{-1}$ intervals. The velocities indicated in the upper right corner represent the central channel velocity of the map. The maps are boxcar smoothed at the indicated velocities +/- 5 channels (at $\sim$ 5 km s^{-1} resolution). The five HI cloud detections are indicated as C1 through C5. The ellipse in the lower left indicates the ALFALFA beam size ($3'.3 \times 3'.8$).

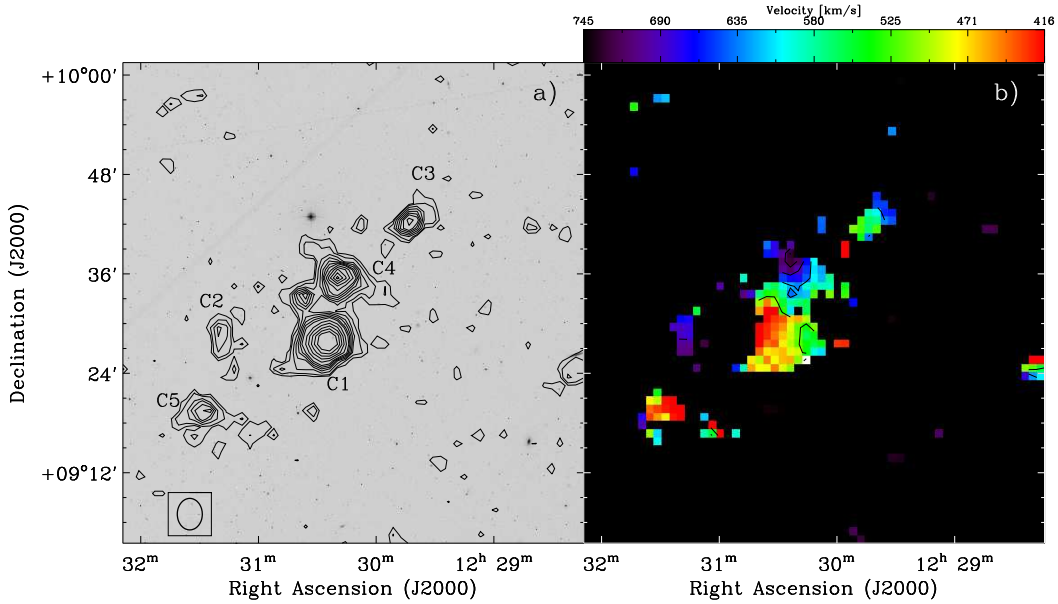

Figure 5.2: Global HI distribution and kinematics of the cloud complex. *a*) One square degree total intensity (zeroth moment) map of the cloud complex field. The HI contours are 50, 100, 200, 300, 400, 500, 600, 800, 1000, 1200, 1400, 1600 mJy km s^{-1} beam^{-1}. The background image is taken from the 2nd generation Digital Sky Survey B-band plates (Lasker et al. 1990). The ellipse in the lower left indicates the ALFALFA beam size (3′.3 × 3′.8). *b*) Intensity-weighted velocity (first moment) map. The linear scale bar ranges from 416-745 km s^{-1}. Contours indicate 450, 500, 550, 600, 650, 700 km s^{-1}.

$M_{HI} = (1.62 \pm 0.04) \times 10^8\ M_\odot$. There is a faint, uncataloged optical feature visible in SDSS images in the vicinity of C1; its relationship to the HI cloud will be discussed in section 5.3.

Cloud C2: This isolated cloud is the faintest ALFALFA detection in the region at $S/N = 6.5$, and it has the lowest HI mass. C2 is close to the ImV dwarf galaxy VCC 1357 (Binggeli et al. 1985), but the ALFALFA centroid is offset from the optical position of the latter by 2′ to the West. An Arecibo single-beam observation centered on VCC 1357 with similar sensitivity to the ALFALFA data is presented by Hoffman et al. (1987). The properties of their detection are identical to those of C2 within the measurement uncertainties; these and the ALFALFA observations have likely uncovered

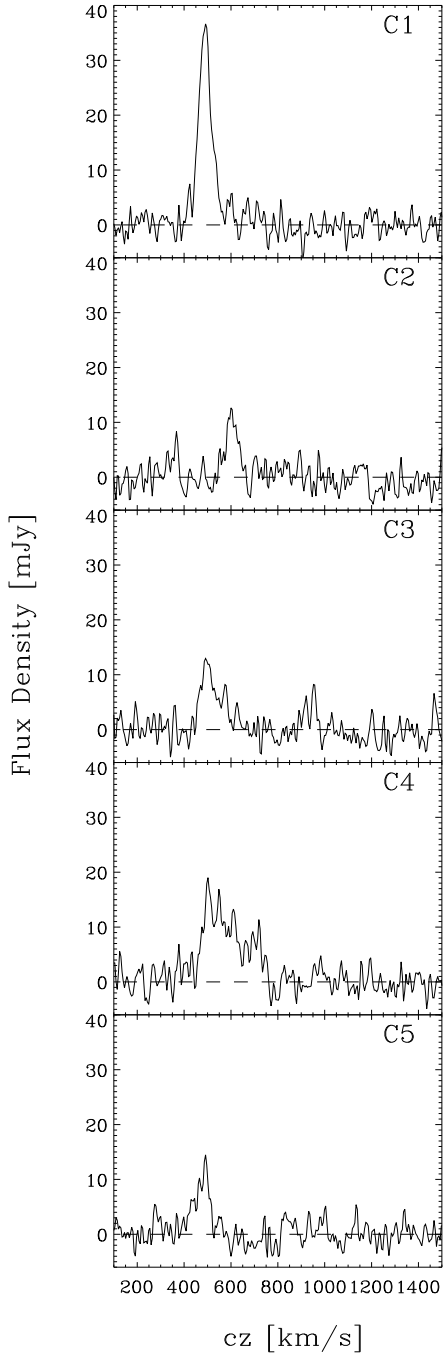

Figure 5.3: Integrated spectral profiles for C1-C5 at a resolution of $\delta V = 5.1$ km s^{-1}. The average RMS across the five spectra is 2.13 mJy/channel.

the same object. However, the previous association of VCC 1357 with this HI source is now muddled by the evidence for an offset in position between the two, and by the detection of the other HI complex clouds presented here. The possible relationship between C2 and VCC 1357 is discussed in section 5.2.

Cloud C3: This northernmost component of the complex is unresolved by the ALFA beam. Its integrated profile appears asymmetric with more emission on the high-velocity side of the peak (Figure 5.3), but this may be an artifact of the poor S/N. A new detection by ALFALFA, C3 is not connected to the main clouds C1 and C4 at the sensitivity obtained. There is no optical counterpart to C3 in the SDSS or DSS survey images of the region.

Cloud C4: This cloud is a new ALFALFA detection that appears to be connected to the main cloud C1, with its centroid located just 6.6′ to the North of the latter (Figure 5.2). Its HI mass is equal to that of C1 with $M_{HI} = (1.66 \pm 0.08) \times 10^8\ M_\odot$, but its integrated profile is almost 200 km s^{-1} broader. The spectrum is asymmetric with more emission on the high-velocity side of the peak (Figure 5.3), and the cloud is resolved into a collection of smaller clumps by the ALFA beam. It therefore seems unlikely that the integrated profile is broadened by coherent rotation. There is no optical counterpart to C4 in the SDSS or DSS survey images of the region.

Cloud C5: This new ALFALFA detection is located 17.4′ Southeast of the main cloud C1. Its integrated profile appears to be symmetric, and implies an HI mass that is a third that of C1 at $M_{HI} = (5.9 \pm 0.4) \times 10^7 M_\odot$. At the ALFALFA sensitivity, C5 is not connected with any other complex clouds. There is no optical counterpart to C5 in the SDSS or DSS survey images of the region.

5.2 The Environment of the Cloud Complex

Followup observations with the Palomar 5-m Hale telescope on the cloud complex have not yielded any spectral signature for redshift measurements. Limits on the mass–to–light ratio can be made by determining surface brightness limits from raw SDSS imaging provided by the Data Access Server. A small, optical feature appears to coincide with C1 and is just above the *g*-band SDSS detection limit. We use the C1 cloud mass M_{HI} = 1.62×10^8 $M_\odot$ from Table 5.1. The computed luminosity and resulting M_{HI}/L ratios are shown as a function of optical size in Figure 5.4. The optical feature near C1 is $\sim$ 10″ across; for this size the *g*–band luminosity is $L_g \sim 10^6$ $L_\odot$. Using the stellar M^*/L^* ratios estimated from *g*–band luminosity functions, this gives a stellar mass–to–light ratio estimate of M^*/L^* ∼1.6 (Bell et al. 2003). If this optical counterpart is associated with C1, the stellar mass is less than 1% of M_{HI} and M_{HI}/L_g >170. An analogous exercise with C2 and possible counterpart VCC 1357 yield a stellar mass to HI mass ratio of less than 0.05. Any association between faint optical features and the HI detections remains ambiguous.

It is useful to analyze the Virgo cluster environment and the clouds' location therein. Figure 5.5 shows the Virgo Cluster X-ray environment in the vicinity of the HI cloud detections (Snowden et al. 1995). The large X–ray hotspots are M49 and M87, with the HI cloud complex indicated with the crossed circles. The density of the ICM in the vicinity of the cloud complex is $\rho_{_{ICM}} = 1.7 \times 10^{-3}$ cm^{-3} (Vollmer et al. 2001). The Virgo cluster temperature map derived by Shibata et al. (2001) gives an ICM temperature of $T_8 = 0.235$ in units of 10^8 K. The nearby SBa galaxy NGC 4424 (also cataloged as UGC 7561 and VCC 9079) is west of the cloud complex, located at $\alpha = 12^{\rm h}27^{\rm m}11.6^{\rm s}, \delta =$ +09°25′14″ (J2000). This places NGC 4424 at a projected distance of 236 kpc from the cloud center, and 900 kpc from M87. This peculiar galaxy is at a velocity ($cz_\odot$ =

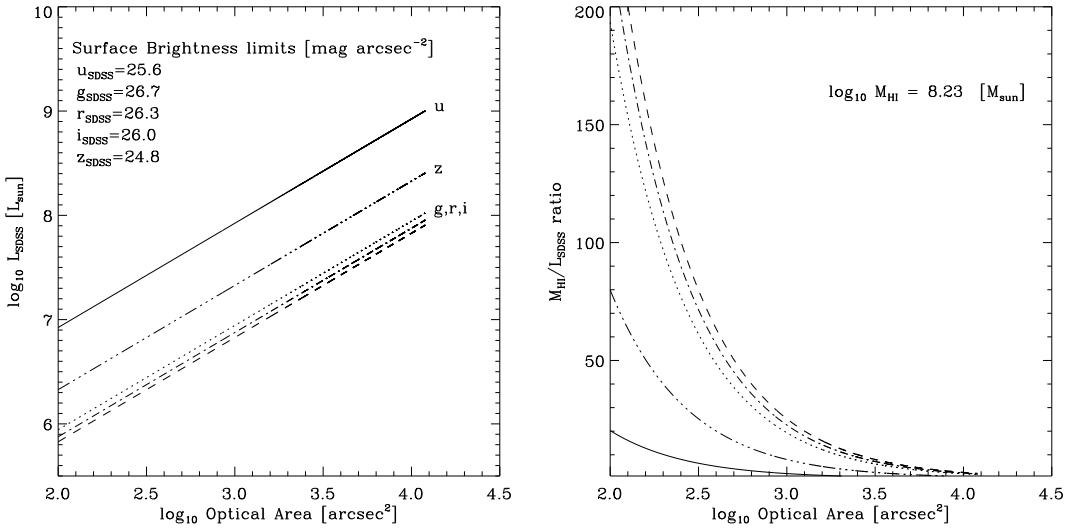

Figure 5.4: Luminosity and M/L ratio limits for 5 SDSS bands based on measured surface brightness limits.

437 km s^{-1}), near that of the main cloud, and has an HI mass of 2.5×10^8 $M_\odot$ in the disk and tail components. Figure 5.7 shows the map of NGC 4424 as created from the ALFALFA data cubes, displaying the one sided tail extending toward the southeast. The tail was originally resolved at higher resolution by Chung et al. (2007), who also showed that the HI disk is truncated at a radius smaller than that of the stellar component of the galaxy. The angular size of the stellar component, $3'.6 \times 1'.8$, translates to a linear size of 17×9 kpc at the Virgo distance. HI deficiency values for NGC 4424 range from 0.75 (Chung et al. 2007) to 1.09 (Helou et al. 1984), indicating that 80% to 90% of its HI gas has been lost. Cortés et al. (2006) characterizes it as having disturbed morphology; they also suggest that CO observations are indicative of non–circular gas motions and discuss the vulnerability of the galaxy to ram pressure stripping (see also Kenney et al. 1996). It is also important to note the southeast to northwest direction of motion for NGC 4424 as exhibited by the tail; this motion is not compatible with the position of the cloud complex.

Edge on spiral NGC 4445 (type Sab) is the closest galaxy both spatially and in veloc-

ity to the HI cloud complex, and is located at $\alpha = 12^h28^m15.9^s, \delta = +09°26'11''$ (2000). Its heliocentric radial velocity is $cz_\odot = 354$ km s^{-1} and the HI mass 5.5×10^7 $M_\odot$ (Kent et al. 2008). Solanes et al. (2002) estimate its HI deficiency between 0.98 and 1.11, i.e. NGC 4445 has lost about between 90% and 93% of its HI gas. with a major axis angular diameter of 2′.6, its linear size is about 13 kpc. We are not aware of HI synthesis data of this object; none are found in the VLA data archive.

Under the assumption that the clouds originated in the disk of a galaxy moving at high speed through the cluster, the velocity vector of the clouds in the cluster reference frame has a net component towards us, as the heliocentric velocity of the clouds is several hundred km s^{-1} lower than the systemic velocity of the cluster of 1150 km s^{-1} (Huchra 1988). NGC 4424 and NGC 4445 are relevant to the cloud complex due to their spatial and velocity proximity. A parent galaxy to the cloud complex should have a velocity measurement even lower than that of the gas clouds, and NGC 4424 and NGC 4445 satisfy that criteria. Figure 5.6 shows all cataloged objects within 1° of C1 and with heliocentric velocities between 100 and 900 km s^{-1}. Galaxies detected in the 21cm line are plotted with a circle of area proportional to the HI mass. Galaxies not detected in ALFALFA with redshift information from other sources are plotted with crosses. It is assumed that all galaxies are located at the distance of the Virgo cluster. NGC 4424, NGC 4445, and NGC 4451 are labeled for reference.

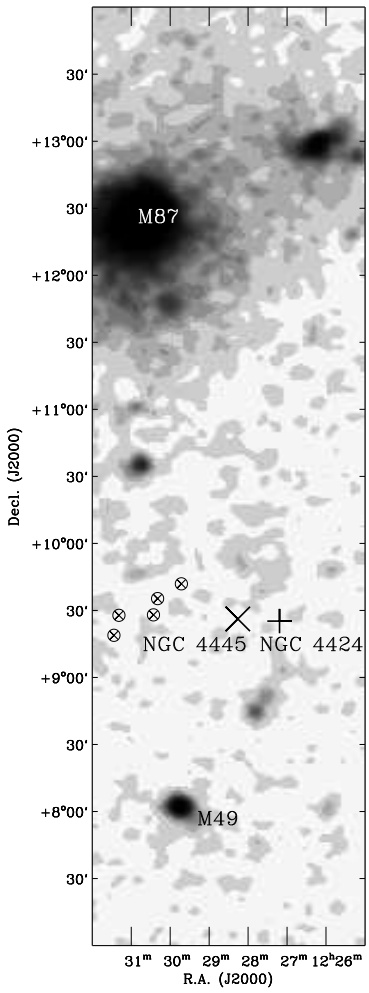

Figure 5.5: The environment of the HI cloud complex within the greater cluster area. The crossed circles indicate the five components of the complex discussed in this paper. The large plus (+) indicates the position of SBa galaxy NGC 4424 ($cz_{\odot}$ = 476 km s^{-1}). The large X indicates the position of Sab galaxy NGC 4445 ($cz_{\odot}$ = 354 km s^{-1}. The X-ray peaks are labeled indicating Virgo cluster galaxies M49 and M87 (Snowden et al. 1995). The symbols are not indicative of source sizes and are shown only for positional indication.

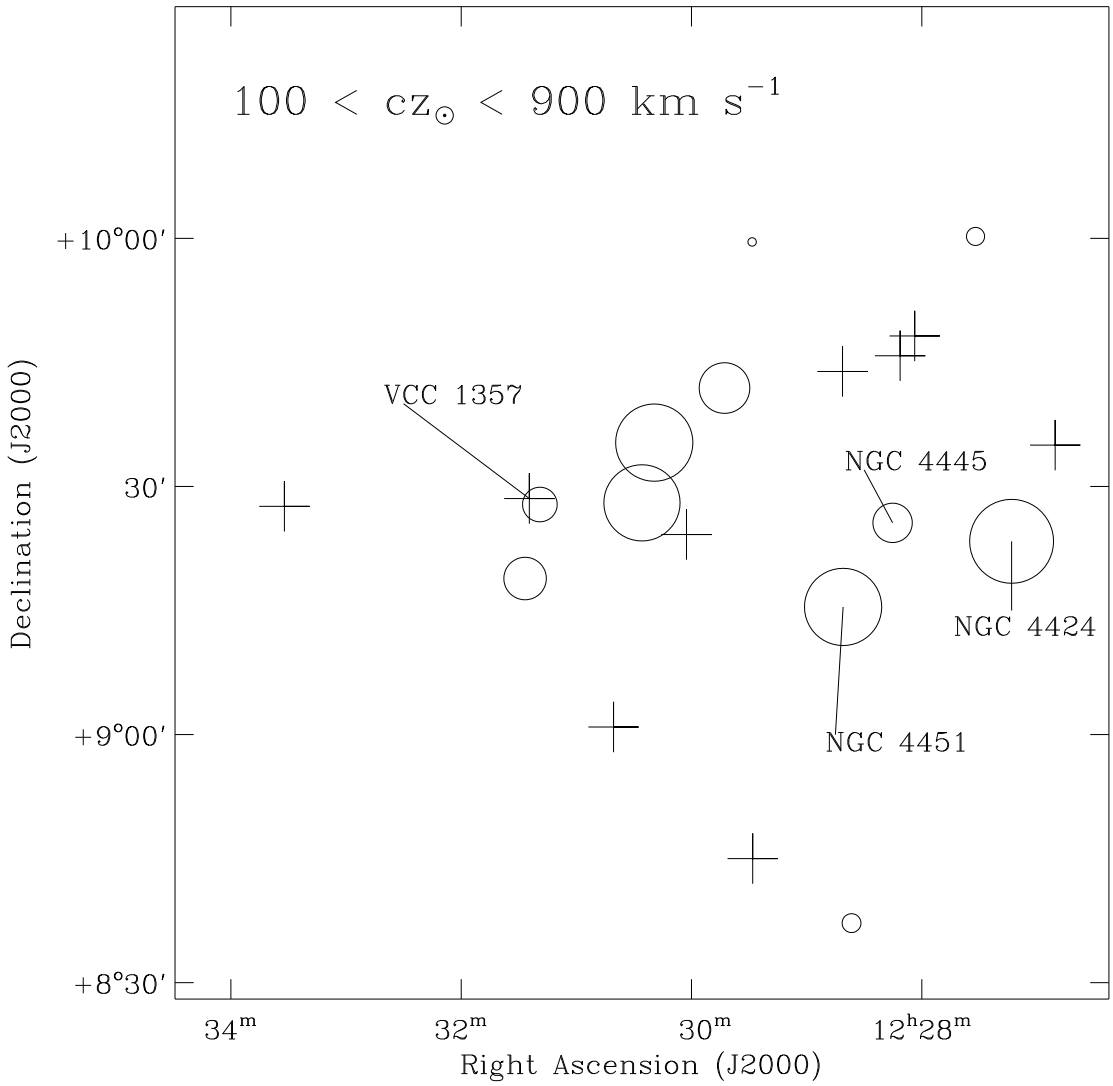

Figure 5.6: Galaxies in the vicinity of the cloud complex. The plot shows all objects with $100 < cz_{\odot} < 900$ km s^{-1} and within 1° of C1 listed in the Arecibo General Catalog. The crosses indicate objects without HI measurements from the ALFALFA survey. Objects with HI masses as measured from ALFALFA are shown as circles, with the circle size indicative of the HI mass. The smallest circle indicates $\log_{10}(M_{HI}/M_{\odot})$=7.30 and the largest circle indicates $\log_{10}(M_{HI}/M_{\odot})$=8.28. Galaxies pertaining to the possible origin of the HI cloud complex are labeled for reference.

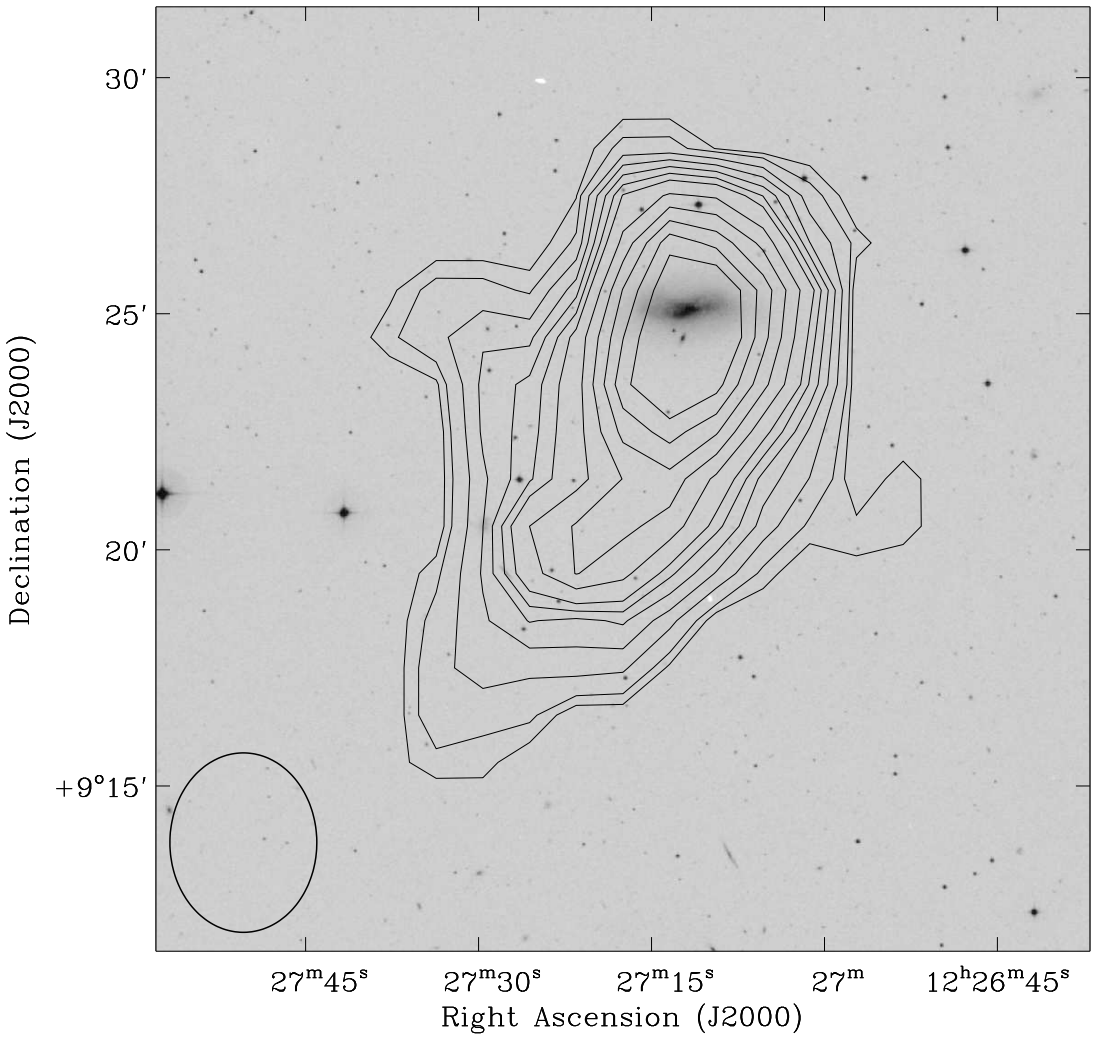

Figure 5.7: ALFALFA map of NGC 4424 ($cz_\odot$ = 476 km s^{-1}), showing the HI tail extending to the southeast. The total intensity map shows emission integrated over the velocity range 367 ≤ $cz_\odot$ ≤ 517 km s^{-1}. The contour levels indicate 50, 100, 200, 300, 400, 500, 600, 800, 1000, 1200, 1400, and 1600 mJy km s^{-1} beam^{-1}. The ellipse in the lower left shows the size of the ALFALFA beam (3′.3 × 3′.8).

5.3 Discussion

5.3.1 A Gravitationally Stable Cloud?

We can consider multiple physical scenarios and timing arguments based on the known physical parameters of the cloud complex and its location in the cluster. The first analysis examines the cloud as an isolated entity. The lack of a visible optical counterpart could be attributed to the shallowness of available optical online databases. If the individual cloud components are gravitationally bound objects embedded in their own dark matter halos, their total dynamical masses can be computed (assuming spherical symmetry for a self-gravitating cloud) via

$$\frac{M_{dyn}}{M_{\odot}} = (3.39 \times 10^4)\, a_{HI}\, D_V \left(\frac{W_{50}}{2}\right)^2 \tag{5.2}$$

where a_{HI} is the object diameter in arcminutes, W_{50} is the velocity width in km s^{-1} and the Virgo distance D_V is in Mpc.

The dynamical masses are 2.3×10^9 $M_{\odot}$ for C1 and 0.3×10^9 $M_{\odot}$ for C2 as calculated from the aperture synthesis measurements listed in Table 5.2. The density of such objects would be 1.4×10^{-25} g cm^{-3} for C1 and 1.0×10^{-25} g cm^{-3} for C2. These densities can be compared to the critical density, $\rho_{crit} = \left(1.9 \times 10^{-29} \text{ g cm}^{-3}\right) h^2$, where $h = 0.7$. Under the same physical assumptions, the total dynamical mass of the whole cloud complex would be 10^{11} $M_{\odot}$ and the mean density 2.1×10^{-27} g cm^{-3}. The VLA data do not show any trace of ordered motions for the gas measurements of C1 or C2. The Arecibo data show no ordered motions for the entire complex or any degree of central concentration. If the dark matter provided the gravitational binding and extended beyond the measured baryonic component, C1 would exceed 10^{10} $M_{\odot}$, and we would expect to see traces of ordered motion and a central mass concentration. Based on this interpretation

of the observations, it is unlikely that the HI cloud complex is a group of optically dark galaxies embedded in their own dark matter halos.

5.3.2 Interactions with the Cluster Environment

The large HI tail originating from NGC 4254 was presented in Chapter 4 (Kent et al. 2007; Haynes et al. 2007). The subsequent analysis by Duc & Bournaud (2008) modeled the formation of the tail as the result of gas-rich galaxy in a high speed collision in a cluster environment such as Virgo. As a results of these studies, the second analysis examines gas removal by ram pressure and a high speed tidal interaction.

The HI cloud complex does not exhibit the stream-like topology expected in a gravitational encounter. More total HI gas is seen in either of the galaxies NGC 4424 or NGC 4445. If the cloud complex origin lies with NGC 4424 or NGC 4445, the damage would have been quite significant in terms of gas loss. This is contradictory to the evidence that high speed galaxy-galaxy encounters produce relatively small damage of gas loss by the victim with large tails in spatial extent (Duc & Bournaud 2008).

Chung et al. (2007) reports ram pressure effects in the range between $125 < n_{ICM} v_{gal}^2 < 175$ cm^{-3} (km s^{-1})^2, and a restoring force range between $40 < \Sigma_{ISM} V_{rot}^2 / R_{gal} < 475$ cm^{-3} (km s^{-1})^2 for the location of NGC 4424, where n_{ICM} is the particle number density of the intracluster medium (ICM), v_{gal} is the object's velocity with respect to the ICM, Σ_{ISM} is the interstellar medium (ISM) surface density, and V_{rot} is the object's rotational velocity at a radius R_{gal}. Ram pressure stripping will occur when the ram pressure exceeds the gravitational restoring force; $\rho_{ICM} v_{gal}^2 \geq \Sigma_{ISM} V_{rot}^2 / R_{gal}$, with $\rho_{ICM} = m_p n_{ICM}$, where m_p is the mass of the proton and n_{ICM} is defined as above. We can write this

condition in the form

$$n_{ICM} m_p v_{gal,3d}^2 \geq 2\pi G \Sigma_{ISM} \Sigma_d \tag{5.3}$$

where Σ_{ISM} is the gas surface density of the galactic disk, Σ_d is the total surface mass density of the disk, and $v_{gal,3d}$ is the the velocity of the galaxy with respect to the intra-cluster medium. Substituting for the surface densities we can write (in cgs units)

$$n_{ICM} m_p v_{gal,3d}^2 \geq 2\pi G \, \frac{M_{ISM}}{\pi R_{gal}^2} \, \frac{M_d}{\pi R_{gal}^2} \tag{5.4}$$

where M_{ISM} and M_d are the gas and total disk masses respectively. Here we assume a cross sectional area for the disk. Combining constants and converting to more convenient astronomical units, we can write

$$n_{ICM} v_{gal,3d}^2 \geq 1.1 \times 10^{-14} \, \frac{M_{ISM} M_d}{R^4} \tag{5.5}$$

where density values are in cm^{-3}, velocities are in km s^{-1}, masses are in $M_\odot$, and radii are in kpc. Finally, we can parameterize this condition as in (Sarazin 1986), written as

$$\Big(\frac{n_{ICM}}{10^{-3}\,\mathrm{cm}^{-3}}\Big)\Big(\frac{v_{gal,3d}}{10^3\,\mathrm{km\ s}^{-1}}\Big)^2 \geq 11\Big(\frac{M_d}{10^{11} M_\odot}\Big)^2\Big(\frac{R_{gal}}{10\,\mathrm{kpc}}\Big)^{-4}\Big(\frac{M_{ism}}{0.1 M_d}\Big) \tag{5.6}$$

One final consideration takes into account the angle θ between the line of sight and the galaxy velocity vector. The relation between the galaxy's total scalar velocity and the velocity as defined in Equation 5.6 will be $v_{gal,3d} \simeq v_{tot}/\cos\theta$ km s^{-1}. We can now consider scenarios for both NGC 4424 and NGC 4445 under these physical conditions based on the observations.

For NGC 4424, $v_{gal,3d} \simeq 700/\cos\theta$ km s^{-1}, $M_d \simeq 10^{10}\ M_\odot$ within a radius $R_{gal} \simeq 10$ kpc. We note that this is a generous estimate for the mass, since the total velocity width of the HI emission of the galaxy is 61 km s^{-1} (Kent et al. 2007) and the inclination of the disk, albeit unknown, is unlikely to be smaller than 45°. We also assume $n_{ICM} = 1.7 \times$

10^{-3} cm^{-3} and $M_{ISM}/0.1M_d \sim 1$. With those numbers, the ram pressure term exceeds comfortably the restoring force at the larger galactocentric radii, even for geometries for which the average n_{ICM} encountered by the galaxy is significantly lower than the assumed value of 1.7×10^{-3} cm^{-3}. These values agree with the assessment by Chung et al. (2007).

The case for NGC 4445 requires more assumptions. Due to lack of aperture synthesis measurements, we don't know the radial extent of the HI disk in that galaxy. We use $v_{gal,3d} \simeq 800/\cos\theta$ km s^{-1}, and $R_{gal} \simeq 6$ kpc and estimate its disk mass from a rotational velocity of 107 km s^{-1}, from the measured velocity full width of the HI line of 213 km s^{-1}. The estimate of the ram pressure exceeds the restoring force at the galactocentric radii at which most of the HI would be expected to be found in an unperturbed disk.

5.3.3 Tidal Effects and Timing Computations

Simple Tidal Effects

An estimate of dynamical effects on two nearby clouds in the vicinity of a cluster potential can be determined via a simple calculation. Figure 5.8 shows a simple scheme for two such clouds near a cluster. Two clouds will disperse at a rate $\Delta v = g\Delta t$ under gravitational tidal acceleration g from the cluster potential, where g is

$$g = \frac{2GM_{cluster}x}{R^3_{cluster}} \tag{5.7}$$

and $M_{cluster}$ is the mass of the cluster within radius $R_{cluster}$, and x is the initial separation of the two clouds. The timescale of the encounter can be taken as $\Delta t \sim R_{cluster}/v_{c,3d}$, where $v_{c,3d} = v_c/\cos\theta$ is the velocity of the cloud complex with respect to the cluster.

Taking $\Delta v = g\Delta t$, we can write a simple relation for the separation rate of the two clouds

$$\Delta v \approx \frac{2GM_{cluster}x}{R_{cluster}^2 v_{c,3d}} \tag{5.8}$$

For two small clumps separated by a displacement 10 kpc, located 845 kpc from the cluster core of mass 10^{14} $M_\odot$ at a velocity of 600/cos θ km s^{-1} with respect to the cluster, the clouds would separate at a rate Δv ~24 kpc Gyr^{-1}, and would roughly double their separation in a time comparable with the cluster crossing time scale $\sim R_{cluster}/v_{c,3d}$. As neutral gas can be observed for well after a tidal encounter, it is possible that this cloud has been torn within the past 10^8 years. Tidal forces related to the cluster potential alone are unlikely to account for the spatial dispersion of the clouds in the complex, if they were stripped from a single galaxy.

Timing Effects and Ram Pressure Acceleration

A timing argument using for the separation rate between the cloud complex and a nearby galaxy can be approximated by

$$\Delta t_{sep} \sim \frac{\Delta r}{\Delta v} = \left(\frac{\Delta r_{proj}}{\sin\theta}\right)\left(\frac{\Delta v_{proj}}{\cos\theta}\right)^{-1} = \left(\frac{\Delta r_{proj}}{\Delta v_{proj}}\right)\arctan\theta \ \text{[Gyr]} \tag{5.9}$$

where Δr is in units of kpc and Δv is in units of km s^{-1}. For the galaxies NGC 4424 and NGC 4445 we compute

$$\Delta t_{sep,4424} \sim \frac{235 \text{ kpc}}{100 \text{ km s}^{-1}} \arctan\theta = 2.3 \arctan\theta \ \text{Gyr} \tag{5.10}$$

$$\Delta t_{sep,4445} \sim \frac{150 \text{ kpc}}{200 \text{ km s}^{-1}} \arctan\theta = 0.75 \arctan\theta \ \text{Gyr} \tag{5.11}$$

These values are comparable with cluster crossing timescales $\sim R_{cluster}/v_{c,3d}$ for large values of θ. However, as the clouds move through the cluster, the acceleration due to ram pressure is not a constant. If one were to assume constant acceleration, then the separation times for the velocity (Δt_v) and spatial scales (Δt_r) would need to be

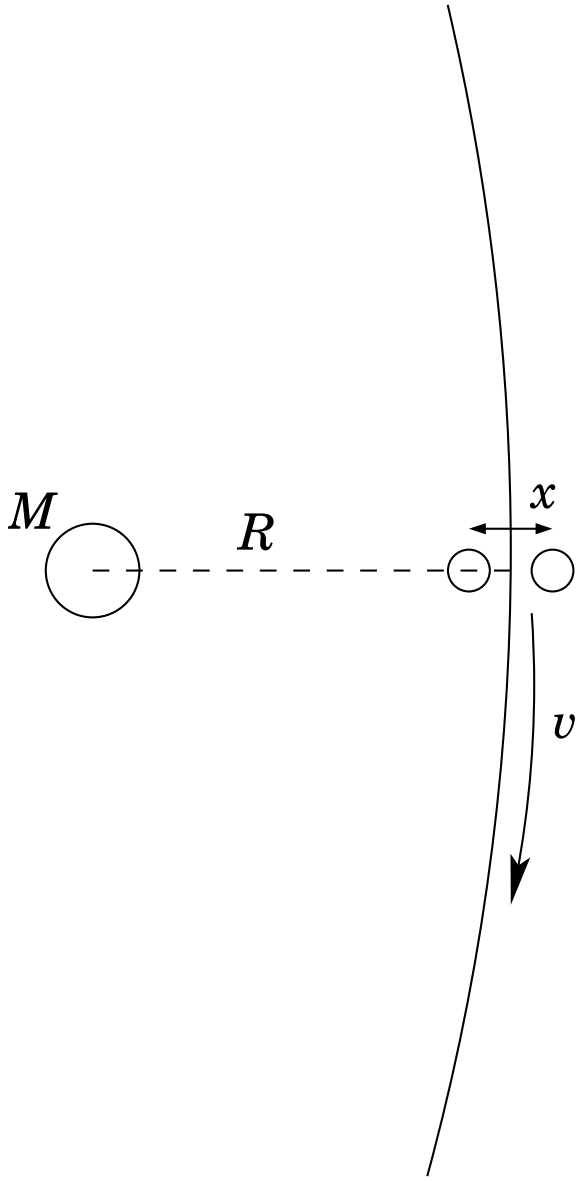

Figure 5.8: Schematic of an encounter of two clouds in a cluster. The clouds are separated by a distance x. The cloud complex model is located a distance R from the cluster core of mass M, moving at a velocity v relative to the cluster.

$\sim 2\Delta t_{sep}$. Therefore, the next step is to derive this effect of moving through the cluster environment.

The force on the cloud can be written as the ram pressure times the cross sectional area, given by (Gunn & Gott 1972; Vollmer et al. 2001)

$$F = P \times A = \left(n_{_{ICM}} m_p v_{c,3d}^2\right)\left(\pi r_c^2\right) \tag{5.12}$$

where the variables are notated as above, m_p is the mass of the proton, and $v_{c,3d} = v_c/\cos\theta$ and r_c are the velocity through the ICM and radius of the cloud respectively.

The acceleration can be computed simply by

$$a = \frac{\Delta v}{\Delta t} = \frac{F}{M_{HI}} = \frac{n_{_{ICM}} m_p v_{c,3d}^2 \pi r_c^2 \eta}{M_{HI}} \tag{5.13}$$

where η accounts for fractional gas species other than neutral hydrogen, and M_{HI} is the HI mass of the cloud. This expression for the acceleration can be parameterized as

$$a = 2.5 \times 10^{-9} \eta \left(\frac{n_{_{ICM}}}{10^{-3}\ \mathrm{cm^{-3}}}\right)\left(\frac{r_c}{\mathrm{kpc}}\right)^2 \left(\frac{v_{c,3d}}{1000\ \mathrm{km\ s^{-1}}}\right)^2 \left(\frac{M_{HI}}{10^8\ M_\odot}\right)^{-1} \ [\mathrm{cm\ s^{-2}}] \tag{5.14}$$

From this expression we can account for acceleration effects on the cloud that will cause separations in both velocity and spatial scales. The accumulation of these effects will occur on time scales Δt_v for velocity and Δt_r for spatial scales by combining equations 5.9 and 5.14, giving

$$\Delta t_v \approx \frac{\Delta v}{a} = 1.26 \times 10^6\ \eta^{-1} \left(\frac{\Delta v_{proj}/\cos\theta}{\mathrm{kpc}}\right)\left(\frac{n_{_{ICM}}}{10^{-3}\ \mathrm{cm^{-3}}}\right)^{-1} \times \left(\frac{v_c/\cos\theta}{1000\ \mathrm{km\ s^{-1}}}\right)^{-2} \left(\frac{r_c}{\mathrm{kpc}}\right)^{-2} \left(\frac{M_{HI}}{10^8\ M_\odot}\right) \ [\mathrm{yrs}] \tag{5.15}$$

$$\Delta t_r \approx \left(\frac{2\Delta r}{a}\right)^{1/2} = 4.98 \times 10^7\ \eta^{-1/2} \left(\frac{\Delta r_{proj}/\sin\theta}{\mathrm{kpc}}\right)^{1/2} \left(\frac{n_{_{ICM}}}{10^{-3}\ \mathrm{cm^{-3}}}\right)^{-1/2} \times \left(\frac{v_c/\cos\theta}{1000\ \mathrm{km\ s^{-1}}}\right)^{-1} \left(\frac{r_c}{\mathrm{kpc}}\right)^{-1} \left(\frac{M_{HI}}{10^8\ M_\odot}\right)^{1/2} \ [\mathrm{yrs}] \tag{5.16}$$

We assume an HI mass for cloud C1 of $M_{HI} = 1.6 \times 10^8\ M_\odot$. The other values that have been used in this section pertaining to NGC 4424 and NGC 4445 are summarized in Table 5.3.

Table 5.3: Timescale Relation Parameters

Galaxy	v_c (km s^{-1})	Δv_{proj} (km s^{-1})	Δr_{proj} (kpc)	$2\ \Delta t_{sep}$
(Gyr) (1)	(2)	(3)	(4)	(5)
NGC 4424	700	100	235	4.6 arctan θ
NGC 4445	800	200	150	1.5 arctan θ

For the condition outlined at the beginning of this section, where $\Delta t_v \simeq \Delta t_r \simeq 2\Delta t_{sep}$, we can equate these two timescales and arrive at the expression

$$\eta^{1/2} \left(\frac{n_{ICM}}{10^{-3}\ \mathrm{cm}^{-3}} \right)^{1/2} \left(\frac{r_c}{\mathrm{kpc}} \right) \sin^{-1/2}\theta = \begin{cases} 0.30 & \text{for NGC 4424} \\ 0.67 & \text{for NGC 4445} \end{cases} \tag{5.17}$$

using the values in Table 5.3. Also shown in the table are the values for twice the separation timescale. Clearly the value for NGC 4424 indicates that a large amount of time has passed since the gas removal occurred. A large angle of θ (perpendicular to the line of sight) would be required if the galaxy was moving at high speed. In contrast, if NGC 4445 is moving at high speed (~1500 km s^{-1}) at an intermediate angle ($\theta \sim 40°$-60°), we arrive at a time scale of ~1 Gyr. The 150 km s^{-1} velocity dispersion of the cloud complex is accounted for by size differences and thermal make up of the clouds.

The measured radius for HI emission of C1 in Table 5.2 is 1′.35, or 6.5 kpc at the Virgo distance. Equation 5.17 can give an effective radius for values of $\eta \sim 0.4$–0.7 and average number density values of $\bar{n}_{icm} \sim 0.5$–1×10^{-3} cm^{-3}, the effective cloud radius is of order 1 kpc. The surviving material is in the denser regions of the cloud complex, whereas neutral gas in the warm neutral medium is easily stripped. The filling factor in the cold neutral medium phase is thought to be a few percent at most.

Cloud Gas Loss through Evaporation

After removal from the galaxy, the cold gas is heated by conduction by the intracluster gas and the gas mass of the cloud is progressively reduced by evaporation. Presumably there are no stars associated with the cloud, and therefore no stellar mass loss is able to replenish the lost gas. The evaporation rate in $M_\odot$ yr^{-1} can be written as (Cowie & McKee 1977; Cowie & Songaila 1977; Sarazin 1986)

$$\dot{M}_{ev} \simeq 16\pi\mu m_p \kappa r_{kpc}/25k \simeq 35 \left(\frac{T}{10^8 \text{ K}}\right)^{5/2} \left(\frac{r}{\text{kpc}}\right) \left(\frac{40}{\ln\Lambda}\right) \quad [M_\odot \text{ yr}^{-1}] \qquad (5.18)$$

where μ is the mean molecular weight, m_p the proton mass, κ the thermal conductivity, T the intracluster gas temperature in units of K, r_{kpc} the effective cloud radius in kpc (proportional to the square root of the area of the cloud exposed to the ICM), k the Boltzmann constant and Λ the Coulomb logarithm. This rate is approximately valid in the cluster core. A couple of cluster core radii ($\sim$ 500 kpc) out from the center of the ICM distribution, however, conduction becomes significantly less effective (Sarazin 1986). Using a value of $T_8 = 0.235$ (Shibata *et al.* 2001) and a Coulomb logarithm of $40/\ln\Lambda \sim 1$, the evaporation timescale is

$$t_{ev} = \frac{M_{gas}}{\dot{M}_{ev}} = \frac{M_{HI}}{\eta\psi}\left(35 \left(\frac{T}{10^8 \text{ K}}\right)^{5/2} \left(\frac{r}{\text{kpc}}\right) \left(\frac{40}{\ln\Lambda}\right)\right)^{-1} \geq 1.7\times10^8 r_{kpc}^{-1} \eta^{-1}\psi^{-1} \text{ [yr]}. \qquad (5.19)$$

In this equation $\psi \leq 1$ is a correction factor that is roughly proportional to the fraction of the time the cloud's orbit that will place it in part of the ICM where the conductivity coefficient κ yields the evaporation rate in equation 5.18. This fraction takes place in the time between gas removal from the parent galaxy and the current epoch. Again using the C1 radius of 6.5 kpc and accounting for helium with $\eta \sim 1.4$, we find an evaporation timescale of $t_{ev} \sim 18\psi^{-1}$ Myr. Other factors that can contribute include the cloud geometry, its orbit trajectory and varying ICM density along that path, the fraction of gas in ionized form and magnetic fields, which would inhibit conduction

across field lines. Examining t_{ev} with the effective radius of $\sim$ 1 kpc obtained in the previous section with a smaller value $\eta \sim 0.5$, gives an estimate of $t_{ev} \sim 340\psi^{-1}$ Myr. If the fractional time of the cloud's orbit ψ is small, an evaporation time scale of order 1 Gyr is possible. With suitable physical conditions at the cloud's location in the cluster, it is reasonable to assume that the observed HI is a ram pressure stripped debris field with clumps of partly ionized gas of low volume filling factor. This ionized gas could be rapidly heated, and the denser HI cores would be largely unaffected.

CHAPTER 6

THE VIRGO ENVIRONMENT

6.1 Introduction

The Arecibo Legacy Fast ALFA survey is able to detect HI masses down to $\sim 2 \times 10^7\ M_\odot$ at the Virgo distance (D_{Virgo} = 16.7 Mpc; Mei et al. 2007). The velocity dispersion of the various morphological populations is as high as ~800 km s^{-1}. Due to the large gravitational potential of the cluster, galaxies in the outlying periphery can move at extremely high velocities with respective to cluster systemic velocity. As a result, the redshift measurement is not a reliable indicator of distance for anything in the projected Virgo vicinity on the sky. Galaxies with HI determined redshifts in the range -500 < $cz_\odot$ < 3000 km s^{-1} could be part of the Virgo cluster population. At the same time, galaxies with large infall velocities can be confused with a) legitimate galaxies that lie in the background at distances that are twice Virgo's and b) galaxies that are more nearby and lie in the foreground of the cluster.

Figure 6.1 shows the ALFALFA detections in the range $cz_\odot \leq$ 3000 km s^{-1} for the canonical Virgo boundaries defined by Binggeli et al. (1987). Distances can be assigned to the HI detections via a mass flow model (Tonry et al. 2000; Masters et al. 2004). All galaxies assigned to the Virgo distance are displayed in Figure 6.2. In both Figures 6.1 and 6.2 the detections are plotted with the radius of the circular symbols being proportional to $\log_{10}(M_{HI})$. Much of the HI mass is concentrated in the outer periphery of the cluster, especially toward the western side. Figure 6.3 clearly shows the separation of the background M and W clouds in the NW and SW periphery of the Virgo cluster.

In this chapter, we describe two preliminary studies in an effort to understand the Virgo environment, a simple determination of the HI mass function, and a N-body/SPH (smoothed particle hydrodynamics) simulation of a disk galaxy in a cluster potential.

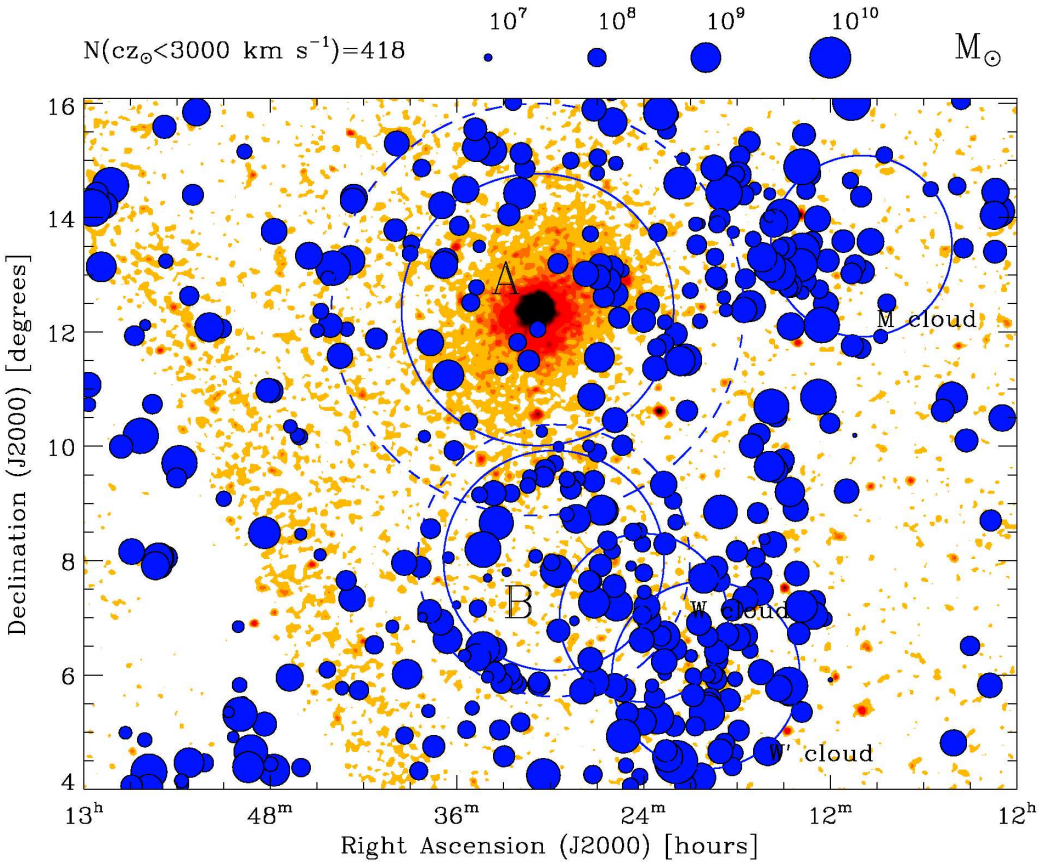

Figure 6.1: Sky distribution of the ALFALFA HI detections with $cz_{\odot} \leq 3000$ km s^{-1}. The radius of the circular symbols is proportional to $\log_{10}(M_{HI})$. The orange background is a hard X-ray counts image from ROSAT (Snowden et al. 1995), smoothed with a 5′ Gaussian kernel. The solid circles outline the boundaries of the A, B, M, W, and W′ areas defined by Binggeli et al. (1987). The dashed lines indicate the virial radius of the dark matter halo $r_{200}/2$ determined by McLaughlin (1999), for the A and B areas centered around cluster members M87 and M49 respectively.

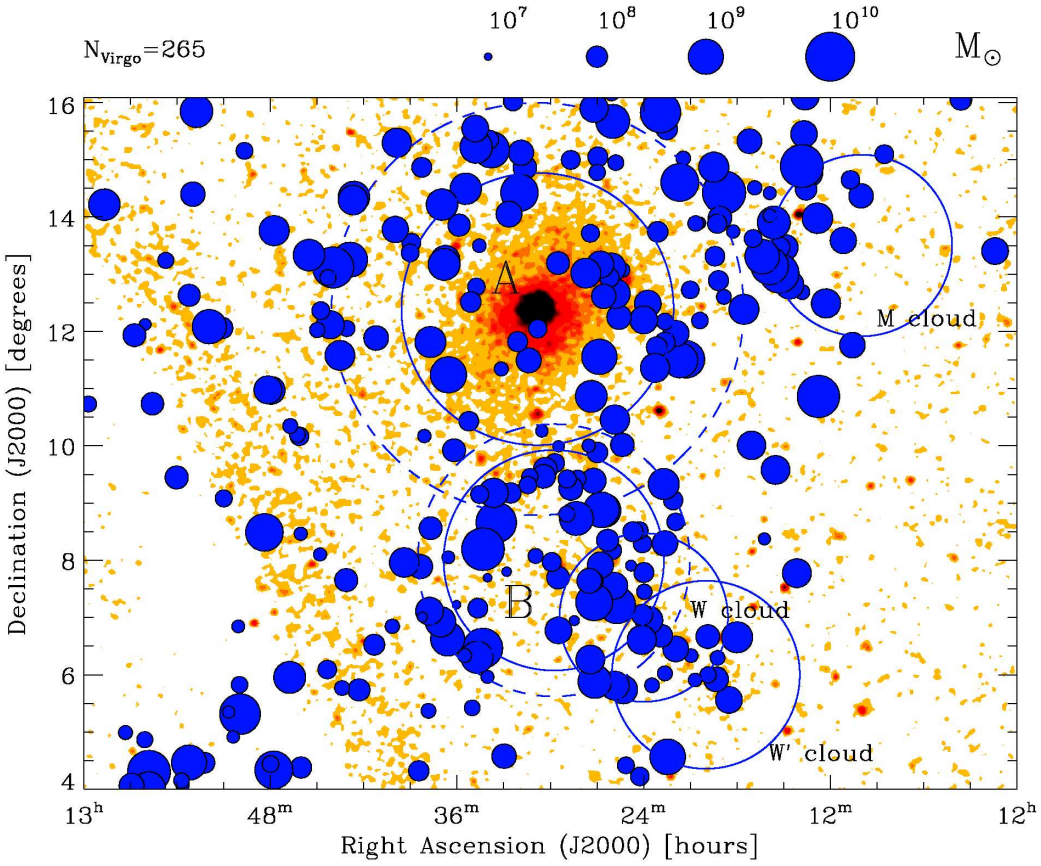

Figure 6.2: Sky distribution of the ALFALFA HI detections with Virgo cluster membership assigned by a mass flow model (Tonry et al. 2000; Masters et al. 2004). The radius of the circular symbols is proportional to $\log_{10}(M_{HI})$. The orange background is a hard X-ray counts image from ROSAT (Snowden et al. 1995), smoothed with a 5′ Gaussian kernel. The solid circles outline the boundaries of the A, B, M, W, and W′ areas defined by Binggeli et al. (1987). The dashed lines indicate the virial radius of the dark matter halo $r_{200}/2$ determined by McLaughlin (1999), for the A and B areas centered around cluster members M87 and M49 respectively.

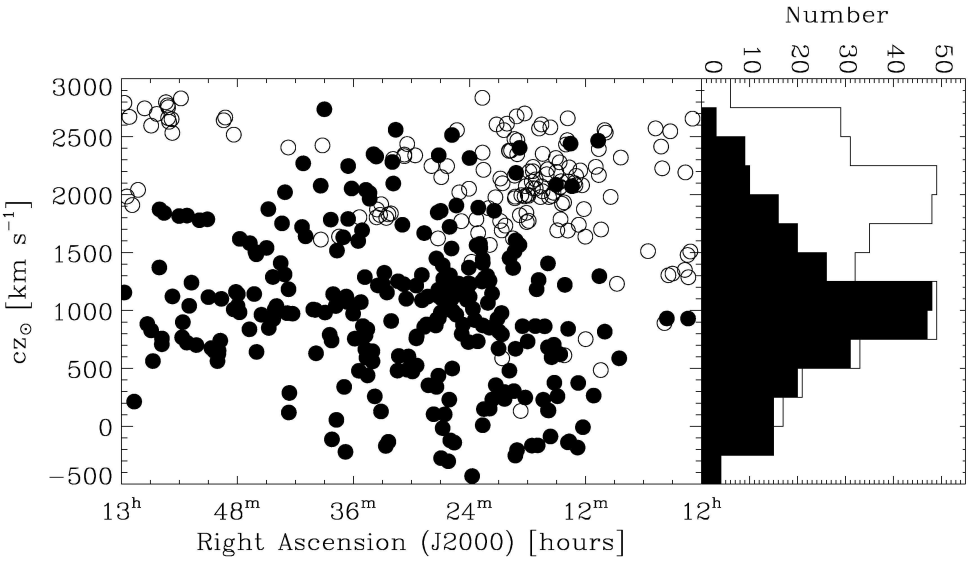

Figure 6.3: $cz_\odot$ versus right ascension for ALFALFA galaxies between 12^h < R.A.(J2000) < 13^h. All circles represent detections for $cz_\odot \leq 3000$ km s^{-1}. Solid circles represent galaxies with Virgo cluster membership assigned by a mass flow model (Tonry et al. 2000; Masters et al. 2004). Therefore unfilled circles show galaxies that are likely to lie behind the Virgo cluster in one of the subclouds shown in Figures 6.1 and 6.2. The unfilled histogram at right shows the *cz* distribution for *all* detections in the plot. The filled histogram shows detections assigned only to Virgo.

6.2 The HI Mass Function

It is important to understand the space density of HI-bearing structures, especially in terms of their galaxy environment. Briggs (1990) published a comprehensive study comparing the mass sensitivity limits of various targeted HI surveys. The HI Mass Function (HIMF) gives the spatial density of galaxies as a function of mass decade, in units of objects Mpc^{-3} dex^{-1}.

The Schechter function (Schechter 1976) is typically used as a non-linear analytical fit to the HIMF, given by

$$\phi(M_{HI}) = \frac{dN}{d\,\log(M_{HI})} = \ln(10)\phi_* \left(\frac{M_{HI}}{M_*}\right)^{\alpha+1} \exp\left(-\frac{M_{HI}}{M_*}\right) \qquad (6.1)$$

In this formulation, α represents the low-mass slope, M_* the "knee" turn in the function,

and ϕ_* the vertical offset.

6.2.1 Computing the HI Mass Function

Galaxies from the ALFALFA catalog are usually assigned a distance based on pure Hubble flow ($D = cz_\odot/H_0$). Distance errors from peculiar velocities are only 10% of the systemic velocity beyond $cz_\odot \sim 6000$ km s^{-1}, which is comparable with the best Tully–Fisher results. For galaxies at $cz_\odot \lesssim 6000$ km s^{-1} that do not have primary distance indicators, a flow model is employed to determine distances (Tonry et al. 2000; Masters et al. 2004). Due to group assignments, including those "assigned" to Virgo, many galaxies in the Virgo vicinity and at $cz_\odot \leq 3000$ km s^{-1} are assigned a distance of ~16 Mpc.

The HI mass function typically utilizes the $\Sigma(1/V_{max})$ method, first developed and used by Schmidt (1968) for studying the spatial and luminosity distributions of quasars. The method has been employed in recent HI mass function studies (Zwaan et al. 1997, 2003, 2005; Rosenberg & Schneider 2002; Springob et al. 2005a). For the Virgo determination, the resulting HIMF is the simply the mass distribution divided by a constant value – that of the maximum volume enclosed by the distance out to the Virgo cluster. The Virgo HIMF is shown in Figure 6.4. The most important result of this figure is that there are no galaxies in the sample having $M_{HI} > 10^{9.75}\ M_\odot$. This is likely the result of gas removal from disk galaxies by ram pressure stripping. Further corrections will account for the velocity width distribution.

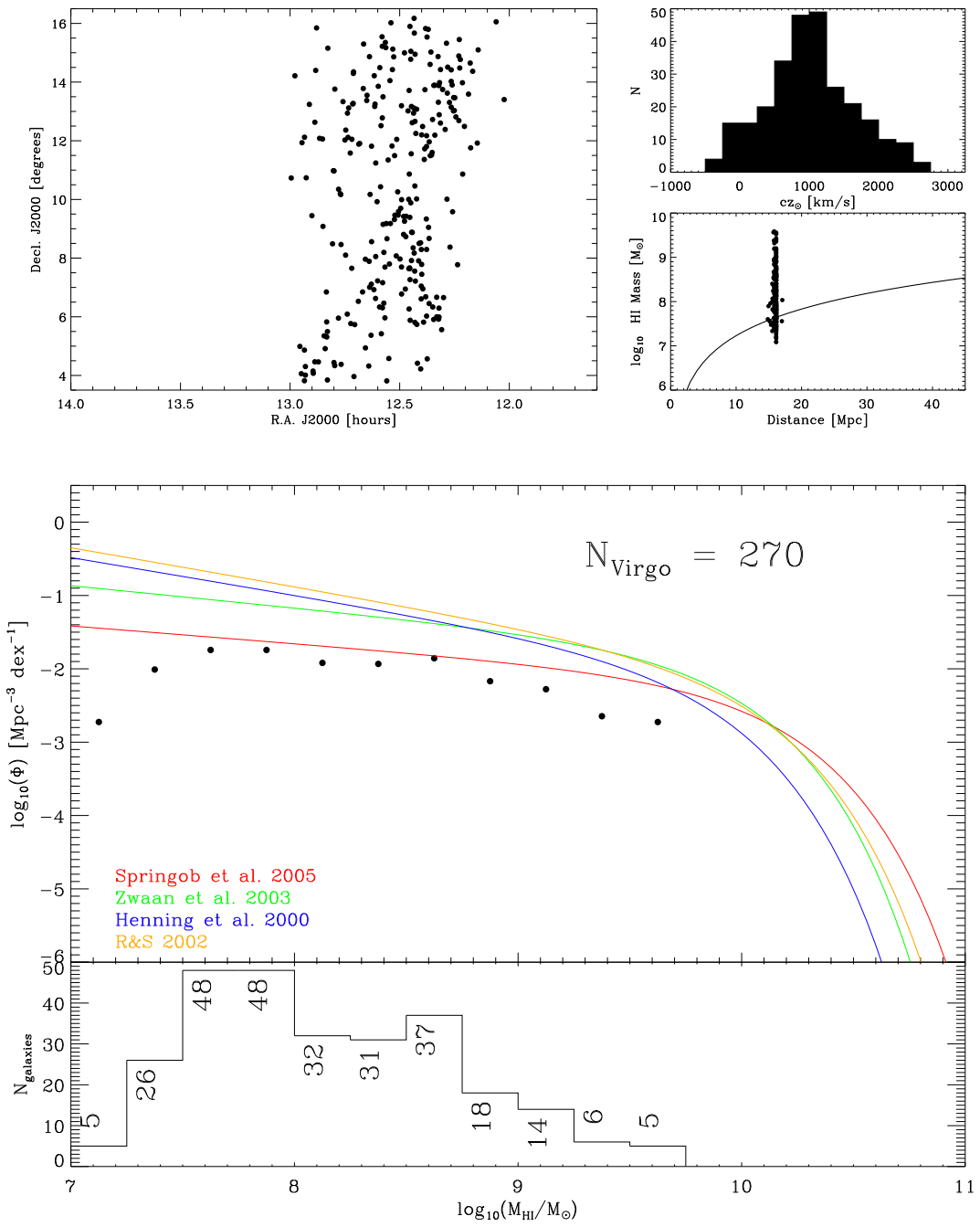

Figure 6.4: Data used to build a HI mass function for the Virgo ALFALFA data set. The sky plot, *cz* distribution, and Spänhauer diagram at the top of the figure show the data used to construct the HIMF. The bottom plot shows the HIMF and binned mass distribution. Four reference Schechter fits from the literature are shown in color.

6.3 Simulating a Galaxy in a Cluster Environment

Results from galaxy surveys have revealed the importance of environment on galaxy evolution. Observing individual galaxies in binary pairs has clearly shown how interactions can affect morphology and star formation. Multi-wavelength observations reveal important differences in the dynamical effects on the stellar and gaseous components. Observations of galaxies through the 21cm line of neutral hydrogen have become particularly important in understanding tidal and hydrodynamical effects on the disk gas content.

Changes in morphological evolution can manifest themselves as warped or asymmetries, differences in gas or stellar disks, and tidal tails that can be hundreds of kiloparsecs long. Canonical examples, including the NGC 4038/4039 pair and the M81/82 group, reveal the effects on gas and stars from interactions within a group (Yun et al. 1994; Chynoweth et al. 2008). Effects on galaxies in a rich cluster can be similar in nature to a certain degree. However, the large centrally concentrated mass, high-galaxian density, and hot intracluster gas can affect galaxies in different, sometimes more extreme ways. HI deficiency is commonly seen in more centrally located massive spirals, attributed to ram pressure stripping of galaxies' disks through interactions with the hot intracluster gas. It has also been shown that galaxy harassment scenarios where high speed encounters with both the cluster potential and other galaxies can result in large streams being ripped off the galaxy (Moore et al. 1998; Davies et al. 2005).

The Virgo Cluster offers the opportunity to study a high–density environment that is both nearby (D_{Virgo} = 16.7 Mpc) and in the process of forming – the outer periphery of Virgo has not reached viral equilibrium (Binggeli et al. 1993). Many outlying subclumps are thought to be falling into Virgo at high speed (Vollmer et al. 2001, 2008). Obser-

vations have been reported of streams of gas and stars seen in Virgo, including through diffuse optical emission (Mihos et al. 2005) and through observations of gaseous streams from both ram pressure stripping, galaxy harassment, and close, high speed encounters (Oosterloo & van Gorkom 2005; Haynes et al. 2007). The origins of more isolated HI clouds in the Virgo periphery with no apparent stellar counterparts are difficult to determine. They could be remnants of the aforementioned dynamical processes (Kent et al. 2007). The formation of these streams, and more importantly, the survival of remnant gas clouds is important for understanding cluster evolution.

The objective of the work described in the next section is to simulate and understand the following: (a) dynamics of a high speed encounter of a large disk galaxy with a Virgo cluster-like gravitational potential and intracluster gas distribution, (b) timescales for dissipation of remnant HI clouds, (c) physical processes that contribute to the formation of observed tails, i.e. galaxy harassment and/or ram pressure stripping, and (d) how projection effects and viewing angles affect observations.

6.3.1 Initial Conditions and Methods of Simulation

Simulations for this work made use of the N–body, smoothed particle hydrodynamics (SPH) code called GADGET-2 (Springel 2005). The code allows for easy tracking of the bulge and disk (stellar and cool gas) components of the simulated galaxy, as well as the hotter cluster gas. The facilities of the Cornell Center for Advanced Computing were used to run the code. Sixteen dual-core Xeon processors running at 2.4 GHz were used in parallel, each with 2GB of memory.

Observational evidence has shown that large spiral galaxies tend to be most affected by the cluster environment; therefore a disk galaxy was modeled in this simulation. The

simulated galaxy and associated initial conditions were constructed using a stellar disk and bulge, gas disk, and dark matter halo. GADGET-2 allows for gas particles to interact both gravitationally and hydrodynamically; all other particles interact via gravity only.

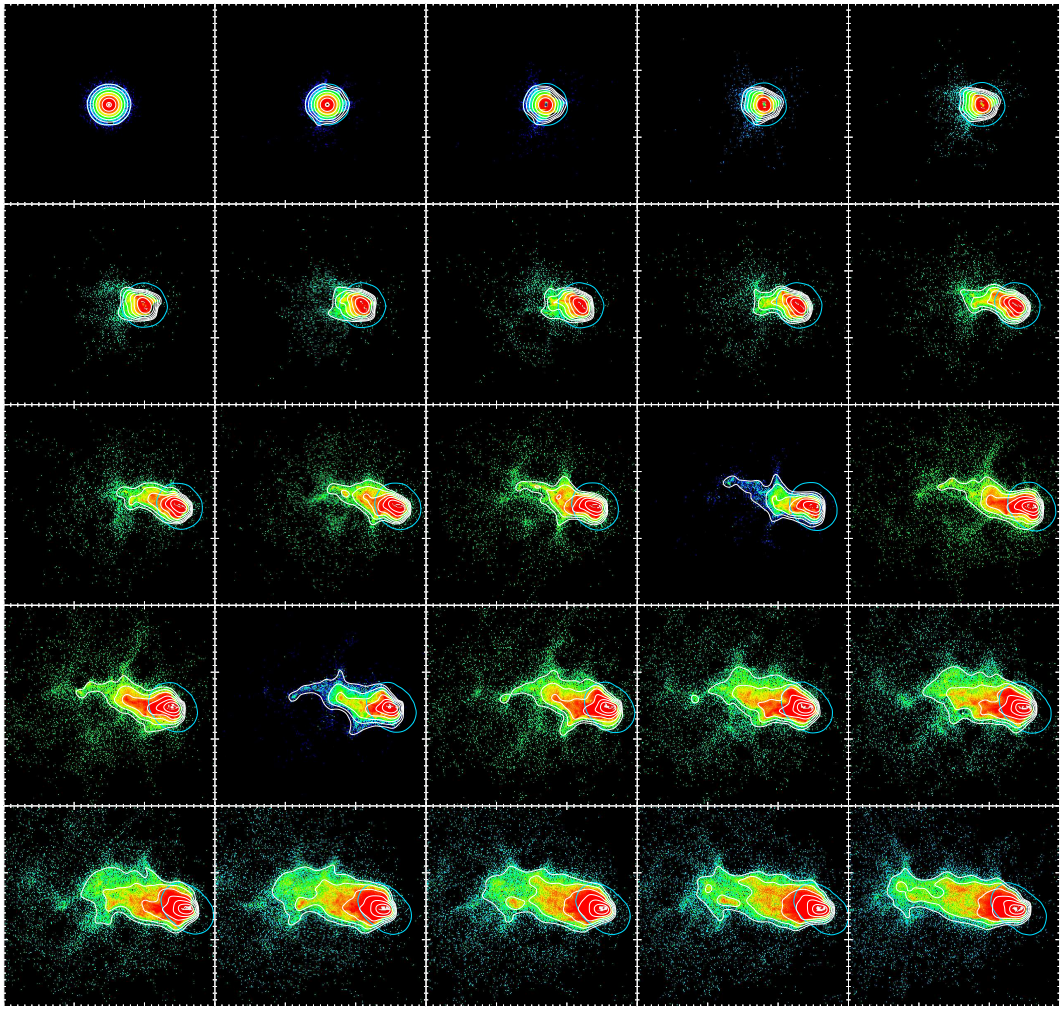

Figure 6.5: GADGET-2 snapshots viewed from a disk inclination of 0°. Each box is 300 kpc in size and tracks with the galaxy as it moves through the intracluster medium. The time between frames is 10 million years. Column density contour levels are plotted for $\log(N_H)$=18.47,19.0,19.5,20.0,20.5,21.0,21.5 cm^{-2}. The blue line traces the stellar disk during the course of the galaxy's movement through the cluster.

The galaxy model mimics the parameters of NGC 4254, a large galaxy known to be harassed in the Virgo Cluster environment (Haynes et al. 2007). Model parameters use values from previous studies by (Dickey et al. 1990) and (Rownd et al. 1994), as

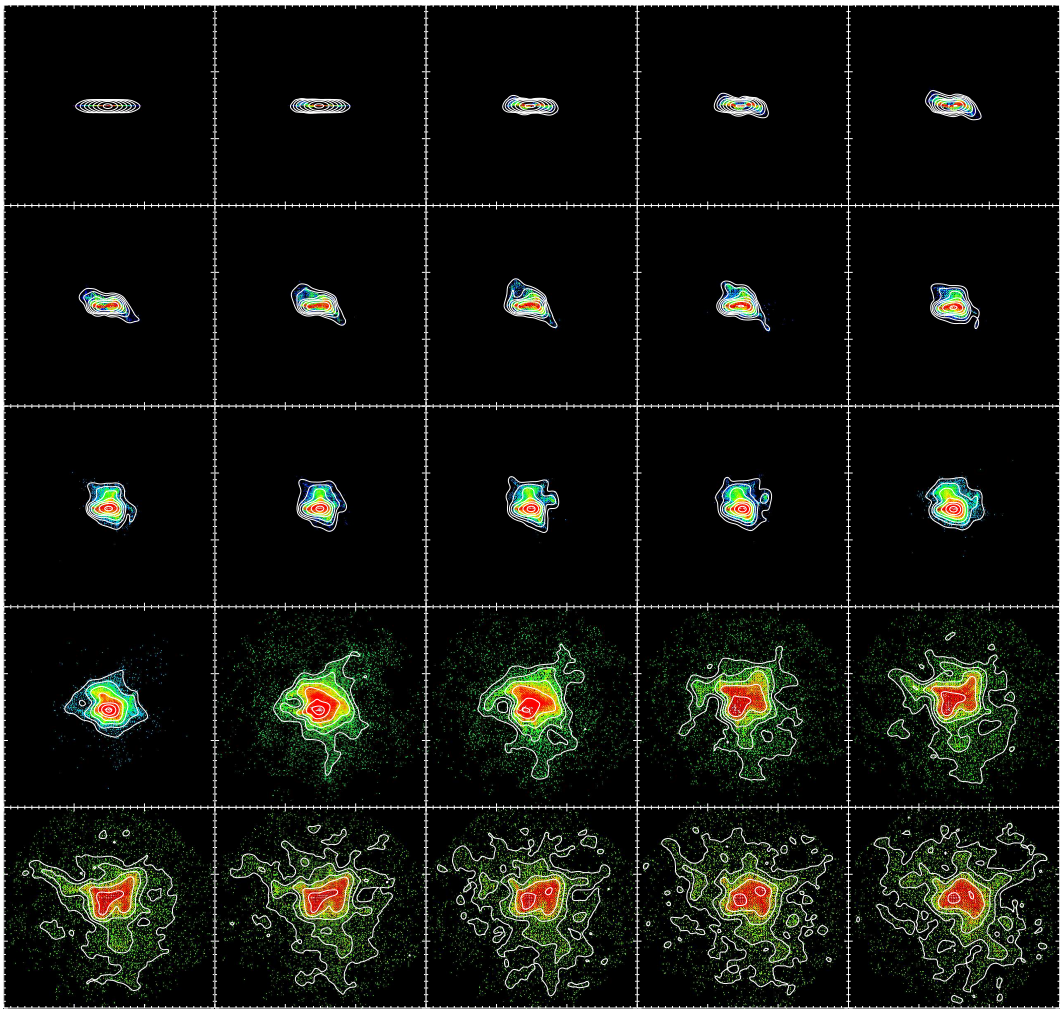

Figure 6.6: GADGET-2 snapshots viewed from a disk inclination of 90°. Each box is 300 kpc in size and tracks with the galaxy as it moves through the intracluster medium. The time between frames is 10 million years. Column density contour levels are plotted for log(N_H)=18.47,19.0,19.5,20.0,20.5,21.0,21.5 cm^{-2}.

these also describe giant disk galaxies. The simulation utilized 1 $\times 10^6$ total particles for the galaxy. The galaxy disk consists of exponential and stellar components with a scale length of 3.5 kpc, total disk mass of 3.1 $\times 10^{10} M_{\odot}$, circular velocity of 230 km s^{-1}and velocity dispersion of 10 km s^{-1}. The gas mass fraction of the disk is 25%, with a temperture of 100 K.

The stellar bulge is modeled as a Plummer sphere (Plummer 1915), with a density

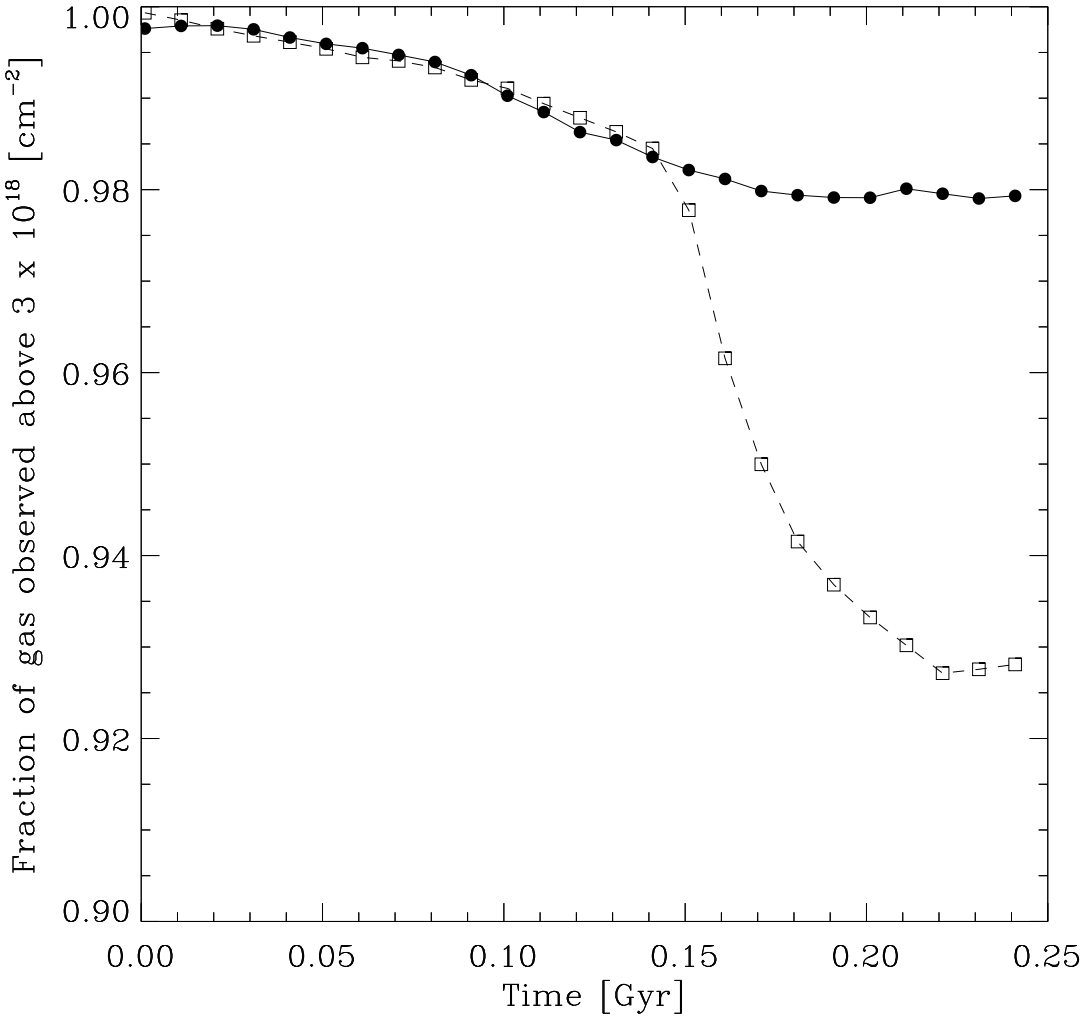

Figure 6.7: Observed disk gas loss for both viewing orientations. The fraction of gas observed in the simulation for $N_H \geq 3 \times 10^{18}$ cm^{-2} is plotted for i =0°(filled circles) and i =90° (open squares).

distribution of a relaxed $n = 5$ polytrope given by

$$\rho(r) = \frac{3}{4\pi}\frac{M_B}{R_B^3}\frac{1}{(1+(r/R_B)^2)^{5/2}}. \tag{6.2}$$

The bulge mass is $M_B = 10^{10} M_\odot$, and bulge radius is $R_B = 1$ kpc.

The dark matter halo is modeled as a softened, isothermal density profile given by

$$\rho(r) = \frac{\rho_0}{1 + (r/r_c)^2}. \tag{6.3}$$

The halo parameters consist of a total mass of 5.98 $\times 10^{11} M_{\odot}$, cutoff radius of 50 kpc, and core radius of 2 kpc. With all components combined the total dynamical mass of the galaxy is $M_{tot} = 6.2 \times 10^{11} M_{\odot}$.

The cluster is also modeled with a simple Plummer sphere of gas particles using simple "Virgo" like parameters. These parameters include a gas temperature of 10^7 Kelvins, total mass of $M_C = 10^{14} M_{\odot}$, and core radius of 1 Mpc. The galaxy is placed 1.4 Mpc away from the cluster center with an initial velocity of 1000 km s^{-1} directed at 45° to the radial vector between the galaxy and cluster center. The simulation run described has an azimuthal angle of 90° counter-clockwise with respect to the x-axis of the simulation, and polar angle of 0°.

6.3.2 Preliminary Results

A small number of snap shots have been obtained from the simulation covering 0.25 Gyr. The results show the gas being ram pressure stripped away from the direction of motion, viewed at two different inclination angles in Figures 6.5 and 6.6. To confirm that gas loss is occurring in the disk, a simple exercise was carried out to show what fraction of gas originating from the disk would be observable. For both viewing orientations, the fraction of gas above a column density of $N_H \geq 3 \times 10^{18}$ cm^{-2} was computed. The preliminary computation shows that a galaxy viewed at an edge-on inclination of i =90° would result in an observation seeing less gas along the line-of-sight, shown in Figure 6.7. Continued simulation runs will explore more time steps and further evolution of the system.

CHAPTER 7

SUMMARY AND FUTURE WORK

When you make the finding yourself –
even if you're the last person on Earth to see the light –
you'll never forget it.
- Dr. Carl Sagan

7.1 Overview

The preliminary ALFALFA HI study toward the Virgo cluster region of sky has been presented. The survey is currently in its fourth year of operations. Several terabytes of raw and high quality reduced data have been generated. Three catalogs with over 1800 HI detections have been published, with three more to be published in the coming year. The survey project is ongoing and is scheduled to be completed within a few years of the publication of this dissertation. Current survey efforts explore a wealth of science that complement the presented work, including surveys for galaxies in the *anti*-Virgo region, high-velocity clouds, intermediate-*z* OH megamasers, and HI absorption lines. The data for HI mass determinations for the whole survey, cross-correlation functions, HI deficiency studies, and other statistical analysis are currently underway. Follow-up efforts including observations with other facilities at optical, infrared, and radio wavelengths are crucial. High resolution VLA mapping of nearby HI clouds will yield rotational kinematics and place limits their star formation potential. Parallel N-body and SPH simulations will examine the evolution of these HI clouds in a variety of environments, including a large cluster potential with hot intracluster gas, as well as small galaxy groups.

Significant effort has also been placed to export catalogs and spectra into the new

paradigm of the Virtual Observatory. The collaborative online databases are allowing other groups to cross correlate results as the ALFALFA catalogs are published. Various in-house client applications have been created to bring imaging data into the ALFALFA data reduction pipeline.

The catalog, compiled from the efforts of Giovanelli et al. (2007), Kent et al. (2008), and Koopmann et al. (in preparation), encompasses the most homogeneous HI survey of the cluster to date. The ALFALFA minimum detectable mass at the Virgo distance of 16.7 Mpc is $2 \times 10^7\ M_\odot$. The wide area coverage of the survey and carefully constructed data reduction process have resulted in the discovery of several HI clouds in the cataloged data set. These clouds are all of order $\sim 10^8\ M_\odot$ or less, and exhibit no apparent optical counterpart in imaging available from online databases.

7.2 HI Clouds

We have reported on the detection of eight HI features not coincident with stellar counterparts in the Virgo Cluster region. All of the HI clouds have $cz_\odot \leq 3000$ km s^{-1}and, if at the Virgo distance, HI masses between $1.9{\times}10^7\ M_\odot$ and $1.1{\times}10^9\ M_\odot$. The VLA observations for one of the more isolated, unresolved clouds (Chapter 4, Cloud 2) have revealed a small system of several HI clumps, spread over approximately 20-25 kpc, which, if gravitationally bound, exhibits a similar separation timescale ($<$ 1 Gyr) as one of the large detections (Chapter 4, Cloud 7).

We have utilized data sets from the ALFALFA survey and follow-up observations with the Very Large Array in C configuration to obtain both single dish and aperture synthesis observations of a new HI cloud complex in the Virgo Cluster. The observations reveal multiple components, all within 15′ of the central clump. The results of these

observations and their interpretations are summarized as follows:

1. Five separate HI cloud detections in the ALFALFA survey between $cz_\odot$ ~500 and 600 km s^{-1} are part of a HI cloud complex. The complex is assumed to be at the distance of the Virgo cluster (D_V = 16 Mpc), with individual masses in the range 0.48–1.7 $\times 10^8$ $M_\odot$ and a total complex mass of 5.1×10^8 $M_\odot$. The clouds' velocity widths vary between 50 and 250 km s^{-1}. In the latter case, the wide spectrum is likely to be due to a blend of several poorly resolved clumps.

2. Higher resolution VLA observations reveal detections corresponding to the positions and velocities of clouds C1 and C2, with sizes of 2.7 and 1.5 arcminutes respectively. If C1 and C2 are self-gravitating, then the dynamical masses would be 2.3×10^9 $M_\odot$ for C1 and 0.3×10^9 $M_\odot$ for C2. Faint optical features are found in the vicinity of the two clouds. Lack of optical redshifts prevent us from establishing a physical association. If the optical features were associated with the two clouds, their HI mass to g–band luminosity ratios would be respectively $M_{HI}/L_g \sim 170$ for C1 and $M_{HI}/L_g \sim 30$ for C2, in solar units. The synthesis maps do not exhibit any degree of symmetry in the gas distribution or in the velocity field. If the HI complex as a whole is bound by self-gravity, then its total dynamical mass would be of order 10^{11} $M_\odot$.

3. Nearby spiral galaxies NGC 4424 ($cz_\odot$ = 437 km s^{-1}) and NGC 4445 ($cz_\odot$ = 354 km s^{-1}) appear to be likely parent sources for the cloud complex origin. The total HI mass of the cloud complex is equivalent to between 1/2 and 1/3 of the HI lost by NGC 4424 and about 4/5 of the HI lost by NGC 4445. NGC 4445 is located at a closer projected distance of 150 kpc. While both galaxies are extremely HI deficient, gas loss estimates and timing arguments indicate that NGC 4445 is the more likely candidate associated with the cloud complex. Relative velocities and

spatial displacements between NGC 4445 and the HI cloud complex indicate that the separation of the gas from the parent galaxy would have taken place at least 0.5 Gyr ago, and the motion of clouds and parent galaxy would be seen to take place at an angle of order $sim60^\circ$ from the line of sight.

4. It is unlikely that the HI clouds are primordial in nature, embedded in their own dark matter halos. A more plausible scenario is that the complex is material removed from a galaxy (in this case NGC 4424 or NGC 4445) traveling through the cluster at high speed. Evidence has been presented indicating that a ram pressure stripping event is preferred to a purely gravitational one.

7.3 Future Work

7.3.1 Galactic Neutral Hydrogen

The current ALFALFA bandpass is centered at 1385 MHz, covering a bandwidth of 100 MHz. As a result, ALFALFA also observes perigalactic high-velocity clouds(HVCs) and galactic HI. An initial map of galactic HI has been created from 402 data cubes observed and reduced by the ALFALFA collaboration. Each data cube covers $2.4^\circ \times 2.4^\circ$ of sky, with a pixel resolution of 1 arcmin pixel^{-1}. ALFALFA maps are exported from the *IDL* environment, and mosaicked using the *Montage* C libraries (Laity et al. 2005; Berriman et al. 2007). The result is the tri-color wide-field equal area Aitoff projection shown in Figure 7.1.

The Montage process is versatile in that it allows the use of all coordinate systems and projection types typically found in astronomy. The code is scalable and can be run in parallel on multiple processor systems through the Message Passing Interface. The

process involves conversion of ALFALFA data cubes to FITS files with W3C and astrometric information in the headers. Central to the speed and efficiency of the algorithm for small areas of sky is the use of a plane-to-plane reprojection algorithm, which uses gnomonic and orthographic projections to reproject through a common point to the center of a sphere. Larger images (such as the Cartesian gridded data in ALFALFA) require a reprojection onto sky coordinates before reprojecting onto a plane, resulting in longer processing times. Using multiple processors on recent computer hardware allows the creation of a full sky ALFALFA mosaic within 48 hours.

The background matching algorithm uses simple surface fitting functions to rotate and offset the images to a common background. The ALFALFA galactic HI mosaic is derived from the spring sky data set grids shown in Figure 2.8. A least squares fit is used on each grid and its neighbors (eight per grid) to determine the best offset and gradient to apply for a background correction. This background modeling allows for a common flux scale to be achieved across all the re-projected images of the entire mosaic. Current and future work involving galactic HI and its extension to nearby HVCs and HI debris in the Local Group is an ongoing process, and the results will be discussed in the near future.

7.3.2 High-Velocity Clouds

N-body simulations employing the Λ-CDM paradigm predict more dwarf galaxies than are currently observed in the Local Group (Moore et al. 1999; Klypin et al. 1999). The characterization of any nearby candidate objects such as gas-rich mini-halos will shed light on the expectations of galaxy formation paradigms. Studies of both galactocentric high-velocity clouds (HVCs; Verschuur 1969) and nearby dwarf galaxies like SagDEG

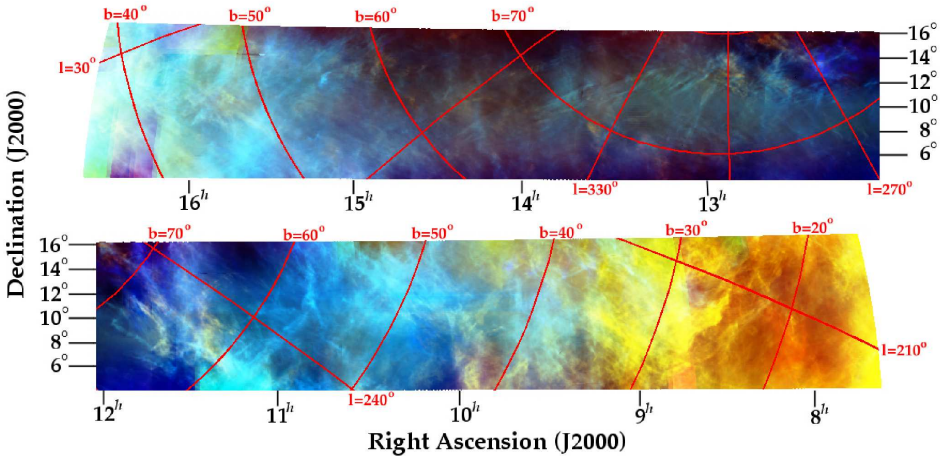

Figure 7.1: 1527 deg^2 wide-field equal area Aitoff projection of galactic HI observed with the ALFALFA survey near the North Galactic Pole (NGP). Data cubes are processed in *IDL* and mosaicked using the libraries provided by *Montage* (Berriman et al. 2004, 2006). The data have been binned into three overlapping velocity bins. The bins are combined into a tri-color RGB image – Blue: -50 < v_{lsr} < 0 km s^{-1}; Green: -25 < v_{lsr} < +25 km s^{-1}; Red: 0 < v_{lsr} < +50 km s^{-1}. The pixel resolution of the ALFALFA data cubes is 1 arcmin pixel^{-1}. The elliptical half-power beamwidth of the ALFA receiver is 3′.8 × 3′.3.

have revealed important information on the dynamics of Local Group objects. With the advent of large–scale multicolor optical surveys such as 2MASS and SDSS, the periphery of our Galaxy has been discovered to be an active laboratory of tidal events. The discovery of the tidally disrupted Sagittarius dwarf spheroidal (SgrDS) by Ibata et al. (1997) was followed by the spectacular stream associated with it, by Majewski et al. (2003) and “its siblings” (Belokurov et al. 2006a,b). A wide array of “high-velocity” phenomena have been identified in the ALFALFA survey, in both the Virgo and anti-Virgo regions. These include both compact high-velocity clouds (CHVCs) and long stream-like features such as those shown in Figures 7.2 and 7.3. The stream is over 4 degrees and exhibits an velocity gradient along the main feature. Followup analysis and modeling of the feature is planned.

A sample of 60 positive velocity ALFALFA HI clouds in the north galactic polar

region (NGP) have been identified for $V_{LSR} > 100$ km s^{-1} and $b > 35^{\circ}$. This restriction also excludes most of the known HI emission by the so–called Leading Arm feature (LA; Lu et al. 1998; Putman et al. 1998; Connors et al. 2006) of the disturbed Magellanic system. No discernible optical emission is seen in any of the HVC fields, either by inspection of SDSS or DSS2. A subset of the clouds are relatively extended (>15′) and exhibit stream-like morphology. They are more likely explained by models that place them at relatively small distances (<100 kpc), whereby they are vulnerable to tidal disruption by the Milky Way. A larger subsample of about 45 objects appear very compact, and in many cases are unresolved by the 4′ resolution of ALFALFA. Future studies will target a sample of these objects with the Very Large Array.

7.4 Future Endeavors

The ALFALFA survey has been incredibly productive in both exciting scientific discoveries and the dissemination of catalogs and spectra to the astronomical community. However, the project and its goals, including the work culminating in this dissertation, are far from finished. This work is a complement to other regions of sky covered by ALFALFA, the catalogs of which will be published in the near future. The data cubes covering the area North of the Virgo Cluster will continue to sample a region along the supergalactic plane. The HI mass function determination for Virgo will be compared to HIMF's for the field as well as the global HIMF for the entire HI survey. These studies will detail the HIMF's dependency on environment and the survey sensitivity will allow for a statistically significant sample of HI detections at the low mass end. The cosmologically fair sample of HI-bearing objects produced by the survey coupled with HIMF studies, aperture synthesis follow-up on gas-rich, optically unseen detections, and simulations in various environment will produce an unprecedented view of the local

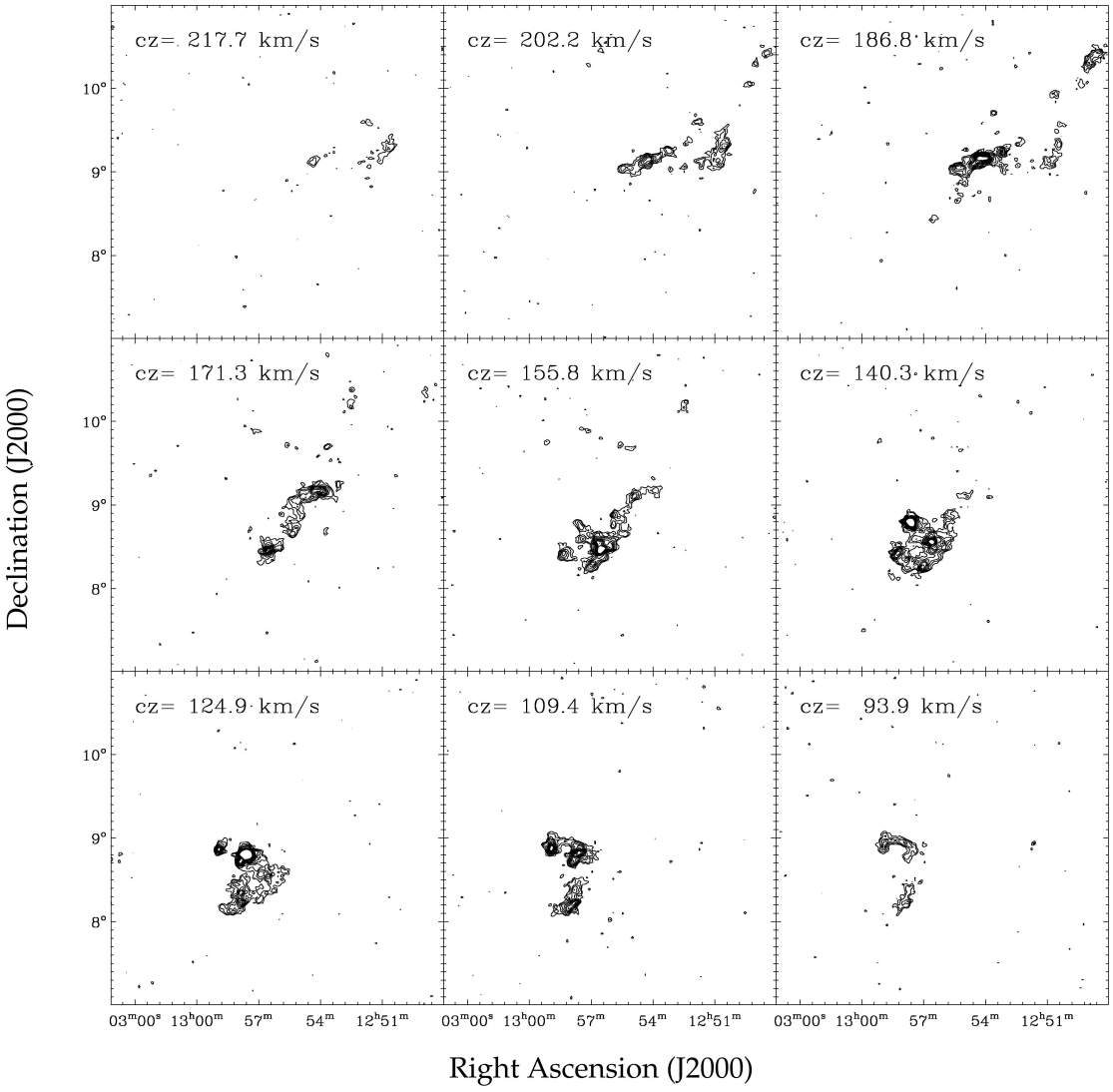

Figure 7.2: Moment maps of a new HI stream feature detected in the ALFALFA survey. The stream is over four degrees in extent and covers 130 km s^{-1} in velocity space. Contour levels for the maps are at 130, 200, 300, 400, 500, 600, 700, 800, 900, and 1000 mJy km s^{-1} $beam^{-1}$.

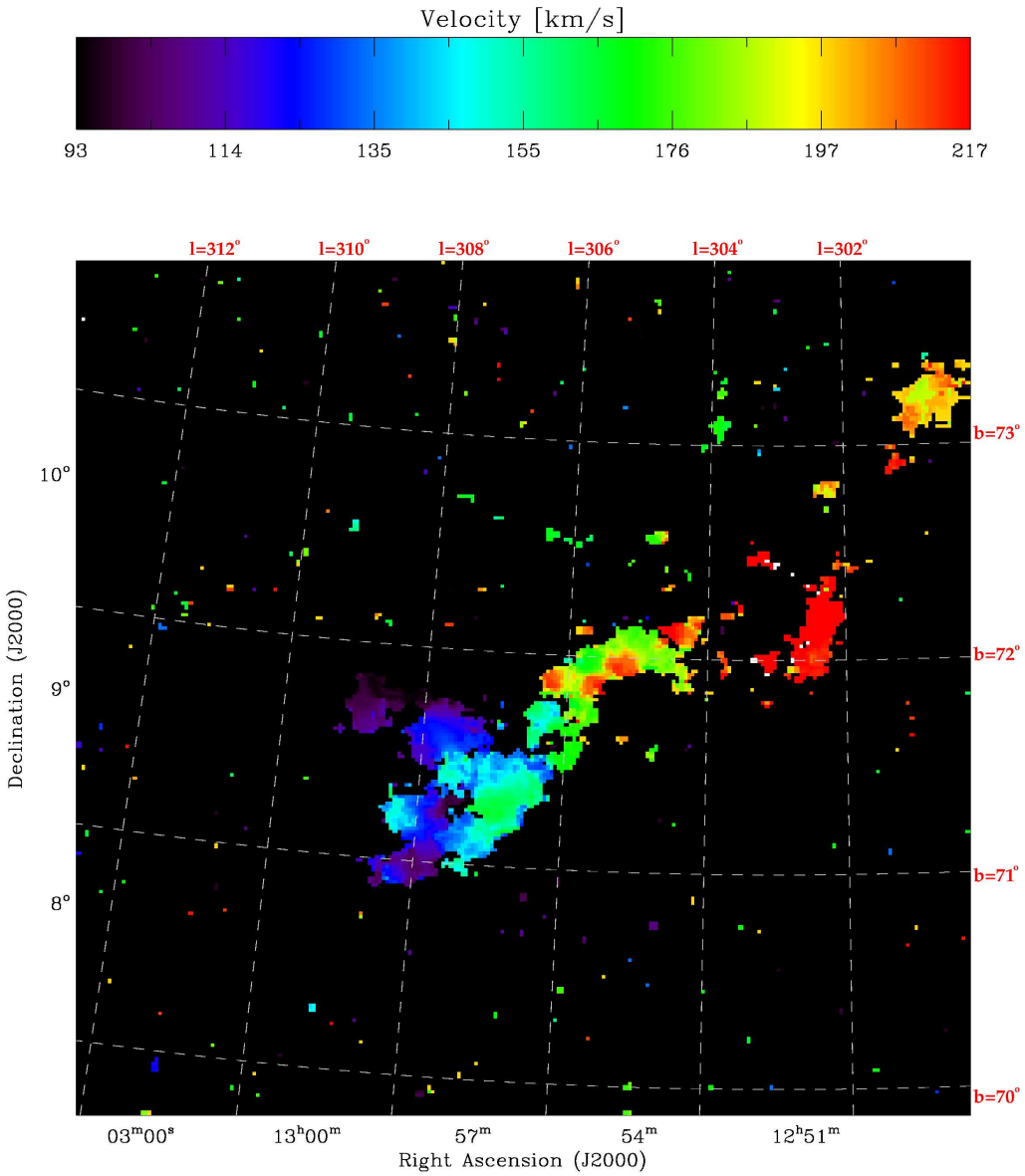

Figure 7.3: Intensity weighted velocity map (first moment) of a high-velocity cloud stream detected in the Virgo region catalogs. The dashed lines (red labels) indicate galactic coordinates.

universe's gaseous content.

A large effort has been placed on the technical and software development of the survey. This will continue, especially in the distribution of data cubes through online web services. In addition to intensifying the study of science topics discussed in this dissertation, I will contribute to the scientific and technical development of future NRAO facilities including the Atacama Large Millimeter Array as a Jansky Fellow at the National Radio Astronomy Observatory.

APPENDIX A

VIRTUAL OBSERVATORY

A.1 Introduction to the Data Access Layer: Cone Search Protocol

The cone search is the simplest of the VO protocols to implement and use. These services provide a basic research tool for data access and play an important role in the data access layer (DAL). As the first data access layer protocol used in the VO, the cone search aims to be simple so that data providers can quickly implement it as a powerful search tool. The requirements for using and publishing a cone search service, as well as required responses from the service will be described[1].

A.1.1 Service Query Requirements

The cone search represents one of the simplest queries that can be created – searching within a specified radius on the sky and forming a cone. A cone search service must respond to an HTTP GET request with three input parameters:

```
http://<base_url>?RA=187.0&DEC=12.0&SR=6.0
```

The three required input parameters to the request are the Right Ascension (RA) and Declination (DEC) (both epoch J2000), as well as a search radius (SR), all in decimal degrees. An optional verbosity parameter (VERB) may be specified by the user to specify the number of columns to be returned by the service, with a value of 1 meaning the bare minimum and a value of 3 being all columns in the table.

[1]Elements of this chapter have been reproduced by permission of the Astronomical Society of the Pacific from ASPCS volume 382.

Service Response Requirements

A cone search service will respond to a query with an XML VOTable document, of MIME type text/xml, containing any results in the service's catalog that meet the search criteria. The service implementer may decide to additionally include data that fall outside the requested cone, e.g. when the cone defines a circular search region but the data provider returns all results from a rectangular region of the same width. The returned VOTable must contain a single <TABLE> element within a single <RESOURCE> and must have at least the three unique <FIELDS> described in Table A.1 1. UCD+ notation (Unified Content Descriptor) using periods to denote the hierarchy is preferred, however some systems may use the permitted, but older all caps syntax with underscores. First time data managers should employ the UCD+ syntax. These three columns will be the bare minimum returned in the case of VERB=1 in the web query. Other fields in the VOTable should be properly described with the correct units and data types.

Table A.1: Required field UCDs for the cone search.

Field UCD+	Unit	Type	Short Description
meta.id	N/A	char	Main identifier for the object in the row (must be unique)
pos.eq.ra.main	degrees	double	J2000 Right Ascension
pos.eq.dec.main	degrees	double	J2000 Declination

Error Responses

In the event that improper input is passed to the service, the cone search should respond with the metadata describing the service, and a single parameter field ERROR in the table. Possible cases of error include an absence of one of the three required input parameters, a search radius larger than allowed by the service, or numerical/ logic errors

(e.g. DEC=-100.0). Input parameters that result in a query where there is no data should not return an error, but instead should return the metadata for the table. SR=0 is a special case used to query the service to determine the fields returned by the service without triggering an error.

Resource Metadata and the Registry

All valid cone search services should have an entry placed in the registry so that they are exposed to the greater VO infrastructure. Table 2 describes the necessary metadata used to describe the service. The service can be published in the NVO Registry using the Resource Type CONE. Once a service has been implemented, it can be tested with a cone search validator. The validator will test any specified cone search service with a standard query, a metadata query, and a user input error query. The validation service will display any compliance errors, warnings, and recommendations for the service. Accessing a cone search service will be described in the next section using a variety of software packages.

A.2 Using Cone Search Client Applications

Obtaining catalog subsets of objects in selected regions of the sky is one of the most basic searches conducted in astronomy. In this tutorial, we will examine how to use software libraries in various languages included in the software distribution to build simple client applications for calling cone search services. The user will specify coordinates in Right Ascension and Declination, and a search radius. The cone search service will return a VOTable of objects that the user can analyze using VO tools or other software packages in their own environment.

A.2.1 The Cone Search Specification

The cone search protocol was one of the first service specifications to be created for the Virtual Observatory. It represents one of the simplest queries an astronomer can create - searching for cataloged objects within a given patch of sky, specified by a central set of coordinates and search radius. A cone search service responds to an HTTP GET request of the form:

```
http://<base url>?RA=187.0&DEC=12.0&SR=6.0
```

The input parameters are the Right Ascension and Declination in decimal degrees (J2000), as well as a search radius in decimal degrees. In addition, the cone search allows an optional VERB keyword (for verbosity), which is an integer that determines how many columns should be returned by the service (with values of 1 for the minimum, and 3 for all columns in the data set being queried). A cone search service will respond with a VOTable containing the results of the search, a table describing the fields returned by the service but with no data, or an error response.

A.2.2 Examples of Using a Cone Search

Examples of using cone search clients in various languages and environments are given below. Each example will produce the same result – the returned VOTable can be saved for later use or used immediately in a scientific plotting environment such as IDL or VOPlot.

Interactive Data Language (IDL)

IDL affords the advantage of having XML support as well as a fully featured scientific plotting and numerical analysis environment. A cone search can be called via routines from the VO IDL library. The procedure requires that the cone service URL, Right Ascension, Declination, and search radius be passed in as parameters. The returned VOTable is written to an IDL structure variable. The VO IDL library procedures are located in $ NVOSS_HOME/idl/VOlib_0.2/pro/.

```
IDL> url=http://arecibo.tc.cornell.edu/hiarchive/cone.php?
IDL> conecall, str=table, url, 187, 12, 6
```

Java

The Java VO library contains a class for handling a cone search. The callCone- Service() method uses an external service, defined in the file $NVOSS_HOME/java/src/coneclient/build.xml. The method can be called from the directory $NVOSS_HOME/java/src/coneclient/.

```
> java callConeService(187.0, 12.0, 6.0,
http://arecibo.tc.cornell.edu/hiarchive/cone.php?)
```

Python

The Python libraries (Kwok 2008) can be used with an example file ConeSearchEx.py below. The classes can be found in and the example files in $NVOSS_HOME/python/volib/ and the example files in $NVOSS_HOME/python/samples/.

```
> python ConeSearchEx.py coneSearchVOTable
http://arecibo.tc.cornell.edu/hiarchive/cone.php? 187,12,6
```

PHP

The PHP libraries can be embedded in web pages to access various cone search services by creating an instantiation of the Cone Search class. Note that this PHP library uses the simpleXML feature of PHP 5 to manipulate the XML document. The files containing the PHP classes are located in $NVOSS_HOME/php/web/phpVOlib and may be used as in:

```
//Create a new coneSearch object
$coneObject = new Cone-
Search(http://arecibo.tc.cornell.edu/hiarchive/cone.php?);
//Use this to print the raw VOTable
echo $coneObject->getRaw(187.0, 12, 6);

//Alternatively, use this to fetch in a VOTable format and then
//print as an XML file in the browser
$vot=$coneObject->getVOTable(187.0, 12.0, 6.0)
echo $vot->getAsXML();
```

IRAF

IRAF access to cone services is through the VOClient interface (Tody & Fitzpatrick 2008), this integration provides both programmatic access in the CL scripting environment as well as a task interface. Functions exist in the CL to resolve a service name to a URL automatically and so the standard task interface would look something like:

```
cl> vocatalog HIA 187.0 12.0 6.0
```

In this case the HIA refers to the ShortName entry of this service in the Registry that the task will resolve internally. The result is printed to the terminal as an ASCII table since the task converts from the VOTable internally as well. Using the CL scripting syntax, the query would look much as it does in other languages, however instead of printing the resulting VOTable directly, the user would normally be required to manually walk through the result table.

Simple Web Request

A cone search service executes as an HTTP GET request, and so it can also be typed as the target in a web browser or as a wget command. For example, type the following URL at the web browser:

```
http://arecibo.tc.cornell.edu/hiarchive/cone.php?
RA=187.0&DEC=12.0&SR=6.0
```

or at the command prompt (Windows and OSX users will need to download wget)

```
> wget -q -O votable.xml ‘‘http://arecibo.tc.cornell.edu/hiarchive/
cone.php?RA=187.0&DEC=12.0&SR=6.0’’
```

The Returned VOTable File

A cone search service will return a VOTable similar to the output below. The results of the cone search queried in this document are shown in Figure A.1.

```
<?xml version="1.0" encoding="utf-8"?>
```

```
<!DOCTYPE VOTABLE SYSTEM "http://us-vo.org/xml/VOTable.dtd">
<VOTABLE>
<RESOURCE>
<DESCRIPTION>Cornell University HI Archive: Springob, et al. 2005,
ApJS,160,149 </DESCRIPTION>
<TABLE>
<DESCRIPTION>Cornell University HI Archive: Springob, et al. 2005,
ApJS,160,149 </DESCRIPTION>
<FIELD ID="AGCUGC" ucd="ID_MAIN" datatype="char">
<DESCRIPTION>Arecibo General Catalog number</DESCRIPTION>
</FIELD>
<FIELD ID="othername" ucd="META_ID" datatype="char" arraysize="15">
<DESCRIPTION>Other name (NGC, IC, etc.)</DESCRIPTION>
</FIELD>
<FIELD ID="RA" ucd="POS_EQ_RA_MAIN" datatype="double" unit="deg">
<DESCRIPTION>Right Ascension(J2000) in decimal degrees</DESCRIPTION>
</FIELD>
</FIELD>
<FIELD ID="b" ucd="PHYS_ANGSIZE_SMINAXIS" datatype="double"
unit="arcmin">
<DESCRIPTION>Blue minor diameter in arcminutes</DESCRIPTION>
</FIELD>
...
...
<DATA>
<TABLEDATA>
```

```
<TR>
<TD>7048</TD>
<TD> N4067</TD>
<TD>181.04833333</TD>
<TD>10.85416667</TD>
<TD>1.2</TD>
<TD>0.9</TD>
<TD>3</TD>
<TD>4.68</TD>
<TD>5.39</TD>
<TD>5.58</TD>
<TD>0.59</TD>
...
```

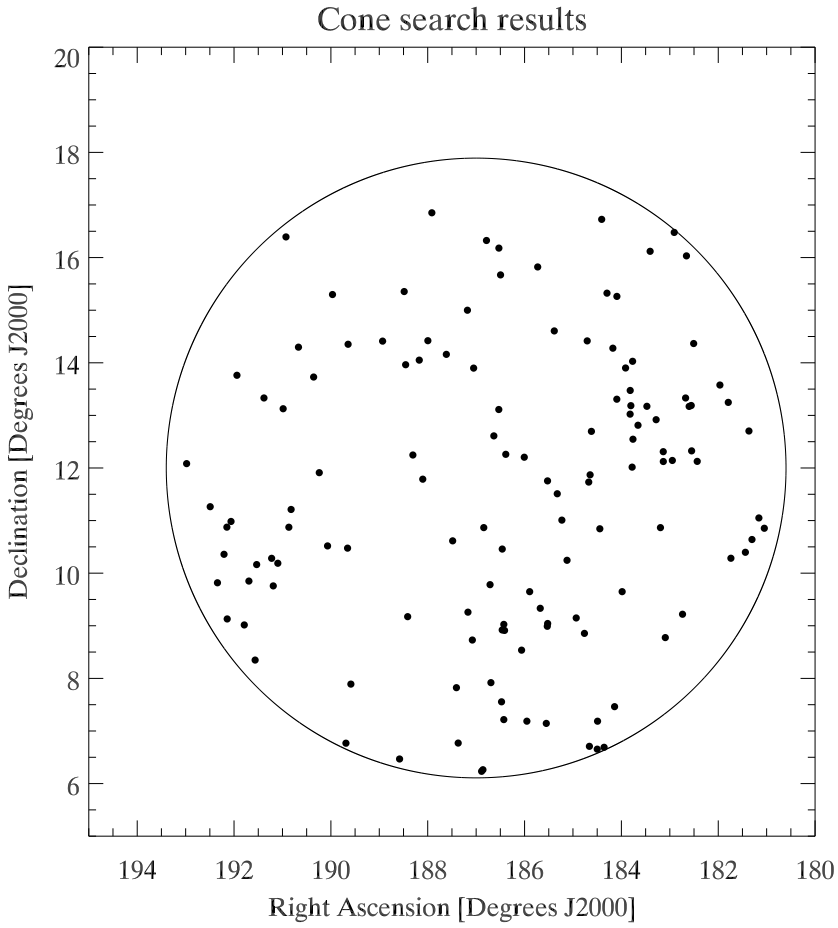

Figure A.1: Plot of objects within six degrees of the queried position returned from the cone search of the Cornell Digital HI Archive (Springob et al. 2005b).

A.3 3. Building a Simple Cone Service

The cone search service protocol will be examined from the server side in this chapter. A simple cone search service will be setup and configured locally using MySQL. Data will be read into a table, and the Java JDBC will be used to connect to the database. Readers will understand the VO cone search specification and how to use it to query a database on their local systems and return an XML/VOTable file based on an input of RA/DEC coordinates and a search radius. The cone search in this example will be

deployed as a Java servlet. The resulting cone search can be tested with a verification service. This basic setup can be used with other languages and relational databases.

A.3.1 Overview and Requirements

A basic requirement in astronomy is to have the ability to search a catalog of objects with positions on the sky. A cone search service (Kent & Plante 2008) can be written in any language, with Java, C#, PHP, and Perl being the most popular. In this example, we will utilize the Apache Tomcat server setup, MySQL database, and a Java servlet to make this cone search implementation.

Requirements

The following list of components is needed to complete the cone search implementation successfully.

Apache Tomcat server – an implementation to run locally on a machine. When the implementation is placed on a live server, one can use Apache or IIS (for Windows).

Java Development Kit (JDK 1.5) –the code provided has been tested with Java 1.5. This code will read the data from the database, and actually perform the cone search on the data. The file will be compiled using Apache Ant, and deployed as a Java servlet.

MySQL (version 5.0) – a relational database provided to hold the data and table.

MySQL JDBC connector – a Java JAR file library used to allow Java to connect to the database.

Web Server configuration – a configuration script is provided with the software distribution, and is used in this chapter as starttomcat, stoptomcat, and bouncetomcat.

The Sample Data Set

A sample comma-separated value table is provided, utilizing data from the Cornell Digital HI Archive (Springob et al. 2005b). The data contains a collection of 9000 homogeneously reduced HI detections from extragalactic sources out to cz 28,000 km/s. The catalog provided contains the named identifier from the Arecibo General Catalog (AGC), the Right Ascension and Declination (epoch J2000), and the heliocentric velocity in km/s. The full data set can be accessed via a web form (and a cone search) at: http://arecibo.tc.cornell.edu/hiarchive/.

MySQL Database

MySQL is a relational database implementation for Linux, Windows, and Mac OS X under GPL. Other database systems may be substituted for your cone search service, including PostgreSQL and Microsoft SQL Server. The table schema will need little to no modification to work with these database implementations. MySQL will be manipulated here on the command line, however, many GUIbased front-end packages, including PHP-MyAdmin (server-based) and MySQLFront (Windows commercial program), can be used to create the database and tables and import the data set. Refer to the SQL discussion (McGlynn & Nieto-Santisteban 2008) for related information on command line usage and queries. The first step involves starting the MySQL daemon with the command:

```
> mysqld
```

This will start MySQL in the background. Next, login to MySQL (we'll use the root account for simplicity, but you would not want to do this a live server) - on Windows:

```
> MySQL 5.0\bin\mysql -u root
```

Or, on UNIX/Mac OS:

```
> mysql -u root
```

First, create a database called nvoss, and select it to be used:

```
msyql> create database nvoss;
Query OK, 1 row affected (0.04 sec)

mysql> use nvoss;
Database changed
```

Create a table called galaxies within the database nvoss (note that decl is used instead of dec, as dec is reserved in most SQL implementations),

```
mysql> create TABLE galaxies (
mysql> agcnumber int NOT NULL,
mysql> ra double,
mysql> decl double,
mysql> velocity int);
```

Check the table schema via the command:

```
mysql> describe galaxies;
```

There are different ways of getting data into the table depending on the SQL implementation that one uses. Using a comma-separated value ASCII file is usually easiest. A convenient way to load the data is via:

```
mysql> load data infile '$NVOSS_HOME/java/data/agcgalaxies.csv' into
table galaxies fields terminated by ',';
```

One can now issue a simple SQL query at the prompt to examine the data:

```
mysql> SELECT * from galaxies;
```

See the SQL discussion for details on creating a table schema (McGlynn & Nieto-Santisteban 2008).

Web Server

The first step is to test that the Tomcat implementation provided in the software release works. We should check that the environment variable CATALINA_HOME has been set – on Windows:

```
> dir "%CATALINA_HOME%"
```

Or, on UNIX/Mac OS:

```
> ls $CATALINA_HOME
```

If that returns a listing we should be able to use the script in the $NVOSS_HOME/bin directory to start Tomcat:

```
> starttomcat
```

This will fail if Tomcat is already running on the port. The port is set in the server.xml file in the conf directory under $CATALINA_HOME. The default is 8080 - but you may change it. As a reminder, there are additional utilities for managing the server. Issue the command bouncetomcat to stop and restart the server, or stoptomcat to stop the server. If you are having a service error, it may be due to a bad reset or not waiting for the server to complete initialization. In the case of error, sometimes try to reset the server using the utilities provided making sure you allow a few seconds for the initialization to complete. The Tomcat server may be verified by typing the URL http://localhost:8080/ into a web browser.

Java Server Pages (JSP)

JSP is a very quick way to develop highly functional web pages. Effectively each page becomes a Java class (a servlet) that is compiled once by the server. When coding in JSP we may intermix Java code with actual output such as XML or HTML to create our pages. The .NET framework also now provides a facility like this in its ASPX pages. The input to the service itself is relatively simple. Effectively the cone search service is a web application that takes 3 parameters: right ascension, declination, and a search radius. It then needs to do a lookup using this information and provide the answer in a VOTABLE. An HTTP GET request to a cone service should look like

```
coneserviceURL?RA=108&DEC=1.5&SR=0.5
```

An easy way to do this would be to make a simple JSP page and have it pull these parameters from the request. Such a page is provided in the software distribution package in $NVOSS_HOME/java/src/coneserver/coneShell.jsp. Let's walk through the code before we deploy it. This is a nice easy JSP so for deployment all we need to do is copy it to a web directory. The default root of the Tomcat installation is in the webapps/ROOT directory so copy it to the root directory – on Windows:

```
> copy coneShell.jsp "%WEB_DEPLOY%"\ROOT
```

Or, on UNIX/Mac OS:

```
> cp coneShell.jsp $WEB_DEPLOY/ROOT
```

If you have sourced the software setup, then this will be available at:

```
http://localhost:8080/coneShell.jsp?SR=1&DEC=180&RA=1
```

There are no data yet -this will be included in the next section.

Using the Java Code

The provided coneserver Java code uses the package sumsch. In addition, it requires the Java SQL libraries to access the MySQL database. The VOTWrap class is used to instantiate and manipulate the VOTable (Fitzpatrick 2008). The Java code with the associated methods for this exercise can be found in $NVOSS_HOME/java/src/coneserver/src/sumsch/VOTCone.java.

The database is queried, and returned objects are written to a VOTable file. The class VOTCone calls the IVOA VOTWrap search method that will determine the angular distance between the position passed to the cone search (using the Java distance method), and an object within the table along a great circle. Those objects are returned to the Java server page and displayed in XML. The coneserver software uses Apache Ant for compilation, with build.xml being used to define any dependencies. The next step is to switch to the main coneserver directory and build the coneserver servlet:

```
> cd $NVOSS_HOME/java/src/coneserver
> ant compile
```

A simple ant test can now be run, which will return messages establishing a connection and termination to MySQL:

```
> ant test
```

The final step is to deploy the module to the server, also by using ant. First, a small modification needs to be made to the web.xml configuration file located in $NVOSS_HOME/java/src/coneserver/conf/. The env-entry value needs to be changed to the $NVOSS_HOME/java/data/ directory where the value of the NVOSS_HOME environment variable needs to be stated explicitly:

```
<?xml version="1.0" encoding="ISO-8859-1"?>
<!DOCTYPE web-app
PUBLIC "-//Sun Microsystems, Inc.//DTD Web Application 2.3//EN"
"http://java.sun.com/dtd/web-app_2_3.dtd">
<web-app>
```

```
<env-entry>
<env-entry-name>dataPath</env-entry-name>
<env-entry-type>java.lang.String</env-entry-type>
<env-entry-value>/nvoss2006/java/data/</env-entry-value>
</env-entry>
</web-app>
```

Return to the coneserver directory, and deploy the servlet:

```
> ant deploy
```

A.3.2 Testing and Returning the XML VOTable

The coneserver module will be deployed to $CATALINA_HOME/webapps/ROOT/cone/. A test URL can be used to search for galaxies within a two-degree radius in the vicinity of the Virgo Cluster. Use the URL:

```
http://localhost:8080/cone/cone.jsp?RA=180&DEC=12&SR=2
```

This will return the file header, object numbers, coordinates, and heliocentric velocities from the catalog that matches the criteria. Depending on your web browser, the raw XML or a plain HTML-style table may be displayed. A further shell can be created to read the XML and display the table in a nicer format. The cone search server can now be accessed via any valid cone search client application (Kent 2008; Tody & Fitzpatrick 2008).

As the cone server is now running on your machine, you can use a client application to access the cone search service. Any client application in any language on any platform will work. The Python cone search client located in $NVOSS_HOME/python/samples/ConeSearchEx.py uses the class ConeSearch.py. Other cone search clients can be found in the previous section

```
> python ConeSearchEx.py coneSearchRaw
http://localhost:8080/cone/cone.jsp 180.0 12.5 2.0 1
```

Finally, one can validate a live cone search service with the NCSA Cone Search Validator. This will send three tests to the service – a standard input, a user error input, and a metadata query. Results, errors, and recommendations to your service will be made based on the results sent from the service.

A.4 4. Building a Simple SIAP Service

This section will give an example of how to build a service around an archive of images using the Simple Image Access Protocol (SIAP). The different image service types and basic requirements for user input using a HTTP GET request will be described. The metadata requirements will be discussed. The service will return a VOTable and options for several different image formats, including FITS and JPEG.

A.4.1 The Simple Image Access Protocol

Many astronomical archives provide not only cataloged measurements, but two-dimensional images from various spectral bands and position information on those im-

ages as well. The Simple Image Access Protocol (SIAP; Kwok & Tody 2008b) provides a bridge between client applications and imaging services. The specification can be found in the IVOA documentation. In short, a user can query the service through a simple HTTP GET request and be given a VOTable listing of images and formats that meet the search criteria. Different types of image services exist, with different purposes and levels of complexity. The four basic types into which most image services will fall are described below:

1. **Image Cutout** – Provides smaller, unmodified images from a larger subset of a sky survey
2. **Image Mosaicking** – More complex service that provides the ability to resample and reproject data into larger images
3. **Atlas** – Images are of a precomputed size, and are not dynamically created cutouts
4. **Pointed Image** – Smaller resources that large sky surveys that target specific regions of sky, e.g. HII regions in a particular galaxy

A.4.2 Basic Input Parameters and Output

A SIAP service provides an image query web method such that one can search for imaging data within a region of sky. The simplest example of using SIAP to obtain a list of images uses the following HTTP GET request:

```
http://URL_to_service/siap.jsp?POS=187.5,12.5&SIZE=0.1
```

This request illustrates two parameters the service must have in order to specify a region of interest. The central coordinates of the region are given as the POS parame-

ter – the Right Ascension and Declination in decimal degrees, delimited by a comma. The SIZE parameter describes the angular size of the region of interest, also in decimal degrees, as a scalar, or as two comma-separated parameters for each axis (e.g. SIZE=0.1,0.2). Together, these parameters give the service a rectangular region of sky to search.

The service returns a VOTable with data entries meeting the criteria, including URLs to the imaging service that will yield images of various types (FITS, JPEG, GIF) that can be accessed from the imaging service. Each row entry in the VOTable will give access to an image.

A.4.3 Other Service Input Parameters

A SIAP service is not limited to the basic POS and SIZE parameters in the web request. With the exception of INTERSECT, FORMAT, and VERB, the parameters listed below will generally be used with a cutout or mosaicking service:

1. INTERSECT – Describes whether images could COVER the entire region, be entirely ENCLOSED, overlap the CENTER of the region, or OVERLAP (default) some part of the region.
2. NAXIS – Supported by a cutout service, this specifies the image size in pixels as a vector (NAXIS=256,512).
3. CFRAME – Coordinate reference frame. Default is ICRS.
4. EQUINOX – Equinox for reference frame specified in CFRAME. J2000 by default.
5. CRPIX – Coordinates of the reference pixel –the image center by default.

6. CRVAL – WCS relative to the CFRAME parameter at the reference pixel.
7. CDELT – Image scale of the image in degrees per pixel, with negative values indicating an axis flip.
8. ROTANG – Image rotation relative to the reference frame defined in CFRAME.
9. PROJ – Three character code for the image projection – same as the FITS WCS, with the default value set as TAN.
10. FORMAT – The service must support this parameter that describes the image formats.
11. VERB – Verbosity value specifying the number of columns to be returned.

A.4.4 VOTable Output

The XML VOTable provides a listing of images that meet the criteria defined by the query. Fields in the VOTable must contain a specific set of UCDs that correspond to data model attributes. Those parameters describe each image in the table, as shown in the listing below:

1. VOX:Image_Title – Short description of image, source, observation
2. INST_ID – Instrument used for the observation
3. VOX:Image_MJDateObs – Mean modified Julian date of the image
4. POS_EQ_RA_MAIN – J2000 Right Ascension of the image center
5. POS_EQ_DEC_MAIN – J2000 Declination of the image center
6. VOX:Image_Naxes – Integer number of image axes
7. VOX:Image_Naxis – Integer length in pixels of each image axis

8. VOX:Image_Scale – Scale of each axis in degrees per pixel
9. VOX:Image_Format – MIME type of the object associated with the image
10. VOX:Image_AccessReference – The service must support this parameter
11. VERB – Verbosity value specifying the number of columns to be returned

A.4.5 Setting up the SIAP Service

The SIAP service is very similar in nature to that of the cone search (Kent & Greene 2008). Requirements extend to having a source of images and data to describe those images and fill in the metadata. In this scenario, the MySQL database will be used as this source. The following list of components is needed to complete the SIAP implementation successfully. This list mimics that in the cone search section

Apache Tomcat server – an implementation to run locally on a machine. When the implementation is placed on a live server, one can use Apache or IIS (for Windows)

Java Development Kit (JDK 1.5) – the code provided has been tested with Java 1.5. This code will read the metadata from the database, and actually finds what images meet the search criteria. The file will be compiled using Apache Ant, and deployed as a Java servlet.

MySQL (version 5.0) – a relational database provided to hold the database and table.

MySQL JDBC connector – a Java JAR file library used to allow Java to connect to the database.

Web Server configuration – a configuration script is provided with the software distribution, and is used in this section as starttomcat, stoptomcat, and bouncetomcat.

A.4.6 The Imaging Data Set

For this tutorial, a small atlas set of 178 S0 galaxies will be used as the imaging service. The images are six arcminute cutouts from the 2nd generation Digital Sky Survey blue plates, provided in both FITS and JPEG format. In addition, the UCD values are provided in a comma-separated value file, which will be read into the database in the next section.

A.4.7 Setting up the Database

Starting up MySQL is exactly the same as in the cone search tutorial ([ref cone search database]). The first step involves starting the MySQL daemon with the command – on Windows:

```
> mysqld
```

This will start MySQL in the background. Next, login to MySQL (we'll use the root account for simplicity, but again, you would not want to do this to a live server):

```
> MySQL 5.0\bin\mysql -u root
```

Or, on UNIX/Mac OS:

```
> mysql -u root
```

Please refer to the SQL discussion for details on navigating through databases and tables (McGlynn & Nieto-Santisteban 2008). First, create a database called nvoss, and select it to be used:

```
msyql> create database nvoss;
Query OK, 1 row affected (0.04 sec)
mysql> use nvoss;
Database changed
```

Create a simple table called galaxyimages within the database nvoss (note that decl is used instead of dec, as dec is reserved in most SQL implementations),

```
mysql> create TABLE galaxyimages (
mysql> entrynum int
mysql> agcnumber int NOT NULL,
mysql> ra double,
mysql> decl double,
mysql> inst\_id char,
msyql> image\_mjdateobs float,
mysql> image\_naxes longint,
mysql> image\_naxis\_x longint,
msyql> image\_naxis\_y longint,
mysql> image\_scale\_x double,
mysql> image\_scale\_y double,
mysql> image\_format char,
mysql> image\_accessreference char);
```

Check the table schema via the command:

```
mysql> describe galaxyimages;
```

There are different ways of getting data into the table depending on the SQL implementation that one uses. Using a comma-separated value ASCII file is usually easiest. A convenient way to load the data is via:

```
mysql> load data infile '$NVOSS\_HOME/java/data/galaxyimagedata.csv'
into table galaxyimages fields terminated by ',';
```

One can now issue a simple SQL query at the prompt to examine the data:

```
mysql> SELECT * from galaxyimages;
```

Web Server

The web server setup is identical to that for the cone search service (Kent & Greene 2008). Verify that the CATALINA_HOME environment variable has been properly set:

```
> dir "%CATALINA_HOME%"
```

Or, on UNIX/Mac OS:

```
> ls $CATALINA_HOME
```

If that returns a listing we should be able to use our script in the bin directory to start Tomcat:

```
> starttomcat
```

This will fail if Tomcat is already running on the port. The port is set in the server.xml file in the conf directory under $CATALINA_HOME. The default is 8080 - but you may change it to another port. As a reminder, there are additional utilities for managing the server. Issue the command bouncetomcat to stop and restart the server, or stoptomcat to stop the server. If you are having a service error, it may be due to a bad reset or not waiting for the server to complete initialization. In the case of error, sometimes try to reset the server using the utilities provided making sure you allow a few seconds for the initialization to complete. The Tomcat server may be verified by typing the URL http://localhost:8080/ into a web browser.

Java Server Pages (JSP)

The SIAP service is a web application that takes 2 parameters: a two-element array consisting of right ascension and declination, and another parameter that gives the search area size. It then needs to do a lookup using this information and provide the answer in a VOTable. A call to a SIAP service should look like

```
siapserviceURL?POS=180.5,12,7&SIZE=0.5
```

The service created in this tutorial will be available at:

```
http://localhost:8080/siap/siap.jsp?
```

Using the Java Code

The siapserver Java code provided in the software distribution uses the package sumsch. It is similar in implementation to the coneserver and can be found in the directory:

```
$NVOSS_HOME/java/src/siapserver/src/sumsch/VOTSiap.java
```

The database is queried, and returned objects are written to a VOTable file. The class VOTSiap calls the IVOA VOTWrap search method that will determine the angular distance between the position passed to the SIAP search (using the Java distance method), and an object within the table along a great circle. Those objects are returned to the Java server page and displayed in XML. Like most of the Java code, the siapserver software uses Apache Ant for compilation, with build.xml being used to define any dependencies. The next step is to switch to the main $NVOSS_HOME/java/src/siapserver directory and build the siapserver servlet:

```
> cd $NVOSS_HOME/java/src/siapserver
> ant compile
```

We can now run a simple ant test, which will return messages establishing a connection and termination to MySQL:

```
> ant test
```

The final step is to deploy the module to the server, also by using ant. First, a small modification needs to be made to the web.xml configuration file located in $NVOSS_HOME/java/src/siapserver/conf/. The env-entry value needs to be changed to the Java data directory:

```
<?xml version="1.0" encoding="ISO-8859-1"?>
<!DOCTYPE web-app
PUBLIC "-//Sun Microsystems, Inc.//DTD Web Application 2.3//EN"
"http://java.sun.com/dtd/web-app_2_3.dtd">
<web-app>
<env-entry>
<env-entry-name>dataPath</env-entry-name>
<env-entry-type>java.lang.String</env-entry-type>
<env-entry-value>/nvoss2006/java/data/</env-entry-value>
</env-entry>
</web-app>
```

Return to the siapserver directory, and deploy the servlet:

```
> ant deploy
```

A.4.8 Testing and Returning the XML VOTable

The server module will be deployed to $CATALINA_HOME/webapps/ROOT/siap/. In addition, the JPEG and FITS images need to be copied to the server directory, as the URL entries in the database are specific to this local server demonstration. On Windows:

```
> cd "%CATALINA_HOME%\webapps\ROOT\siap%"
> mkdir jpeg
> mkdir fits
> copy %NVOSS_HOME/java/data/images/*.fits
```

```
%CATALINA_HOME/webapps/ROOT/siap/fits/.
> cp %NVOSS_HOME/java/data/images/*.jpeg
%CATALINA_HOME/webapps/ROOT/siap/jpeg/.
```

or on UNIX/Mac OS:

```
> cd $CATALINA_HOME/webapps/ROOT/siap/
> mkdir jpeg
> mkdir fits
> cp $NVOSS_HOME/java/data/images/*.fits
$CATALINA_HOME/webapps/ROOT/siap/fits/.
> cp $NVOSS_HOME/java/data/images/*.jpeg
$CATALINA_HOME/webapps/ROOT/siap/jpeg/.
```

A test URL can be used to search for galaxies within a ten degree box (since this atlas of images is rather sparse on the sky)

```
http://localhost:8080/siap/siap.jsp?POS=187.5,12.5&SIZE=5.0
```

This will return the file header, object numbers, coordinates, and all metadata for each image than meets the search criteria. Depending on your web browser, the raw XML or a plain HTML-style table may be displayed. A further shell can be created to read the XML and display the table in a nicer format. The SIAP server can now be accessed via any valid SIAP client application (Kwok & Tody 2008a).

A.5 Combining VO Services in a Data Reduction and Visualization Environment

An example case study using VO standards, technology, and libraries will be described using a large extragalactic radio survey. The Arecibo Legacy Fast ALFA extragalactic HI survey, conducted with Arecibo's new multi-beam *L*-band receiver system, benefits from fast access to multi-wavelength data sets provided by VO technologies. Examples of implementing existing libraries into a data reduction pipeline/ visualization package will be shown. Survey participants use the tools for access to catalogs and imaging from predetermined resources, but also have the ability to import or query for their own. The tools make use of the VO IDL libraries available in the software distribution.

A.5.1 Implementing the VO into a Large Scale Survey

As astronomy moves into a new paradigm of full sky surveys at all wavelengths with ever expanding data sets, the foundations created with Virtual Observatory technology will help to correlate the vast results with hundreds of astronomical databases. Clearly cross correlation and mining of archival data sets will be of great importance to astronomical research, however, current data reduction pipelines can also benefit by integrating VO tools into software packages. Real-time querying of data archives allows users to interpret results quickly, yielding a faster turn around time for science results and potential follow-up targets.

The ongoing ALFALFA survey greatly benefits from the VO paradigm in delivering data products and catalogs to the astronomical community in a timely manner. The ALFALFA data reduction pipeline used to analyze Level I (radio interference flagging)

and Level II (data cubes and signal extraction) data products is written in the Interactive Data Language (see Chapter 2). The environment provides large libraries well suited for numerical analysis and manipulation of large matrices. IDL also contains support for XML and VO protocols and standards can be easily implemented, as has been done with the ALFALFA data pipeline. ALFALFA data cubes are 2.4 by 2.4 degrees on the sky, by 5000 km/s in *cz* space, and occupy a disk space of 380 MB. In addition to the spectral information, the data cube files contain spectral weights, continuum maps, and cube makeup information from original data files. The following Virtual Observatory resources are used within the data cube visualization environment.

VOTable - downloaded and user-provided XML files with minimum columns of type meta.id, pos.eq.ra.main, pos.eq.dec.main (just as in a response from a cone call) can be overlaid on the sky maps.

Registry Search - users from the research team can query for resources for different online resources

Cone Search - search pre-selected cone search resources and return results SIAP - fetch images from DSS 2, SDSS, 2MASS, and NVSS cutouts of a specified size.

Integrating these protocols and libraries into our existing software environment required having IDL 6+, Java 1.5, and the IDL User's Library.

A.5.2 Example GUI for SIAP

The code below outlines a few simple ways of getting images into IDL. It makes use of procedures from the IDL User's Library, and is used in the GUI procedure provided in the software distribution. The code is not meant to be used as a stand-alone procedure

as it is presented below, but more of a schematic for first time users.

```
;Sample code for gaining access to images from the DSS using queryDSS
;and a simple WGET to access the Sloan Digital Sky Survey cutouts.
;Obtain the image size and central coordinates
;from user input or a GUI text window
```

First, an image center and size are defined with three variables. In the GUI procedure, these are the inputs, with an image default of six arcminutes.

```
;Coordinate center for the image - units of decimal hours
; and decimal degrees

rahr = 12.5
decdeg = 12.5
Combining VO Services 329
imagesize = 10.0 ; Image size in arcminutes
```

Next, an IDL User's Library procedure, queryDSS is used to retrieve the image and associated FITS header. We will default to the 2nd Digital Sky Survey Blue plates, but other other options are available as well. In addition, we perform a simple re-gridding of the image to 210 by 210 pixels, and store it in a previously created state structure (only necessary in the GUI version).

```
;OBTAIN AN IMAGE FROM THE DSS 2 BLUE SURVEY
queryDSS, [rahr*15.0,decdeg], image, header, $
imsize=imagesize, survey='2b'
state.dssimage=congrid(image, 210,210)
```

SDSS optical images can be retrieved from their web service via the wget command in UNIX or Mac OS X, and read into IDL environment with the native command READ_JPEG.

```
;Check for OS family, works with Linux or Max OS X
osfamily = strupcase(!version.os_family)
if (osfamily eq 'UNIX') then begin
;SIMPLE METHOD FOR ACCESSING SDSS JPEG CUTOUTS - inverted negative
;images from the CASJOBS server
url='http://casjobs.sdss.org/ImgCutoutDR4/getjpeg.aspx?ra='+$
strcompress(rahr*15.0, /remove_all)+$
'&dec='+strcompress(decdeg, /remove_all)+$
'&scale='+strcompress(imagesize/6.67,/remove_all)+$
'&opt=GI&width=400&height=400'
;Temporary file storage in the user's home directory
filename='~/idl_temp.jpg'
;Use the WGET command to save image as a temporary file
spawn, 'wget -q -O '+ filename + " '" + url + "'"
;Use the native IDL procedure READ_JPEG to read in the file
;Note that the image is stored
read_jpeg, filename, imagesdss, true=1
;Remove the temporary file
spawn, '/bin/rm -r ~/idl_temp.jpg'
endif
;USE SIAP TO ACCESS IMAGES
;Refer to the IDL section
;for more information on specific
```

```
;IDL related access to VO services. This simple example will
;return FITS images to the current working directory.

siapcall, str=siapresult, 217.5,35.0, 0.16,$
url="http://irsa.ipac.caltech.edu/cgi-bin/2MASS/IM/nph-
+$im_sia?type=ql&ds=asky", root='2mass'

;Any display routines can be now be used to show the images, for
;example:
> tvscl, imagedss
> tv, imagesdss, /true
```

Methods used in the above code can be wrapped into an example GUI application, shown in Figure A.2. The GUI is included in the software distribution for illustrative purposes in the IDL $NVOSS_HOME/idl/gui directory and may be incorporated into larger data reduction schemes.

A.5.3 Usage in the ALFALFA Visualization Environment

Many of the VO components and applications mentioned have been integrated into a custom written application called *GRID*View. *GRID*View was developed for the ALFALFA project for the purpose of viewing three-dimensional data cubes in the IDL environment. As shown in Figure A.3, users can cut the cube at specific *cz* values and view sky maps and the spectral weights that apply to that area. Once sources are identified, users can overlay catalogs in real time and access images from multiple surveys. The image viewing application GUI for this article as an example in section 2 is also

implemented in the GRIDview application. Access to images and catalog information at a rapid rate has greatly increased optical counterpart identification of sources in the ALFALFA survey. Survey participants are heavy end users of the VO and the tools that take advantage of the protocols. In addition, catalogs and extracted measurements can be distributed to follow- up websites for review by team members.

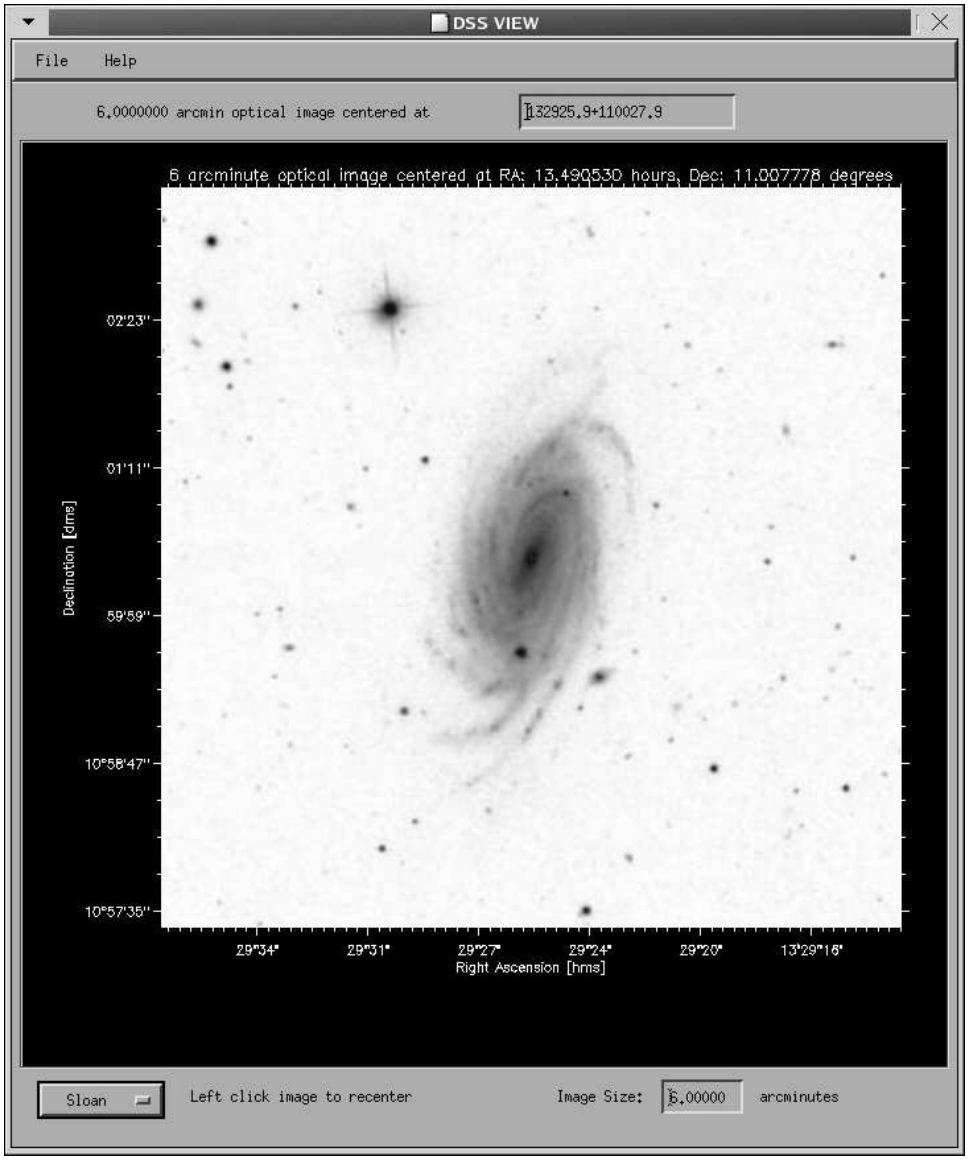

Figure A.2: Example GUI application built in IDL to access image cutouts from both the Digital Sky Survey(Lasker et al. 1990) and SDSS(York et al. 2000). The galaxy shown in UGC 8475.

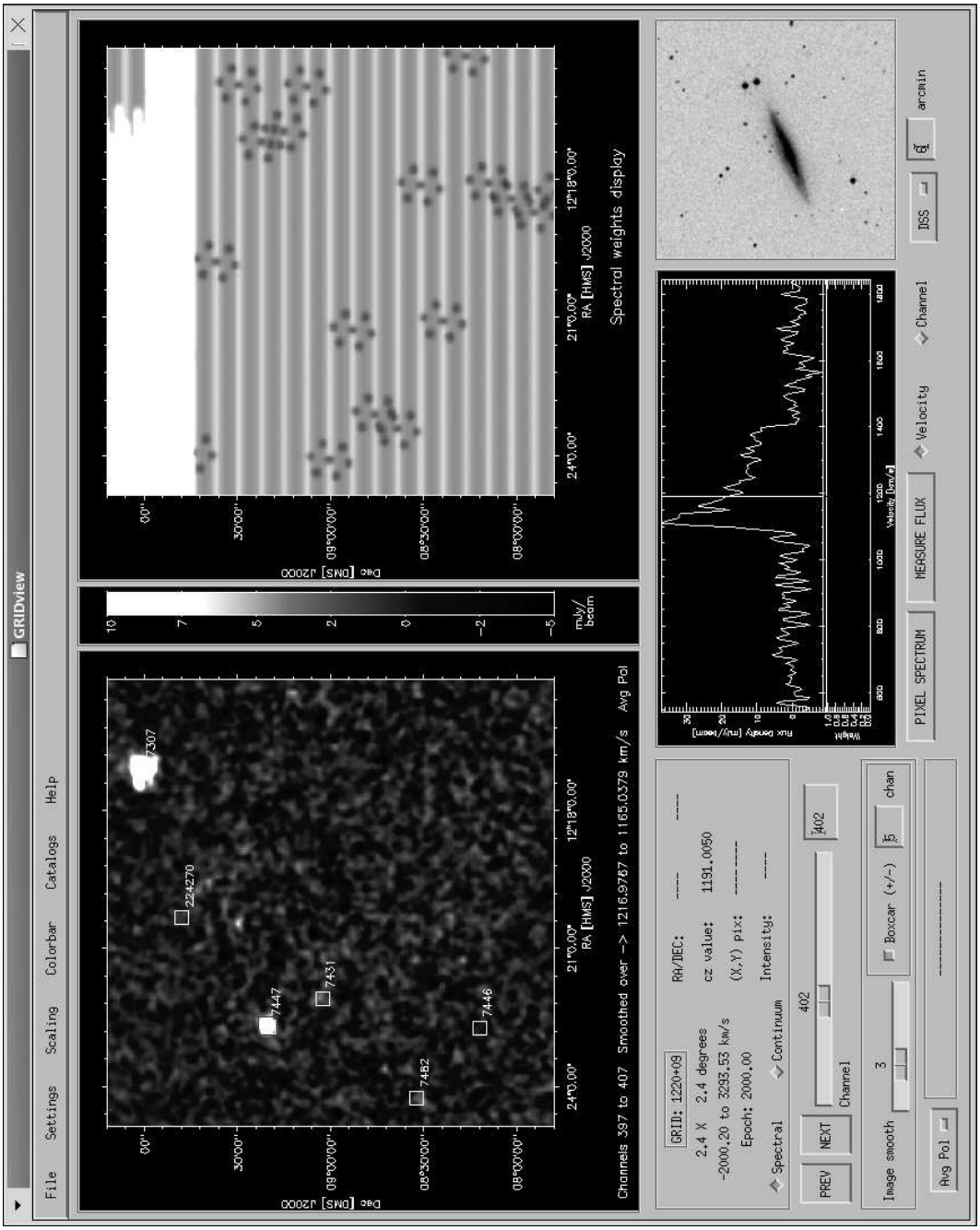

Figure A.3: GRIDview application GUI created in IDL. The data cube visualization procedure incorporates various VO protocols for use during the data analysis process. The figure shows both optical image viewing and catalog overlay on the radio data. Users can manipulate the cube with various GUI controls, export maps, and examine a one-dimensional spectrum from any cube pixel.

REFERENCES

Abell, G. O. 1975, Clusters of Galaxies (Galaxies and the Universe), 601

Allen, R. J. 1968, Nature, 220, 147

Auld, R., Minchin, R. F., Davies, J. I., Catinella, B., van Driel, W., Henning, P. A., Linder, S., Momjian, E., Muller, E., O'Neil, K., Sabatini, S., Schneider, S., Bothun, G., Cortese, L., Disney, M., Hoffman, G. L., Putman, M., Rosenberg, J. L., Baes, M., de Blok, W. J. G., Boselli, A., Brinks, E., Brosch, N., Irwin, J., Karachentsev, I. D., Kilborn, V. A., Koribalski, B., & Spekkens, K. 2006, Mon. Not. R. Astron. Soc., 371, 1617

Baade, W. 1956, Astrophys. J., 123, 550

Baldwin, J. E. & Smith, F. G. 1956, The Observatory, 76, 141

Balkowski, C., Chamaraux, P., & Fontanelli, P. 1985, in The Virgo Cluster of Galaxies, 37–43

Barnes, D. G., Staveley-Smith, L., de Blok, W. J. G., Oosterloo, T., Stewart, I. M., Wright, A. E., Banks, G. D., Bhathal, R., Boyce, P. J., Calabretta, M. R., Disney, M. J., Drinkwater, M. J., Ekers, R. D., Freeman, K. C., Gibson, B. K., Green, A. J., Haynes, R. F., te Lintel Hekkert, P., Henning, P. A., Jerjen, H., Juraszek, S., Kesteven, M. J., Kilborn, V. A., Knezek, P. M., Koribalski, B., Kraan-Korteweg, R. C., Malin, D. F., Marquarding, M., Minchin, R. F., Mould, J. R., Price, R. M., Putman, M. E., Ryder, S. D., Sadler, E. M., Schröder, A., Stootman, F., Webster, R. L., Wilson, W. E., & Ye, T. 2001, Mon. Not. R. Astron. Soc., 322, 486

Baugh, C. M. 2006, Reports of Progress in Physics, 69, 3101

Bell, E. F., McIntosh, D. H., Katz, N., & Weinberg, M. D. 2003, Astrophys. J., Suppl. Ser., 149, 289

Belokurov, V., Zucker, D. B., Evans, N. W., Gilmore, G., Vidrih, S., Bramich, D. M., Newberg, H. J., Wyse, R. F. G., Irwin, M. J., Fellhauer, M., Hewett, P. C., Walton, N. A., Wilkinson, M. I., Cole, N., Yanny, B., Rockosi, C. M., Beers, T. C., Bell, E. F., Brinkmann, J., Ivezić, Ž., & Lupton, R. 2006a, Astrophys. J., Lett., 642, L137

Belokurov, V., Zucker, D. B., Evans, N. W., Wilkinson, M. I., Irwin, M. J., Hodgkin, S., Bramich, D. M., Irwin, J. M., Gilmore, G., Willman, B., Vidrih, S., Newberg, H. J., Wyse, R. F. G., Fellhauer, M., Hewett, P. C., Cole, N., Bell, E. F., Beers, T. C., Rockosi, C. M., Yanny, B., Grebel, E. K., Schneider, D. P., Lupton, R., Barentine, J. C., Brewington, H., Brinkmann, J., Harvanek, M., Kleinman, S. J., Krzesinski, J., Long, D., Nitta, A., Smith, J. A., & Snedden, S. A. 2006b, Astrophys. J., Lett., 647, L111

Bennett, A. S. 1962, Mem. R. Astron. Soc., 68, 163

Berriman, G. B., Deelman, E., Good, J. C., Jacob, J. C., Katz, D. S., Kesselman, C., Laity, A. C., Prince, T. A., Singh, G., & Su, M.-H. 2004, in Presented at the Society of Photo-Optical Instrumentation Engineers (SPIE) Conference, Vol. 5493, Optimizing Scientific Return for Astronomy through Information Technologies. Edited by Quinn, Peter J.; Bridger, Alan. Proceedings of the SPIE, Volume 5493, pp. 221-232 (2004)., ed. P. J. Quinn & A. Bridger, 221–232

Berriman, G. B., Good, J. C., Laity, A. C., Prince, T. A., Jacob, J. C., Katz, D. S., Deelman, E., Singh, G., Su, M.-H., & Kesselman, C. 2006, The Virtual Observatory in Action: New Science, New Technology, and Next Generation Facilities, 26th meeting of the IAU, Special Session 3, 17-18, 21-22 August, 2006 in Prague, Czech Republic, SPS3, #52, 3

Berriman, G. B., Laity, A. C., Good, J. C., Katz, D. S., Jacob, J. C., Deelman, E., Singh, G., Su, M.-H., & Prince, T. A. 2007, Highlights of Astronomy, 14, 621

Binggeli, B., Popescu, C. C., & Tammann, G. A. 1993, Astron. Astrophys. Suppl. Ser., 98, 275

Binggeli, B., Sandage, A., & Tammann, G. A. 1985, Astron. J, 90, 1681

Binggeli, B., Tammann, G. A., & Sandage, A. 1987, Astron. J, 94, 251

Blumenthal, G. R., Faber, S. M., Primack, J. R., & Rees, M. J. 1984, Nature, 311, 517

—. 1985, Nature, 313, 72

Boselli, A., Boissier, S., Cortese, L., & Gavazzi, G. 2008, Astrophys. J., 674, 742

Bottinelli, L. & Gouguenheim, L. 1974, Astron. Astrophys., 36, 461

Bottinelli, L., Gouguenheim, L., & Heidmann, J. 1973, Astron. Astrophys., 25, 451

Bradt, H., Mayer, W., Naranan, S., Rappaport, S., & Spada, G. 1967, Astrophys. J., Lett., 150, L199+

Branchini, E., Teodoro, L., Frenk, C. S., Schmoldt, I., Efstathiou, G., White, S. D. M., Saunders, W., Sutherland, W., Rowan-Robinson, M., Keeble, O., Tadros, H., Maddox, S., & Oliver, S. 1999, Mon. Not. R. Astron. Soc., 308, 1

Braun, R., Thilker, D., & Walterbos, R. A. M. 2003, Astron. Astrophys., 406, 829

Bregman, J. N. & Roberts, M. S. 1990, Astrophys. J., 362, 468

Briggs, F. H. 1990, Astron. J, 100, 999

Burbidge, G. R. 1956, Astrophys. J., 124, 416

Cayatte, V., Kotanyi, C., Balkowski, C., & van Gorkom, J. H. 1994, Astron. J, 107, 1003

Cayatte, V., van Gorkom, J. H., Balkowski, C., & Kotanyi, C. 1990, Astron. J, 100, 604

Chamaraux, P., Balkowski, C., & Gerard, E. 1980, Astron. Astrophys., 83, 38

Chengalur, J. N., Giovanelli, R., & Haynes, M. P. 1995, Astron. J, 109, 2415

Chung, A., van Gorkom, J. H., Kenney, J. D. P., & Vollmer, B. 2007, Astrophys. J., Lett., 659, L115

Chynoweth, K. M., Langston, G. I., Yun, M. S., Lockman, F. J., Rubin, K. H. R., & Scoles, S. A. 2008, Astron. J, 135, 1983

Cole, S., Lacey, C. G., Baugh, C. M., & Frenk, C. S. 2000, Mon. Not. R. Astron. Soc., 319, 168

Condon, J. J., Cotton, W. D., Greisen, E. W., Yin, Q. F., Perley, R. A., Taylor, G. B., & Broderick, J. J. 1998, Astron. J, 115, 1693

Connors, T. W., Kawata, D., & Gibson, B. K. 2006, Mon. Not. R. Astron. Soc., 371, 108

Cornett, R. H. & Smith, A. M. 1981, Astronomical Data Center Bulletin, 1, 78

Cortés, J. R., Kenney, J. D. P., & Hardy, E. 2006, Astron. J, 131, 747

Cortés-Medellin, G. 2002, NAIC Internal Memorandum 02-08

Côté, P., Blakeslee, J. P., Ferrarese, L., Jordán, A., Mei, S., Merritt, D., Milosavljević, M., Peng, E. W., Tonry, J. L., & West, M. J. 2004, Astrophys. J., Suppl. Ser., 153, 223

Cowie, L. L. & McKee, C. F. 1977, Astrophys. J., 211, 135

Cowie, L. L. & Songaila, A. 1977, Nature, 266, 501

Davies, J., Minchin, R., Sabatini, S., van Driel, W., Baes, M., Boyce, P., de Blok, W. J. G., Disney, M., Evans, R., Kilborn, V., Lang, R., Linder, S., Roberts, S., & Smith, R. 2004, Mon. Not. R. Astron. Soc., 349, 922

Davies, J. I., Disney, M. J., Minchin, R. F., Auld, R., & Smith, R. 2006, Mon. Not. R. Astron. Soc., 368, 1479

Davies, J. I., Roberts, S., & Sabatini, S. 2005, Mon. Not. R. Astron. Soc., 356, 794

Davies, R. D. 1968, Observatory, 88, 196

Davies, R. D., Gottesman, S. T., Reddish, V. C., & Verschuur, G. L. 1963, The Observatory, 83, 245

Davies, R. D. & Lewis, B. M. 1973, Mon. Not. R. Astron. Soc., 165, 231

de Vaucouleurs, G. 1961, Astrophys. J., Suppl. Ser., 6, 213

—. 1975, Social Studies of Science, 9, 557

de Vaucouleurs, G., Angione, R., & Fraser, C. W. 1968, Astrophysical Letters, 2, 141

di Serego Alighieri, S., Gavazzi, G., Giovanardi, C., Giovanelli, R., Grossi, M., Haynes, M. P., Kent, B. R., Koopmann, R. A., Pellegrini, S., Scodeggio, M., & Trinchieri, G. 2007, Astron. Astrophys., 474, 851

Dickey, J. M., Hanson, M. M., & Helou, G. 1990, Astrophys. J., 352, 522

Dieter, N. H. 1958, Astron. J, 63, 49

—. 1962a, Astron. J, 67, 313

—. 1962b, Astron. J, 67, 317

—. 1962c, Astron. J, 67, 217

Djorgovski, S. 1990, Astron. J, 99, 31

Drake, F. D. 1971, in Bulletin of the American Astronomical Society, Vol. 3, Bulletin of the American Astronomical Society, 466

Dressler, A. 1980, Astrophys. J., 236, 351

Duc, P.-A. & Bournaud, F. 2008, Astrophys. J., 673, 787

Duprie, K. & Schneider, S. E. 1996, Astron. J, 112, 937

Ewen, H. I. & Purcell, E. M. 1951, Nature, 168, 356

Field, G. B. 1959a, Astrophys. J., 129, 525

—. 1959b, Astrophys. J., 129, 536

Fitzpatrick, M. J. 2008, in Astronomical Society of the Pacific Conference Series, Vol. 382, The National Virtual Observatory: Tools and Techniques for Astronomical Research, ed. M. J. Graham, M. J. Fitzpatrick, & T. A. McGlynn, 363–374

Frenk, C. S., White, S. D. M., Efstathiou, G., & Davis, M. 1985, Nature, 317, 595

Freudling, W., Staveley-Smith, L., Calabretta, M., Catinella, B., van Driel, W., Linder, S., Minchin, R., Momjian, E., Zwaan, M., & AUDS Team. 2005, in Bulletin of the American Astronomical Society, Vol. 37, Bulletin of the American Astronomical Society, 1316

Friedman, H. & Byram, E. T. 1967, Science, 158, 257

Fukugita, M., Okamura, S., & Yasuda, N. 1993, Astrophys. J., Lett., 412, L13

Gavazzi, G., Boselli, A., Donati, A., Franzetti, P., & Scodeggio, M. 2003, Astron. Astrophys., 400, 451

Gavazzi, G., Giovanelli, R., Haynes, M. P., Fabello, S., Fumagalli, M., Kent, B. R., Koopmann, R. A., Brosch, N., Hoffman, G. L., Salzer, J. J., & Boselli, A. 2008, Astron. Astrophys., 482, 43

Giovanardi, C., Helou, G., Salpeter, E. E., & Krumm, N. 1983, Astrophys. J., 267, 35

Giovanelli, R. 1985, in The Virgo Cluster of Galaxies, 67–70

Giovanelli, R. & Haynes, M. P. 1983, Astron. J, 88, 881

—. 1988, Extragalactic Neutral Hydrogen (Galactic and Extragalactic Radio Astronomy (2nd Edition))

—. 1989, Astrophys. J., Lett., 346, L5

—. 1991, Ann. Rev. Astron. Astrophys., 29, 499

—. 2003, ALFALFA white paper

Giovanelli, R., Haynes, M. P., Kent, B. R., Perillat, P., Catinella, B., Hoffman, G. L., Momjian, E., Rosenberg, J. L., Saintonge, A., Spekkens, K., Stierwalt, S., Brosch, N., Masters, K. L., Springob, C. M., Karachentsev, I. D., Karachentseva, V. E., Koopmann, R. A., Muller, E., van Driel, W., & van Zee, L. 2005a, Astron. J, 130, 2613

Giovanelli, R., Haynes, M. P., Kent, B. R., Perillat, P., Saintonge, A., Brosch, N., Catinella, B., Hoffman, G. L., Stierwalt, S., Spekkens, K., Lerner, M. S., Masters, K. L., Momjian, E., Rosenberg, J. L., Springob, C. M., Boselli, A., Charmandaris, V., Darling, J. K., Davies, J., Lambas, D. G., Gavazzi, G., Giovanardi, C., Hardy, E., Hunt, L. K., Iovino, A., Karachentsev, I. D., Karachentseva, V. E., Koopmann, R. A., Marinoni, C., Minchin, R., Muller, E., Putman, M., Pantoja, C., Salzer, J. J., Scodeggio, M., Skillman, E., Solanes, J. M., Valotto, C., van Driel, W., & van Zee, L. 2005b, Astron. J, 130, 2598

Giovanelli, R., Haynes, M. P., Kent, B. R., Saintonge, A., Stierwalt, S., Altaf, A., Balonek, T., Brosch, N., Brown, S., Catinella, B., Furniss, A., Goldstein, J., Hoffman, G. L., Koopmann, R. A., Kornreich, D. A., Mahmood, B., Martin, A. M., Masters, K. L., Mitschang, A., Momjian, E., Nair, P. H., Rosenberg, J. L., & Walsh, B. 2007, Astron. J, 133, 2569

Giovanelli, R., Williams, J. P., & Haynes, M. P. 1991, Astron. J, 101, 1242

Goldstein, S. J. 1966a, Astron. J, 71, 162

Goldstein, Jr., S. J. 1966b, Science, 151, 71

Guhathakurta, P., van Gorkom, J. H., Kotanyi, C. G., & Balkowski, C. 1988, Astron. J, 96, 851

Gunn, J. E. & Gott, J. R. I. 1972, Astrophys. J., 176, 1

Hanisch, R. J., Farris, A., Greisen, E. W., Pence, W. D., Schlesinger, B. M., Teuben, P. J., Thompson, R. W., & Warnock, III, A. 2001, Astron. Astrophys., 376, 359

Hawkins, M. R. S. 1997, Astron. Astrophys., 328, L25

Haynes, M. P. 1985, in The Virgo Cluster of Galaxies, 45–50

Haynes, M. P. & Giovanelli, R. 1984, Astron. J, 89, 758

—. 1986, Astrophys. J., 306, 466

Haynes, M. P., Giovanelli, R., & Chincarini, G. L. 1984, Ann. Rev. Astron. Astrophys., 22, 445

Haynes, M. P., Giovanelli, R., & Kent, B. R. 2007, Astrophys. J., Lett., 665, L19

Heeschen, D. S. 1957, Astrophys. J., 126, 471

Helou, G., Hoffman, G. L., & Salpeter, E. E. 1984, Astrophys. J., Suppl. Ser., 55, 433

Helou, G., Salpeter, E. E., Giovanardi, C., & Krumm, N. 1981, Astrophys. J., Suppl. Ser., 46, 267

Helou, G., Salpeter, E. E., & Krumm, N. 1979, Astrophys. J., Lett., 228, L1

Henning, P. A., Sancisi, R., & McNamara, B. R. 1993, Astron. Astrophys., 268, 536

Henning, P. A., Staveley-Smith, L., Ekers, R. D., Green, A. J., Haynes, R. F., Juraszek, S., Kesteven, M. J., Koribalski, B., Kraan-Korteweg, R. C., Price, R. M., Sadler, E. M., & Schröder, A. 2000, Astron. J, 119, 2686

Hibbard, J. E., van der Hulst, J. M., Barnes, J. E., & Rich, R. M. 2001, Astron. J, 122, 2969

Hiltner, W. A. 1959, Astrophys. J., 130, 340

Hinks, A. 1911, Mon. Not. R. Astron. Soc., 71, 588

—. 1914, Mon. Not. R. Astron. Soc., 74, 707

Hoffman, G. L., Glosson, J., Helou, G., Salpeter, E. E., & Sandage, A. 1987, Astrophys. J., Suppl. Ser., 63, 247

Hoffman, G. L., Helou, G., Salpeter, E. E., & Lewis, B. M. 1989a, Astrophys. J., 339, 812

Hoffman, G. L., Lu, N. Y., & Salpeter, E. E. 1992, Astron. J, 104, 2086

Hoffman, G. L., Olson, D. W., & Salpeter, E. E. 1980, Astrophys. J., 242, 861

Hoffman, G. L., Williams, B. M., Lewis, B. M., Helou, G., & Salpeter, E. E. 1989b, Astrophys. J., Suppl. Ser., 69, 65

Holmberg, E. 1961, Astron. J, 66, 620

Hubble, E. & Humason, M. L. 1931, Astron. J, 74, 43

Huchra, J. P. 1988, in Astronomical Society of the Pacific Conference Series, Vol. 5, The Minnesota lectures on Clusters of Galaxies and Large-Scale Structure, ed. J. M. Dickey, 41–70

Ibata, R. A., Wyse, R. F. G., Gilmore, G., Irwin, M. J., & Suntzeff, N. B. 1997, Astron. J, 113, 634

Impey, C., Bothun, G., Malin, D., & Staveley-Smith, L. 1990, Astrophys. J., Lett., 351, L33

Jacoby, G. H., Kenney, J. D. P., Tal, T., Crowl, H. H., & Feldmeier, J. J. 2005, in Bulletin of the American Astronomical Society, Vol. 37, Bulletin of the American Astronomical Society, 1392

Jansky, K. G. 1933, Proceedings of the IRE, 21, 1387

Jordán, A., Côté, P., Ferrarese, L., Blakeslee, J. P., Mei, S., Merritt, D., Milosavljević, M., Peng, E. W., Tonry, J. L., & West, M. J. 2004, Astrophys. J., 613, 279

Kellogg, E., Gursky, H., Leong, C., Schreier, E., Tananbaum, H., & Giacconi, R. 1971, Astrophys. J., Lett., 165, L49+

Kenney, J. D. P., Koopmann, R. A., Rubin, V. C., & Young, J. S. 1996, Astron. J, 111, 152

Kent, B. R. 2008, in Astronomical Society of the Pacific Conference Series, Vol. 382, The National Virtual Observatory: Tools and Techniques for Astronomical Research, ed. M. J. Graham, M. J. Fitzpatrick, & T. A. McGlynn, 493–497

Kent, B. R., Giovanelli, R., Haynes, M. P., Martin, A. M., Stierwalt, S., Saintonge, A., Balonek, T. J., Brosch, N., & Koopmann, R. A. 2008, Astron. J., 136, 713

Kent, B. R., Giovanelli, R., Haynes, M. P., Saintonge, A., Stierwalt, S., Balonek, T., Brosch, N., Catinella, B., Koopmann, R. A., Momjian, E., & Spekkens, K. 2007, Astrophys. J., Lett., 665, L15

Kent, B. R. & Greene, G. R. 2008, in Astronomical Society of the Pacific Conference Series, Vol. 382, The National Virtual Observatory: Tools and Techniques for Astronomical Research, ed. M. J. Graham, M. J. Fitzpatrick, & T. A. McGlynn, 555–560

Kent, B. R. & Plante, R. 2008, in Astronomical Society of the Pacific Conference Series, Vol. 382, The National Virtual Observatory: Tools and Techniques for Astronomical Research, ed. M. J. Graham, M. J. Fitzpatrick, & T. A. McGlynn, 489–491

Kilborn, V. A., Staveley-Smith, L., Marquarding, M., Webster, R. L., Malin, D. F., Banks, G. D., Bhathal, R., de Blok, W. J. G., Boyce, P. J., Disney, M. J., Drinkwater, M. J., Ekers, R. D., Freeman, K. C., Gibson, B. K., Henning, P. A., Jerjen, H., Knezek, P. M., Koribalski, B., Minchin, R. F., Mould, J. R., Oosterloo, T., Price, R. M., Putman, M. E., Ryder, S. D., Sadler, E. M., Stewart, I., Stootman, F., & Wright, A. E. 2000, Astron. J, 120, 1342

Kildal, P.-S., Johansson, M., Hagfors, T., & Giovanelli, R. 1993, IEEE Trans. Antennas Propag., 41, 1019

Klypin, A., Kravtsov, A. V., Valenzuela, O., & Prada, F. 1999, Astrophys. J., 522, 82

Knobloch, E. 2007, Centaurus, 49, 3

Koehler, J. A. & Robinson, B. J. 1966, Astrophys. J., 146, 488

Kraan-Korteweg, R. C. 1982, Astron. Astrophys. Suppl. Ser., 47, 505

Kraan-Korteweg, R. C., van Driel, W., Briggs, F., Binggeli, B., & Mostefaoui, T. I. 1999, Astron. Astrophys. Suppl. Ser., 135, 255

Kraus, J. D. 1966, Radio astronomy (New York: McGraw-Hill, 1966)

Krumm, N. & Salpeter, E. E. 1976, Astrophys. J., Lett., 208, L7

—. 1979, Astrophys. J., 227, 776

Kwok, S. H. 2008, in Astronomical Society of the Pacific Conference Series, Vol. 382, The National Virtual Observatory: Tools and Techniques for Astronomical Research, ed. M. J. Graham, M. J. Fitzpatrick, & T. A. McGlynn, 221–240

Kwok, S. H. & Tody, D. 2008a, in Astronomical Society of the Pacific Conference Series, Vol. 382, The National Virtual Observatory: Tools and Techniques for Astronomical Research, ed. M. J. Graham, M. J. Fitzpatrick, & T. A. McGlynn, 511–524

Kwok, S. H. & Tody, D. 2008b, in Astronomical Society of the Pacific Conference Series, Vol. 382, The National Virtual Observatory: Tools and Techniques for Astronomical Research, ed. M. J. Graham, M. J. Fitzpatrick, & T. A. McGlynn, 499–510

Laity, A. C., Anagnostou, N., Berriman, G. B., Good, J. C., Jacob, J. C., Katz, D. S., & Prince, T. 2005, in Astronomical Society of the Pacific Conference Series, Vol. 347, Astronomical Data Analysis Software and Systems XIV, ed. P. Shopbell, M. Britton, & R. Ebert, 34

Lalonde, L. M. 1974, Science, 186, 213

Lang, R. H., Boyce, P. J., Kilborn, V. A., Minchin, R. F., Disney, M. J., Jordan, C. A., Grossi, M., Garcia, D. A., Freeman, K. C., Phillipps, S., & Wright, A. E. 2003, Mon. Not. R. Astron. Soc., 342, 738

Lasker, B. M., Sturch, C. R., McLean, B. J., Russell, J. L., Jenkner, H., & Shara, M. M. 1990, Astron. J, 99, 2019

Lewis, B. M. & Davies, R. D. 1973, Mon. Not. R. Astron. Soc., 165, 213

Lu, L., Sargent, W. L. W., Savage, B. D., Wakker, B. P., Sembach, K. R., & Oosterloo, T. A. 1998, Astron. J, 115, 162

Majewski, S. R., Skrutskie, M. F., Weinberg, M. D., & Ostheimer, J. C. 2003, Astrophys. J., 599, 1082

Markarian, B. E. 1961, Astron. J, 66, 555

Masters, K. L., Haynes, M. P., & Giovanelli, R. 2004, Astrophys. J., Lett., 607, L115

McClintock, J. E., Lewin, W. H. G., Sullivan, R. J., & Clark, G. W. 1969, Nature, 223, 162

McGlynn, T. A. & Nieto-Santisteban, M. 2008, in Astronomical Society of the Pacific Conference Series, Vol. 382, The National Virtual Observatory: Tools and Techniques for Astronomical Research, ed. M. J. Graham, M. J. Fitzpatrick, & T. A. McGlynn, 643–653

McGlynn, T. A., White, N. E., & Scollick, K. 1994, in Bulletin of the American Astronomical Society, Vol. 26, Bulletin of the American Astronomical Society, 898

McLaughlin, D. E. 1999, Astrophys. J., Lett., 512, L9

McNamara, B. R., Sancisi, R., Henning, P. A., & Junor, W. 1994, Astron. J, 108, 844

Mei, S., Blakeslee, J. P., Côté, P., Tonry, J. L., West, M. J., Ferrarese, L., Jordán, A., Peng, E. W., Anthony, A., & Merritt, D. 2007, Astrophys. J., 655, 144

Mei, S., Blakeslee, J. P., Tonry, J. L., Jordán, A., Peng, E. W., Côté, P., Ferrarese, L., Merritt, D., Milosavljević, M., & West, M. J. 2005, Astrophys. J., Suppl. Ser., 156, 113

Messier, C. 1781, Connoissance des Temps

Meyer, M. J., Zwaan, M. A., Webster, R. L., Staveley-Smith, L., Ryan-Weber, E., Drinkwater, M. J., Barnes, D. G., Howlett, M., Kilborn, V. A., Stevens, J., Waugh,

M., Pierce, M. J., Bhathal, R., de Blok, W. J. G., Disney, M. J., Ekers, R. D., Freeman, K. C., Garcia, D. A., Gibson, B. K., Harnett, J., Henning, P. A., Jerjen, H., Kesteven, M. J., Knezek, P. M., Koribalski, B. S., Mader, S., Marquarding, M., Minchin, R. F., O'Brien, J., Oosterloo, T., Price, R. M., Putman, M. E., Ryder, S. D., Sadler, E. M., Stewart, I. M., Stootman, F., & Wright, A. E. 2004, Mon. Not. R. Astron. Soc., 350, 1195

Mihos, J. C., Harding, P., Feldmeier, J., & Morrison, H. 2005, Astrophys. J., Lett., 631, L41

Minchin, R., Davies, J., Disney, M., Boyce, P., Garcia, D., Jordan, C., Kilborn, V., Lang, R., Roberts, S., Sabatini, S., & van Driel, W. 2005, Astrophys. J., Lett., 622, L21

Minchin, R., Davies, J., Disney, M., Grossi, M., Sabatini, S., Boyce, P., Garcia, D., Impey, C., Jordan, C., Lang, R., Marble, A., Roberts, S., & van Driel, W. 2007, Astrophys. J., 670, 1056

Minchin, R. F., Disney, M. J., Boyce, P. J., de Blok, W. J. G., Parker, Q. A., Banks, G. D., Freeman, K. C., Garcia, D. A., Gibson, B. K., Grossi, M., Haynes, R. F., Knezek, P. M., Lang, R. H., Malin, D. F., Price, R. M., Stewart, I. M., & Wright, A. E. 2003, Mon. Not. R. Astron. Soc., 346, 787

Moore, B., Ghigna, S., Governato, F., Lake, G., Quinn, T., Stadel, J., & Tozzi, P. 1999, Astrophys. J., Lett., 524, L19

Moore, B., Katz, N., Lake, G., Dressler, A., & Oemler, A. 1996, Nature, 379, 613

Moore, B., Lake, G., & Katz, N. 1998, Astrophys. J., 495, 139

Muller, C. A. & Oort, J. H. 1951, Nature, 168, 357

Napier, P. J., Thompson, R. T., & Ekers, R. D. 1993, Proc. IEEE, 71, 1295

Oort, J. H. 1958, Ricerche Astronomiche, 5, 25

Oosterloo, T. & van Gorkom, J. 2005, Astron. Astrophys., 437, L19

Osterbrock, D. E. 1960, Astrophys. J., 132, 325

Peng, E. W., Côté, P., Jordán, A., Blakeslee, J. P., Ferrarese, L., Mei, S., West, M. J., Merritt, D., Milosavljević, M., & Tonry, J. L. 2006a, Astrophys. J., 639, 838

Peng, E. W., Jordán, A., Côté, P., Blakeslee, J. P., Ferrarese, L., Mei, S., West, M. J., Merritt, D., Milosavljević, M., & Tonry, J. L. 2006b, Astrophys. J., 639, 95

Plummer, H. C. 1915, Mon. Not. R. Astron. Soc., 76, 107

Putman, M. E., Gibson, B. K., Staveley-Smith, L., Banks, G., Barnes, D. G., Bhatal, R., Disney, M. J., Ekers, R. D., Freeman, K. C., Haynes, R. F., Henning, P., Jerjen, H., Kilborn, V., Koribalski, B., Knezek, P., Malin, D. F., Mould, J. R., Oosterloo, T., Price, R. M., Ryder, S. D., Sadler, E. M., Stewart, I., Stootman, F., Vaile, R. A., Webster, R. L., & Wright, A. E. 1998, Nature, 394, 752

Reaves, G. 1956, Astron. J, 61, 69

—. 1983, Astrophys. J., Suppl. Ser., 53, 375

Reber, G. 1944, Astrophys. J., 100, 279

Roberts, M. S. 1962a, Astron. J, 67, 431

—. 1962b, Astron. J, 67, 437

Roberts, M. S. 1972, in IAU Symposium, Vol. 44, External Galaxies and Quasi-Stellar Objects, ed. D. S. Evans, D. Wills, & B. J. Wills, 12

—. 1975, Radio Observations of Neutral Hydrogen in Galaxies (Galaxies and the Universe), 309

Robinson, B. J. 1965, Nature, 208, 993

Robinson, B. J., van Damme, K. J., & Koehler, J. A. 1963, Nature, 199, 1176

Rosenberg, J. L. & Schneider, S. E. 2002, Astrophys. J., 567, 247

Rownd, B. K., Dickey, J. M., & Helou, G. 1994, Astron. J, 108, 1638

Ryder, S. D., Koribalski, B., Staveley-Smith, L., Kilborn, V. A., Malin, D. F., Banks, G. D., Barnes, D. G., Bhatal, R., de Blok, W. J. G., Boyce, P. J., Disney, M. J., Drinkwater, M. J., Ekers, R. D., Freeman, K. C., Gibson, B. K., Henning, P. A., Jerjen, H., Knezek, P. M., Marquarding, M., Minchin, R. F., Mould, J. R., Oosterloo, T., Price, R. M., Putman, M. E., Sadler, E. M., Stewart, I., Stootman, F., Webster, R. L., & Wright, A. E. 2001, Astrophys. J., 555, 232

Saintonge, A. 2007a, PhD thesis, Cornell University

—. 2007b, Astron. J, 133, 2087

Saintonge, A., Giovanelli, R., Haynes, M. P., Hoffman, G. L., Kent, B. R., Martin, A. M., Stierwalt, S., & Brosch, N. 2008, Astron. J, 135, 588

Salzer, J. J., di Serego Alighieri, S., Matteucci, F., Giovanelli, R., & Haynes, M. P. 1991, Astron. J, 101, 1258

Sancisi, R., Thonnard, N., & Ekers, R. D. 1987, Astrophys. J., Lett., 315, L39

Sandage, A. & Binggeli, B. 1984, Astron. J, 89, 919

Sandage, A., Binggeli, B., & Tammann, G. A. 1985a, Astron. J, 90, 1759

—. 1985b, Astron. J, 90, 395

Sarazin, C. L. 1986, Reviews of Modern Physics, 58, 1

Saunders, W., Sutherland, W., Efstathiou, G., Tadros, H., Maddox, S., White, S., Oliver, S., Keeble, O., Rowan-Robinson, M., & Frenk, C. 1995, in Wide Field Spectroscopy and the Distant Universe, ed. S. J. Maddox & A. Aragon-Salamanca, 88

Schechter, P. 1976, Astrophys. J., 203, 297

Schindler, S., Binggeli, B., & Böhringer, H. 1999, Astron. Astrophys., 343, 420

Schmidt, M. 1968, Astrophys. J., 151, 393

Schmoldt, I. M., Saar, V., Saha, P., Branchini, E., Efstathiou, G. P., Frenk, C. S., Keeble, O., Maddox, S., McMahon, R., Oliver, S., Rowan-Robinson, M., Saunders, W., Sutherland, W. J., Tadros, H., & White, S. D. M. 1999, Astron. J, 118, 1146

Schneider, S. E., Helou, G., Salpeter, E. E., & Terzian, Y. 1983, Astrophys. J., Lett., 273, L1

Schwarz, U. J. 1978, Astron. Astrophys., 65, 345

Schwassmann, A. 1902, Publ. Astrophys. Obs. Königstuhl-Heidelberg, 1, 17

Shapley, H. & Ames, A. 1926, Harvard Circ., 294

—. 1929, Harvard Bulletin, 865

—. 1930a, Harvard Bulletin, 873

—. 1930b, Harvard Bulletin, 880

—. 1932, Harvard Bulletin, 80, 41

Shibata, R., Matsushita, K., Yamasaki, N. Y., Ohashi, T., Ishida, M., Kikuchi, K., Böhringer, H., & Matsumoto, H. 2001, Astrophys. J., 549, 228

Shostak, G. S. & Allen, R. J. 1980, Astron. Astrophys., 81, 167

Skrutskie, M. F., Cutri, R. M., Stiening, R., Weinberg, M. D., Schneider, S., Carpenter, J. M., Beichman, C., Capps, R., Chester, T., Elias, J., Huchra, J., Liebert, J., Lonsdale, C., Monet, D. G., Price, S., Seitzer, P., Jarrett, T., Kirkpatrick, J. D., Gizis, J. E., Howard, E., Evans, T., Fowler, J., Fullmer, L., Hurt, R., Light, R., Kopan, E. L., Marsh, K. A., McCallon, H. L., Tam, R., Van Dyk, S., & Wheelock, S. 2006, Astron. J, 131, 1163

Smith, S. 1936, Astrophys. J., 83, 23

Snowden, S. L., Freyberg, M. J., Plucinsky, P. P., Schmitt, J. H. M. M., Truemper, J., Voges, W., Edgar, R. J., McCammon, D., & Sanders, W. T. 1995, Astrophys. J., 454, 643

Solanes, J. M., Manrique, A., García-Gómez, C., González-Casado, G., Giovanelli, R., & Haynes, M. P. 2001, Astrophys. J., 548, 97

Solanes, J. M., Sanchis, T., Salvador-Solé, E., Giovanelli, R., & Haynes, M. P. 2002, Astron. J, 124, 2440

Somerville, R. S. 2002, Astrophys. J., Lett., 572, L23

Spekkens, K. 2008, Private communication

Spergel, D. N., Bean, R., Doré, O., Nolta, M. R., Bennett, C. L., Dunkley, J., Hinshaw, G., Jarosik, N., Komatsu, E., Page, L., Peiris, H. V., Verde, L., Halpern, M., Hill, R. S., Kogut, A., Limon, M., Meyer, S. S., Odegard, N., Tucker, G. S., Weiland, J. L., Wollack, E., & Wright, E. L. 2007, Astrophys. J., Suppl. Ser., 170, 377

Springel, V. 2005, Mon. Not. R. Astron. Soc., 364, 1105

Springob, C. M., Haynes, M. P., & Giovanelli, R. 2005a, Astrophys. J., 621, 215

Springob, C. M., Haynes, M. P., Giovanelli, R., & Kent, B. R. 2005b, Astrophys. J., Suppl. Ser., 160, 149

Springob, C. M., Masters, K. L., Haynes, M. P., Giovanelli, R., & Marinoni, C. 2007, Astrophys. J., Suppl. Ser., 172, 599

Szalay, A. S., Gray, J., Kunszt, P., Thakar, A., & Slutz, D. 2001, in Mining the Sky, ed. A. J. Banday, S. Zaroubi, & M. Bartelmann, 99

Tammann, G. 1985, in ESO Conference and Workshop Proceedings, Vol. 20, ESO Workshop on the Virgo Cluster, ed. O.-G. Richter & B. Binggeli, 3–10

Taylor, E. N. & Webster, R. L. 2005, Astrophys. J., 634, 1067

Tody, D. & Fitzpatrick, M. J. 2008, in Astronomical Society of the Pacific Conference Series, Vol. 382, The National Virtual Observatory: Tools and Techniques for Astronomical Research, ed. M. J. Graham, M. J. Fitzpatrick, & T. A. McGlynn, 207–219

Tonry, J. L., Blakeslee, J. P., Ajhar, E. A., & Dressler, A. 2000, Astrophys. J., 530, 625

Toomre, A. & Toomre, J. 1972, Astrophys. J., 178, 623

Tully, R. B. & Fisher, J. R. 1977, Astron. Astrophys., 54, 661

van de Hulst, H. C. 1945, Ned. Tijdschr. Natuurk., 11, 201

van den Bergh, S. 1960a, Mon. Not. R. Astron. Soc., 121, 387

—. 1960b, Astron. J, 65, 502

van Gorkom, J. H., Balkowski, C., & Kotanyi, C. 1984a, in Clusters and Groups of Galaxies. International Meeting held in Trieste, Italy, September 13-16, 1983, ed. F. Mardirossian, G. Giuricin, & M. Mezzetti, 261

van Gorkom, J. H., Kotanyi, C. G., & Balkowski, C. 1984b, in Bulletin of the American Astronomical Society, Vol. 16, Bulletin of the American Astronomical Society, 720

Verschuur, G. L. 1969, Astrophys. J., 156, 771

Vollmer, B., Cayatte, V., Balkowski, C., & Duschl, W. J. 2001, Astrophys. J., 561, 708

Vollmer, B. & Huchtmeier, W. 2003, Astron. Astrophys., 406, 427

Vollmer, B., Soida, M., Chung, A., van Gorkom, J. H., Otmianowska-Mazur, K., Beck, R., Urbanik, M., & Kenney, J. D. P. 2008, Astron. Astrophys., 483, 89

Wade, C. M. 1961, The Observatory, 81, 202

Warmels, R. H. & van Woerden, H. 1983, in IAU Symposium, Vol. 104, Early Evolution of the Universe and its Present Structure, ed. G. O. Abell & G. Chincarini, 261

Westerhout, G. 1962, in IAU Symposium, Vol. 15, Problems of Extra-Galactic Research, ed. G. C. McVittie, 70

White, M., Krauss, L. M., & Silk, J. 1993, Astrophys. J., 418, 535

Wong, O. I., Ryan-Weber, E. V., Garcia-Appadoo, D. A., Webster, R. L., Staveley-Smith, L., Zwaan, M. A., Meyer, M. J., Barnes, D. G., Kilborn, V. A., Bhathal, R., de Blok, W. J. G., Disney, M. J., Doyle, M. T., Drinkwater, M. J., Ekers, R. D., Freeman, K. C., Gibson, B. K., Gurovich, S., Harnett, J., Henning, P. A., Jerjen, H., Kesteven, M. J., Knezek, P. M., Koribalski, B. S., Mader, S., Marquarding, M., Minchin, R. F., O'Brien, J., Putman, M. E., Ryder, S. D., Sadler, E. M., Stevens, J., Stewart, I. M., Stootman, F., & Waugh, M. 2006, Mon. Not. R. Astron. Soc., 371, 1855

York, D. G., Adelman, J., Anderson, Jr., J. E., Anderson, S. F., Annis, J., Bahcall, N. A., Bakken, J. A., Barkhouser, R., Bastian, S., Berman, E., Boroski, W. N., Bracker, S., Briegel, C., Briggs, J. W., Brinkmann, J., Brunner, R., Burles, S., Carey, L.,

Carr, M. A., Castander, F. J., Chen, B., Colestock, P. L., Connolly, A. J., Crocker, J. H., Csabai, I., Czarapata, P. C., Davis, J. E., Doi, M., Dombeck, T., Eisenstein, D., Ellman, N., Elms, B. R., Evans, M. L., Fan, X., Federwitz, G. R., Fiscelli, L., Friedman, S., Frieman, J. A., Fukugita, M., Gillespie, B., Gunn, J. E., Gurbani, V. K., de Haas, E., Haldeman, M., Harris, F. H., Hayes, J., Heckman, T. M., Hennessy, G. S., Hindsley, R. B., Holm, S., Holmgren, D. J., Huang, C.-h., Hull, C., Husby, D., Ichikawa, S.-I., Ichikawa, T., Ivezić, Ž., Kent, S., Kim, R. S. J., Kinney, E., Klaene, M., Kleinman, A. N., Kleinman, S., Knapp, G. R., Korienek, J., Kron, R. G., Kunszt, P. Z., Lamb, D. Q., Lee, B., Leger, R. F., Limmongkol, S., Lindenmeyer, C., Long, D. C., Loomis, C., Loveday, J., Lucinio, R., Lupton, R. H., MacKinnon, B., Mannery, E. J., Mantsch, P. M., Margon, B., McGehee, P., McKay, T. A., Meiksin, A., Merelli, A., Monet, D. G., Munn, J. A., Narayanan, V. K., Nash, T., Neilsen, E., Neswold, R., Newberg, H. J., Nichol, R. C., Nicinski, T., Nonino, M., Okada, N., Okamura, S., Ostriker, J. P., Owen, R., Pauls, A. G., Peoples, J., Peterson, R. L., Petravick, D., Pier, J. R., Pope, A., Pordes, R., Prosapio, A., Rechenmacher, R., Quinn, T. R., Richards, G. T., Richmond, M. W., Rivetta, C. H., Rockosi, C. M., Ruthmansdorfer, K., Sandford, D., Schlegel, D. J., Schneider, D. P., Sekiguchi, M., Sergey, G., Shimasaku, K., Siegmund, W. A., Smee, S., Smith, J. A., Snedden, S., Stone, R., Stoughton, C., Strauss, M. A., Stubbs, C., SubbaRao, M., Szalay, A. S., Szapudi, I., Szokoly, G. P., Thakar, A. R., Tremonti, C., Tucker, D. L., Uomoto, A., Vanden Berk, D., Vogeley, M. S., Waddell, P., Wang, S.-i., Watanabe, M., Weinberg, D. H., Yanny, B., & Yasuda, N. 2000, Astron. J, 120, 1579

Yun, M. S., Ho, P. T. P., & Lo, K. Y. 1994, Nature, 372, 530

Zwaan, M. A., Briggs, F. H., Sprayberry, D., & Sorar, E. 1997, Astrophys. J., 490, 173

Zwaan, M. A., Meyer, M. J., Staveley-Smith, L., & Webster, R. L. 2005, Mon. Not. R.

Astron. Soc., 359, L30

Zwaan, M. A., Meyer, M. J., Webster, R. L., Staveley-Smith, L., Drinkwater, M. J., Barnes, D. G., Bhathal, R., de Blok, W. J. G., Disney, M. J., Ekers, R. D., Freeman, K. C., Garcia, D. A., Gibson, B. K., Harnett, J., Henning, P. A., Howlett, M., Jerjen, H., Kesteven, M. J., Kilborn, V. A., Knezek, P. M., Koribalski, B. S., Mader, S., Marquarding, M., Minchin, R. F., O'Brien, J., Oosterloo, T., Pierce, M. J., Price, R. M., Putman, M. E., Ryan-Weber, E., Ryder, S. D., Sadler, E. M., Stevens, J., Stewart, I. M., Stootman, F., Waugh, M., & Wright, A. E. 2004, Mon. Not. R. Astron. Soc., 350, 1210

Zwaan, M. A., Staveley-Smith, L., Koribalski, B. S., Henning, P. A., Kilborn, V. A., Ryder, S. D., Barnes, D. G., Bhathal, R., Boyce, P. J., de Blok, W. J. G., Disney, M. J., Drinkwater, M. J., Ekers, R. D., Freeman, K. C., Gibson, B. K., Green, A. J., Haynes, R. F., Jerjen, H., Juraszek, S., Kesteven, M. J., Knezek, P. M., Kraan-Korteweg, R. C., Mader, S., Marquarding, M., Meyer, M., Minchin, R. F., Mould, J. R., O'Brien, J., Oosterloo, T., Price, R. M., Putman, M. E., Ryan-Weber, E., Sadler, E. M., Schröder, A., Stewart, I. M., Stootman, F., Warren, B., Waugh, M., Webster, R. L., & Wright, A. E. 2003, Astron. J, 125, 2842

Zwicky, F. 1957, Morphological astronomy (Berlin: Springer, 1957)

—. 1959, Handbuch der Physik, 53, 390

INDEX

L-band, 17
2MASS, 4
3C 138, 20

A1367-Coma, 45
aitoff projection, 120
ALFA beam pattern, 18
ALFALFA, 14, 16, 36
Arecibo, 9
Arecibo *L*-band Feed Array, 17
Arecibo Dual Beam Survey, 16

bandpass subtraction, 30

calibration, 27
cone search, 127
continuum pointing correction, 55
Cosmic Microwave Background, 3

dark matter halos, 77
data cube, 33
Digital Sky Survey, 39
drift scan, 25

flagging rfi, 31
Flexible Image Transport System, 25

GADGET-2, 112
galactic neutral hydrogen, 120
gas evaporation, 103
GRIDView, 34, 161

HI line frequency, 5
HI mass, 21
HI mass function, 108, 109
HI Parkes All Sky Survey, 16
HI1225+01, 58, 77
high-velocity cloud, 45

Interactive Data Language, 26

Jansky, Karl, 5

Lambda-Cold Dark Matter, 3
Level I, 26

M87, 7, 45
mass–to–light ratio, 89
missing satellite problem, 58
Montage, 120
mosaic, 121

N-body, 106
NAIC, 16
Neutral Hydrogen, 5
NGC 4388, 59
NGC 4424, 67
NRAO VLA Sky Survey, 47

Palomar 5-m Hale Telescope, 89
peculiar velocities, 42
positional accuracy, 51
PSC*z*, 1

radio frequency interference, 46
ram pressure stripping, 96
Reber, Grote, 5

Schechter fit, 110
SDSS, 4
Simple Image Access Protocol, 145
SKA, 16
smoothed particle hydrodynamics, 106
spectra, 39
Structured Query Language, 138

Unified Content Descriptor, 128

Virgo cluster, 6, 58
Virtual Observatory, 34, 36, 118
VLA, 10, 74

Wideband Arecibo Pulsar Processor, 24
width dependence, 40

X-rays, 89